UNIVERSITY OF SOUTHAMPTON

**OSCILLATORY WAVE-INDUCED BOUNDARY LAYER FLOW
OVER A RIPPLED BED**

By

Yann Ourmières

A thesis submitted for the degree of Doctor of Philosophy.

Faculty of Engineering and Applied Science
Department of Civil and Environmental Engineering

October 2003

UNIVERSITY OF SOUTHAMPTON

ABSTRACT

FACULTY OF ENGINEERING AND APPLIED SCIENCE

DEPARTMENT OF CIVIL AND ENVIRONMENTAL ENGINEERING

Doctor of Philosophy

OSCILLATORY WAVE-INDUCED BOUNDARY LAYER FLOW OVER A

RIPPLED BED

by Yann Ourmières

The aim of this project is to study the wave-induced flow above a rippled bed. Sea bed ripples do not have a major impact on the main flow pattern, but they strongly influence the structure of the boundary layer. Therefore they are of interest in coastal engineering as they are part of the sediment transport process and have influence on surface wave dissipation and flow friction in coastal areas.

By both numerical and experimental means, the flow characteristics were studied. A two-dimensional computer model solving this particular flow was developed and compared to other numerical and experimental data and the available theory. Experiments were conducted in a wave tank fitted with a rigid rippled bed, and flow visualizations were done using fluorescent dye filmed by a digital video camera. Different flow regimes were identified and were classified in terms of relevant parameters such as the ripple slope, the wave orbital amplitude to ripple wavelength ratio and the Taylor number. For a weak flow oscillation to ripple wavelength ratio, two-dimensional structures tend to develop in the form of recirculation cells. For a stronger flow oscillation and a medium to steep ripple slope, the flow separates giving rise to vortices ejected from the ripple crests every half-wave period. Three-dimensional instabilities also appear in two different forms. The most common form observed is a structure of "rings". The other form called brick-pattern is suspected to involve centrifugal instabilities and play a major role in the building of three-dimensional ripple shapes. A final summary of the flow characteristics was done, using the numerical and experimental results.

Contents

List of Figures

List of Tables

Acknowledgements

I wish to express my gratitude to my supervisor Mr John Chaplin who helped me all the way through this three years project, providing me with valuable advice and ideas and always making sure that I was staying in the right tracks. I also wish to thank John and his wife for making me feel more than welcome in England. I wish to thank the Department of Civil and Environmental Engineering for giving me the opportunity to work as a PhD student in the University of Southampton. I wish to thank the people I met during this period and became helpful friends at work and outside work: Fabien, Dominique, Jo, Reuben, Heidi, Anne, Anthony, Martin, Michelle and Chris. I also want to thank the English weather for being so often wet and windy.

Je tiens à remercier ma famille, et tout particulièrement mes parents pour leur soutien exceptionnel et leur patience, car ils ont fait de moi ce que je suis. Un gros merci à Joe, Ketty, Franck, Indra, Steph, Jules, Rodolphe, Nico et toute la compagnie 2002 pour m'avoir apporté réconfort et distraction française aux moments cruciaux où la folie me guettait.

List of Notations

Chapter 1

Introduction

The main subject of this thesis is a study of the flow induced by waves propagating over a rippled bed. Sea bed ripples are mainly present on sand beds in shallow coastal waters, and it is well known that their formation is due to the back and forth motion induced just above the bed by waves. Their evolution is influenced by the wave characteristics and those of the sediment, such as the size and density of the particles. Sea bed ripples do not have a major impact on the main flow pattern, but they strongly influence the structure of the benthic boundary layer. Therefore they are part of the sediment transport process, and have influence on flow friction, and surface wave dissipation.

The wave-induced flow is an oscillatory flow whose amplitude at a certain depth will be determined by the wave height and wave period. One particular feature of this flow is that each particle follows an unclosed path, resulting in a drift of the particles in the same direction as the wave propagation. For a water depth much larger than the wave wavelength, the particle path will be almost circular. For a shallow water case, where the wave wavelength is very long compared with the water depth, the particle path will be more elliptic. If the flow near the bottom boundary is considered, it is characterized by the generation of a steady current close to the bed in the direction of the wave propagation due to the oscillating and progressive nature of the flow. This

1

steady second order drift velocity is usually referred to as the Stokes drift or the mass transport velocity.

Wave-induced flow has been widely studied, from the free surface to the sea bed. It has been intensively studied in the boundary layer over a flat bed, where Longuet-Higgins's theory (1953) describes the flow behaviour in laminar cases. This theory is still widely cited. Oscillatory flow above a rippled bed has also been studied for many years, but there is no established theory for this case. Experiments have been conducted in wave flumes with sand beds or even rigid wavy beds, to provide measurements of some relevant features of the flow: the mean flow, the mass transport velocity, the vorticity and the sediment transport. A few two-dimensional computer models have been developed, solving the vorticity and velocity fields over a rippled domain. The complexity of such a flow makes its study still topical and worthwhile since agreement between models and experiments has not been systematically reached. Moreover, this flow is potentially three-dimensional, and this feature is often neglected in numerical modelling even now. Three-dimensional instabilities as well as two-dimensional instabilities are believed to play an important role in the ripple dynamics. Due to numerical and experimental difficulties, the study of such a complex three-dimensional flow is far from complete.

Considering these facts, the main purposes of this thesis can be presented as follows:

- To provide a review of the present knowledge on the wave-induced flow over a rippled bed, mainly from a fluid mechanics approach with some sediment transport approach inputs.

- To compute and use a two-dimensional model solving the flow characteristics in the vicinity of a rippled boundary. This model will first be tested for flat bed cases. Particular attention will be given to the study of the mass transport velocity, flow separation and vortex formation.

- To categorize different flow regimes by means of experimental visualizations of

the flow in a wave flume fitted with a rigid rippled boundary at its bottom. The experiments will be conducted for various ripple slopes and wave conditions.

- To study the threshold for which the two-dimensional flow will first become three-dimensional, and to study three-dimensional instabilities occurring in this flow possibly leading to particular three-dimensional ripple structures.

- To draw possible conclusions on the wave-induced flow features over sea bed ripples.

This thesis is structured in seven chapters. After this brief introduction of the subject, chapter 2 provides a review of the present knowledge on wave-induced flows over flat and rippled beds, on oscillatory flow instabilities over curved boundaries and on ripple characteristics. Chapter 3 details the computed two-dimensional model solving the flow in this particular area, while chapter 4 provides varied results from the model, comparisons with several sources, and discussions. Chapter 5 presents the chosen set-up for the conducted experiments, while chapter 6 provides the experimental results. Chapter 7 draws conclusions on the work done.

Chapter 2

Literature review

2.1 Introduction

In this chapter, different features of the wave-induced flow will be reviewed. A brief definition of the boundary layer, the area where this study takes place, will be given. Then the characteristics of the oscillatory boundary layer flow are reviewed for the case of a flat bed, and a rippled bed. As the study focuses on laminar conditions, little is developed on the oscillatory boundary layer in turbulent flow, and will be mainly used for a general understanding of the studied phenomenon. Present knowledge on three-dimensional instabilities occurring over curved boundaries is reviewed, leading to a review on centrifugal instabilities over rippled beds, using articles on centrifugal instabilities over cylinders as a starting point. Finally, seabed ripples characteristics such as their size and shape are reviewed.

2.2 Oscillatory wave-induced flow

A cartesian system is defined where x is the horizontal axis, positive in the wave propagation direction, y is the vertical axis, and the origin is at still water level, as shown in figure 2.1. The velocity vector $\vec{u}$ has the components (u,v,w). The fluid
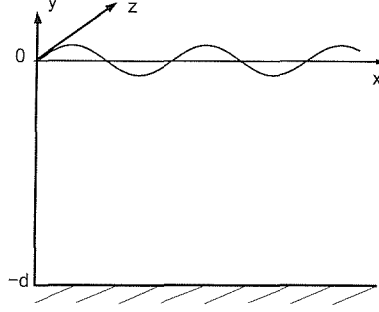
Figure 2.1: Cartesian system of reference.

motion is governed by the conservation law of mass and the Bernoulli equation. The conservation mass equation can be expressed as

$$\vec{\nabla} \cdot \vec{u} = 0, \tag{2.1}$$

and the Bernoulli equation is

$$\frac{\partial \Phi}{\partial t} + \frac{1}{2}u^2 + \frac{p}{\rho} + gy = f(t) \tag{2.2}$$

where p is the pressure, g the gravitational acceleration, ρ the water density, $f(t)$ a function of time and Φ the velocity potential so that

$$\vec{u} = \vec{\nabla}\Phi. \tag{2.3}$$

The arbitrary function of time $f(t)$ can be incorporated into the velocity potential Φ without loss of generality, giving

$$\frac{\partial \Phi}{\partial t} + \frac{1}{2}u^2 + \frac{p}{\rho} + gy = 0. \tag{2.4}$$

The pressure p at the free surface $y = \eta$ is equal to the atmospheric pressure p_a

$$p\big|_{y=\eta} = p_a, \tag{2.5}$$

and chosen to be zero. For $y = \eta$, equation (2.4) can then be changed to

$$\frac{\partial \Phi}{\partial t} + \frac{1}{2}u^2 + g\eta = 0. \tag{2.6}$$

5

The vertical velocity at the free surface is given by

$$v\big|_{y=\eta} = \frac{d\eta}{dt} \tag{2.7}$$

where the differentiation follows a particle at the free surface. As the bed is considered impermeable, the vertical velocity at the bottom is

$$v\big|_{y=-d} = 0. \tag{2.8}$$

Then from equations (2.1), (2.6), (2.7) and (2.8) we have the system of equations:

$$\nabla^2 \Phi = 0, \tag{2.9}$$

$$\frac{\partial \Phi}{\partial y}\big|_{y=-d} = 0, \tag{2.10}$$

$$\frac{d\Phi}{dy}\big|_{y=\eta} = \frac{d\eta}{dt}, \tag{2.11}$$

$$\frac{\partial \Phi}{\partial t} + \frac{1}{2}u^2 + g\eta = 0. \tag{2.12}$$

Equation (2.9) is the Laplace equation. If the assumption is made that waves propagate in the positive x direction, and that the free surface η can be described by $\eta = a\cos(kx - \sigma t)$, then by solving equations (2.9) to (2.12), the horizontal velocity u in the fluid is

$$u = \frac{a\sigma \cosh(k(y+d))}{\sinh(kd)} \cos(kx - \sigma t) \tag{2.13}$$

where a is the wave amplitude, σ the wave angular frequency, d the water depth and k the wavenumber. A sketch of the horizontal wave-induced velocity from the free surface, in the case of infinite water depth is shown in figure 2.2. This flow will change in strength and direction, influenced periodically either by a crest or a trough. In shallow water areas, the wavelength of the wave becomes larger than the water depth so that $kd < 1$. As $k(y+d)$ becomes very small, $\cosh(k(y+d))$ can be approximated by 1 and $\sinh(kd)$ can be approximated by kd. From formula (2.13), the shallow water approximation for the horizontal wave-induced velocity is

$$u = \frac{a\sigma}{kd} \cos(kx - \sigma t). \tag{2.14}$$

6

With such an approximation, the velocity is considered constant in strength from sea surface to bottom[1], as shown in figure 2.3.

wave propagation
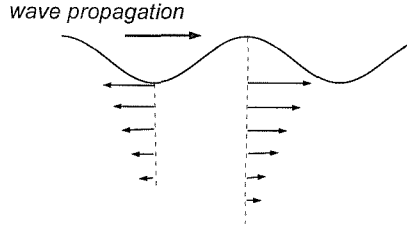
Figure 2.2: Horizontal wave-induced flow for infinite water depth.

wave propagation
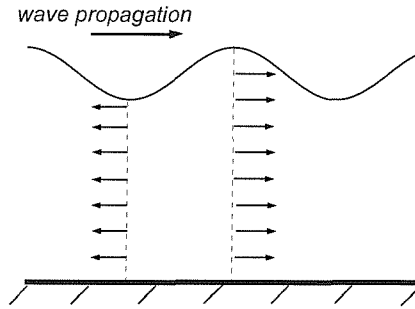
Figure 2.3: Horizontal wave-induced flow in shallow water depth over a flat bed. The characteristics of the flow in the free surface and bottom boundary layers are not represented.

2.3 Brief definition of the bottom boundary layer

In the present study, the bottom boundary layer can be simply defined as the layer inside which the flow is significantly influenced by the sea bed characteristics. In laminar flows, this layer is usually very thin over a smooth solid bed (a few millimeters), and a little larger over a flat sand bed. For the case of a rippled bed, the boundary layer may extend to several times the ripple height (Nielsen, 1992). The wave-induced

---

[1]If the bottom and the free surface boundary layers are neglected (see section 2.3).

boundary layer thickness δ_t is usually defined in terms of

$$\delta_t \sim \sqrt{\nu T}$$

where ν is the water viscosity and T the oscillatory flow period. Even if the qualitative meaning of the bottom boundary layer is clear, opinions about the most appropriate quantitative definition for its thickness are varied. However, the most common definitions use the Stokes length:

$$\delta = \sqrt{\frac{2\nu}{\sigma}}. \tag{2.15}$$

Different definitions for the boundary layer thickness can be found in Jonsson (1966), Kajiura (1968) or Sleath (1987). Such a definition remains strongly dependent on the bottom boundary and flow characteristics, therefore no particular prior definition will be chosen here, as the present study takes place over different types of beds.

Another important parameter relevant to the flow characteristics in the boundary layer needs to be defined. While the well known Reynolds number is defined as

$$R_e = \frac{u_0^2}{\nu\sigma}, \tag{2.16}$$

when boundary layer flows are studied, the boundary layer Reynolds number is commonly used and defined as

$$R_\delta = \frac{u_0\delta}{\nu} \tag{2.17}$$

where u_0 is the horizontal velocity amplitude of the flow outside the boundary layer.

2.4 Wave-induced boundary layer flow over a flat bed

Although a sea bed is rarely perfectly flat, it is worthwhile to understand the flow behaviour over a flat bed, as a starting point for the study of natural flows.

2.4.1 Governing equations

The flow characteristics in the boundary layer can be found by solving the transport equation for vorticity and stream function (2.18) derived from the Navier-Stokes equation and the Poisson equation (2.19):

$$\frac{\partial \omega}{\partial t} + u\frac{\partial \omega}{\partial x} + v\frac{\partial \omega}{\partial y} = \nu\nabla^2\omega \tag{2.18}$$

$$\omega = -\frac{\partial^2 \psi}{\partial x^2} - \frac{\partial^2 \psi}{\partial y^2} \tag{2.19}$$

where ω is the vorticity and ψ is the stream function. The boundary layer approximations used to solve these equations consider the fact that the very thin layer in the vicinity of the boundary has a very large velocity gradient $\delta u/\delta y$ and that the boundary layer thickness is much smaller than the length scale[2]. The typical theoretical horizontal velocity profiles obtained for a wave period are shown in figure 2.4. The vertical axis is now measured upwards and y equals 0 on the sea bed.
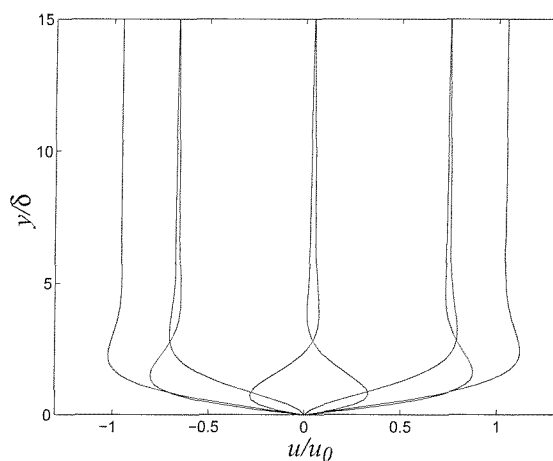
Figure 2.4: Horizontal velocity profiles during a wave period in the boundary layer, for different wave phases.

---

[2]For more information on the approximation and solution of the Navier-Stokes equations in the boundary layer, refer to Schlichting (1979).

2.4.2 Mass transport in water waves over a flat bed

One important characteristic of this flow is that the existence of a non-vanishing viscosity of the water results in the development of second-order mean velocity, relevant to the mass transport in water waves. The generation of a steady current near a solid boundary by an oscillating fluid is a well-known phenomenon. Longuet-Higgins (1953) investigated this phenomenon for sea waves propagating over a smooth flat bottom.

Mass transport velocity: Longuet-Higgins's theory

1. Mean Eulerian velocity

   The Eulerian velocity refers to the velocity as it would be measured over time at a number of fixed points in space. When the boundary layer at the free surface is considered negligible, in waves of very small steepness, a simple sinusoidal harmonic can describe the wave-induced velocity. The fundamental mode of the horizontal wave-induced velocity is $u_0 \cos(kx - \sigma t)$. For such a flow imposed at the top of the boundary layer, the laminar boundary layer solution[3] for the mean Eulerian velocity profile is

$$u_E(y) = \frac{ku_0^2}{4\sigma}\left(3 - 2(y/\delta + 2)e^{-y/\delta}\cos(y/\delta) - 2(y/\delta - 1)e^{-y/\delta}\sin(y/\delta) + e^{-2y/\delta}\right)$$

$$(2.20)$$

   where y is measured upwards from the bed. Figure 2.5 shows a typical mean velocity profile, obtained with formula (2.20).

2. Mass transport velocity in the boundary layer

   The mass transport velocity can be considered as the Lagrangian[4] time-averaged velocity. From Longuet-Higgins (1953), the definition for the mass transport velocity profile near the bottom for a progessive wave is:

$$u_L(y) = \frac{ku_0^2}{4\sigma}\left(5 - 8e^{-y/\delta}\cos(y/\delta) + 3e^{-2y/\delta}\right). \qquad (2.21)$$

---

[3]See (Phillips, 1980, p55-56).

[4]The Lagrangian velocity describes the paths that water particles would follow over time.
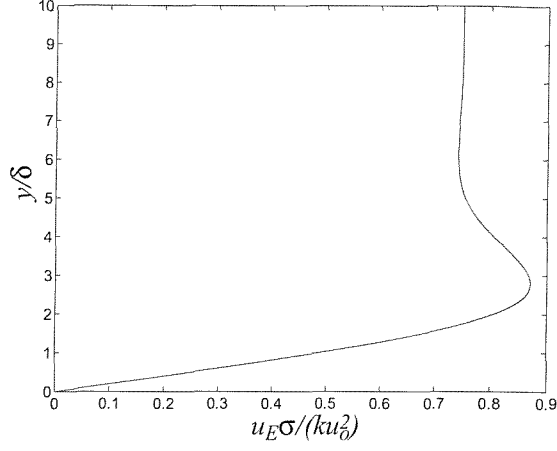
Figure 2.5: Mean Eulerian horizontal velocity obtained with formula (2.20) from Longuet-Higgins (1953).

As shown in figure 2.6, the mass transport velocity is always positive, and just
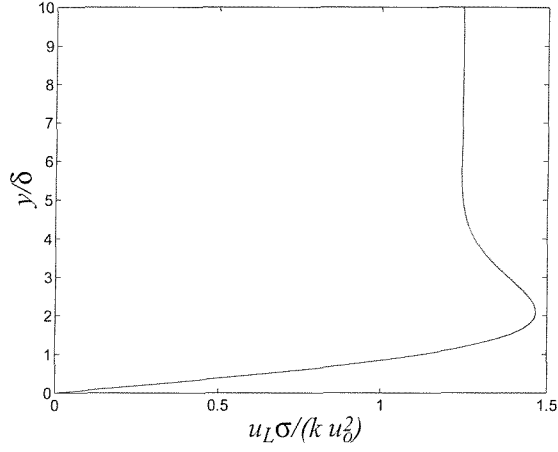
Figure 2.6: Mass transport velocity in the bottom boundary layer for a progressive wave, obtained with formula (2.21) from Longuet-Higgins (1953).

beyond the boundary layer, it tends to

$$u_L = \frac{5ku_0^2}{4\sigma}, \tag{2.22}$$

11

60% of which is the limiting Eulerian velocity $u_E|_{y=\infty}$. It is important to note that these results have been obtained with the assumption that the vorticity vanishes at the top of the boundary layer:

$$w = -\left(\frac{\partial u}{\partial y} + \frac{\partial v}{\partial x}\right) \to 0 \quad \text{as} \quad y \to \infty. \tag{2.23}$$

3. Mass transport velocity in the interior of the fluid

   Longuet-Higgins also developed two solutions for the mass transport velocity in the interior of the fluid, that is the fluid between the bottom and the free surface boundary layers. These solutions need to be mentioned as they have been used and modified by several authors when studying the mass transport inside and outside the bottom boundary layer. These solutions will also be used later in this thesis.

   Longuet-Higgins obtained two solutions: the conduction solution for a small ratio a^2/δ^2 and the convection solution when this ratio is large. The conduction solution corresponds to a vorticity diffusion through the fluid by viscous conduction. In the case of the convection solution, for large values of a^2/δ^2, the vorticity is convected with the mass transport velocity. The conduction solution is:

$$\frac{\partial \psi}{\partial y} = a^2 \sigma k F(\mu), \tag{2.24}$$

where

$$F(\mu) = \frac{1}{4\sinh^2 kd}\Big[2\cosh 2kd(\mu - 1) + 3 + kd\sinh 2kd \tag{2.25}$$
$$(3\mu^2 - 4\mu + 1) + 3(\frac{\sinh 2kd}{2kd} + \frac{3}{2})(\mu^2 - 1)\Big]$$

and

$$\mu = y/d.$$

Figure 2.7 shows different profiles of the mass transport velocity in the interior of the fluid obtained with the solution (2.24). Note that the figure 6 (p572) shown in Longuet-Higgins (1953) for the mass transport in the interior of the fluid is wrong

12
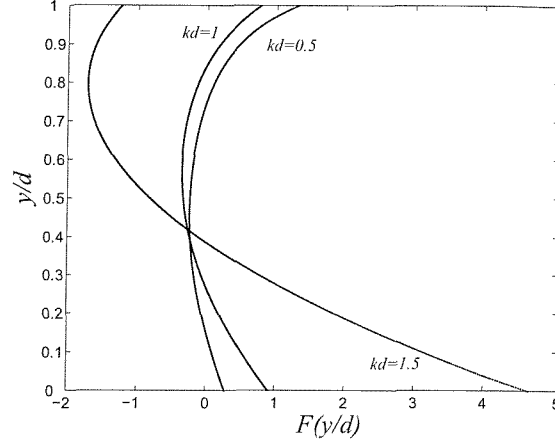
Figure 2.7: F(y/d) for different values of kd, representing the profile of the mass transport velocity (conduction solution).

for $kd = 1.5$ and y is measured downwards. The conduction solution applies when the wave amplitude is much smaller than the boundary layer thickness, which is usually untrue in practice. However, this solution is the one mainly used and referred to in literature. It can be noticed that the profiles feature significant slopes at the bed. There is a mismatch with the boundary layer solution as this latter presents a vertical profile at its top.

The second solution called the convection solution relies on more realistic assumptions, as it is valid when the wave amplitude is much larger than the boundary layer thickness. Unfortunately, the convection equation remains difficult to interpret and no solution is readily obtained. As mentioned by the author himself, this solution representing motions with non-zero total horizontal flow might also remain arbitrary.

Modifications of the theory

From Longuet-Higgins's work, several studies showed that modifications or developments of these solutions up to higher orders were needed in order to reach better

agreement with experimental data. Considering higher order sinusoidal waves is particularly necessary when a description of water waves in shallow water is needed, and consist in adding several harmonics to the fundamental mode of oscillation. Sleath (1972) considered a horizontal component of velocity just outside the boundary layer expressed in the form:

$$u_0 = u_c + u_\infty \cos(\sigma t - kx) + A\frac{u_\infty^2 k}{2\sigma} cos2(\sigma t - kx) + ... \tag{2.26}$$

where u_c is chosen to match the flow in the boundary layer; u_∞ and A are functions of the wave height[5] h, the water depth d, the angular frequency σ, and the wavenumber k. By developing the stream function as a power series in small parameter ϵ

$$\psi = \epsilon\psi + \epsilon^2\psi_2 + \epsilon^3\psi_3 + \epsilon^4\psi_4 ... \tag{2.27}$$

and solving the two-dimensional transport equation for vorticity (2.18), Sleath found a second approximation to the mass transport velocity, but no explicit solution of the mean Eulerian velocity profile was provided. However, obtaining the steady drift expression in the boundary layer can be done by using the results of Sleath (1972) and Dore (1982). The instantaneous velocity profiles can also be calculated from this stream function solution. Sleath (1973) has also numerically found three different solutions for the mass transport velocity in the interior of the fluid. The first solution is close to Longuet-Higgins's conduction solution, while the two others are distinct. The experiments conducted by Sleath in a wave tank showed that after 2 to 3 hours, mass transport velocity profiles corresponding to the second solution could be observed and after 4 hours, profiles corresponding to the third solution were observed. Profiles corresponding to the first solution, closely similar to Longuet-Higgins's conduction solution, were never observed. Swan and Sleath (1990) developed a fourth order solution for the mass transport velocity. Although their solution did not show very good agreement with measurements, it was generally better than the second order solution. They concluded that the discrepancies could be eliminated by a higher order approximation.

---

[5]The wave height h is defined as twice the wave amplitude a, so $h = 2a$.

Liu and Davies (1977) developed a modified solution of the Longuet-Higgins's conduction solution by considering a factor of viscous attenuation of the wave. Their solution does not have any restriction placed on the ratio a/δ. They concluded that the boundary layers at the free surface and at the bottom create vorticity diffusing through the interior of the fluid. The interior flow would therefore be a superposition of a potential flow (of order ka) plus a balance between the viscous forces and the local attenuation.

On the experimental side, mass transport measurements from Russell and Osorio (1957) showed that even if the condition $a \ll \delta$ was not respected, their experimental profiles were quite similar to Longuet-Higgins's conduction solution. Beech (1978) measured the mass transport velocity by Laser Doppler Anemometry. The experimental mass transport measured just outside the boundary layer was smaller but still close to the transport theoretically predicted by Longuet-Higgins's solution. The velocity profiles agreed well with the theory, but the second order effects gave larger velocities in the positive half of the cycle. Other experimental and theoretical comparisons discussing similar discrepancies can be found in Collins (1963) and Dyke and Barstow (1981).

Discussion

The Longuet-Higgins conduction solution and the modified solutions seem to have some features in common with measurements in wave tanks under laminar conditions. It is however clear that further investigations still need to be done to reach better agreement between the theory and the experiments when the mass transport velocity is concerned. In section 4.2.2, formula (2.20) is compared to some experimental mean velocity profiles. Agreement at the top of the bottom boundary layer is never reached. This problem is discussed in section 4.2.2.

It has been shown that a different approach needs to be considered for a turbulent boundary layer (see section 2.5.4). These solutions all apply to the case of a flat and

15

smooth bed. In natural conditions, say in coastal areas, the sea bed can rarely be considered as flat and smooth. Nevertheless, knowing the oscillatory flow characteristics over a flat bed such as the typical mean velocity profile (figure 2.5) and the mass transport velocity will be useful to understand the characteristics of a wave-induced oscillatory flow over a rippled bed as they should have some features in common.

2.4.3 The cnoidal theory

A different theory from Stokes theory for the description of the wave-induced velocity at the top of the boundary layer can be applied, known as the cnoidal theory. This theory for periodic waves in shallow water, has unique characteristics: the described waves are reduced to a solitary wave at one limit and to a profile expressed in terms of cosines at the other limit (Sarpkaya and Isaacson, 1981, p 178-190). In order to calculate the velocity components derived from this theory, only a small number of parameters is required compared to the Stokes theory where wave-induced velocity is obtained by adding several harmonics to the fundamental mode. Despite the fact that this theory is particularly suitable to describe water waves in shallow water, very few articles are available on theoretical or experimental investigations on boundary layers under cnoidal motion. LeMéhauté (1968) and Isaacson (1976) have developed mass transport solutions under cnoidal waves. Tanaka, Mutlu-Sumer and Lodahl (1998) give an analytical solution of the horizontal velocity and provide a study of the boundary layer thickness under the wave crests and troughs. The velocity profiles, the boundary layer thickness and the bottom shear stress obtained with their solution showed significant differences from those under sinusoidal waves.

A simple way to express the cnoidal wave-induced flow is:

$$u = u_s + \frac{cn^2 q - h_1}{1 - h_1}, \qquad (2.28)$$

16

$$
with \begin{cases}
q = K(kx - \sigma t)/\pi \\
K : \text{complete elliptic integral of the first kind} \\
E : \text{complete elliptic integral of the second kind} \\
cn : \text{Jacobian elliptic function} \\
h_1 = (\gamma - \kappa'^2)/\kappa^2 \\
\gamma = E/K \\
\kappa : \text{modulus of elliptic function} \\
\kappa'^2 = 1 - \kappa^2 : \text{complementary modulus}
\end{cases}
$$

The modulus κ is the parameter controlling the wave profile; when κ tends to 0, the profile approaches that of a Stokes first order wave profile, but when κ tends to 1, the profile tends to a solitary wave profile. For κ close to 1, the crest will be sharper and steeper, while the trough will flatten. A typical wave profile for $\kappa = 0.99$ is shown in figure 2.8. The cnoidal wave-induced velocity will fluctuate in time in a similar way to the free surface elevation curve shown in figure 2.8.
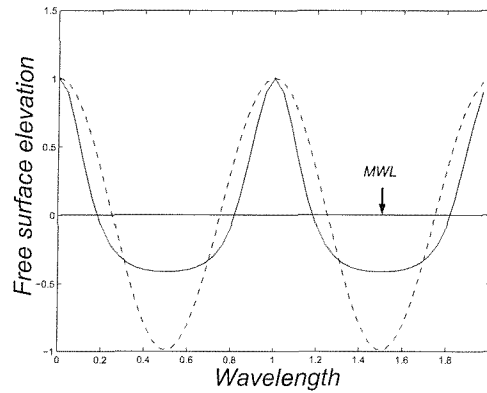
Figure 2.8: Stokes first order wave profile (- -) and cnoidal wave profile (-) for $\kappa = 0.99$ - MWL: Mean Water Level.

Isaacson (1976) derived the mass transport velocity distribution and compared it to Longuet-Higgins's solution (figure 2.9). As expected, the mean profile derived from the cnoidal solution agrees well with Longuet-Higgins's solution for small values of κ. For

17

values of κ close to 1, the mean profiles show a significant decrease. Comparisons with experimental data show a satisfactory agreement but not significantly better than the varied agreements reached between the Longuet-Higgins's solution and the experiments (see section 2.4.2).
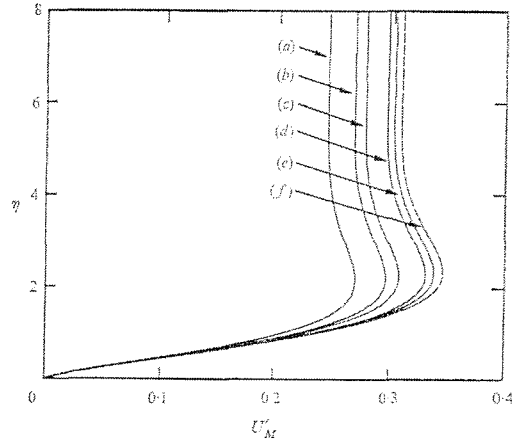
Figure 2.9: Mass transport velocity distributions through the bottom boundary layer for various values of the modulus κ: (a) $\kappa = 0.999$, (b) $\kappa = 0.995$, (c) $\kappa = 0.99$, (d) $\kappa = 0.95$, (e) $\kappa = 0.9$, (f) Solution from Longuet-Higgins(1953) for shallow water waves. Figure from Isaacson (1976); $\eta = y/\delta$ and U'_M is the mass transport velocity.

2.5 Wave-induced boundary layer flow over a rippled bed

2.5.1 Introduction

An oscillating flow over a sand bed can trigger and enhance the formation of bed ripples, with crest lines perpendicular to the ambient fluid oscillation. Oscillating flows over rippled beds are of practical and scientific interest in beach processes. Present knowledge on mean flow drift, mass transport velocity and vorticity dynamics over a

18

rippled bed is reviewed. Finally, in order to have a wider vision of the phenomenon, wave plus current cases and some features of turbulent flows over a rippled bed are discussed. When wave-induced flows over a rippled bed are studied, the relevant parameters usually considered are the wave orbital amplitude a_0, the ripple height h_r, and the ripple wavelength l_r. The ripple slope definition is

$$s_r = \frac{h_r}{l_r},$$ (2.29)

and the orbital amplitude to ripple wavelength ratio definition is

$$r = \frac{a_0}{l_r}.$$ (2.30)

2.5.2 Steady streaming recirculation cells

When the flow oscillation amplitude is small compared to the ripple wavelength and for a small h_r/δ ratio, streaming circulation cells appear. Kaneko and Honji (1979) studied experimentally and numerically these structures. They found that the steady streaming has a double structure consisting of an upper and a lower region of recirculation. Honji, Kaneko and Matsunaga (1980) confirmed it with visualizations of these cells. The upper streaming forms a pair of standing vortices above the trough, and the lower streaming a pair above the crest. The lower vortices are small compared to the upper vortices. According to Honji et al. (1980), because of the low viscosity of water, the lower vortex layer is usually so small that only the upper layer is seen. Kaneko and Honji (1979) also concluded that when the ratio of the amplitude of the wavy wall to the Stokes length is increased, the upper pair of recirculation cells moves towards the boundary in a gap between the lower pair of cells, at the trough. Matsunaga, Kaneko and Honji (1981) reached good agreement between their model and experiments conducted above a wavy wall in a flume when they studied the steady streaming and they found results similar to the conclusions of Kaneko and Honji (1979).

Sleath (1976) analytically found the same type of streaming cells for $a_0/l_r \ll 1$ and for very small ripple slopes (of order 0.03). The assumption $a_0/l_r \ll 1$ is not very realistic as in natural cases, the orbital amplitude and the ripple wavelength are usually of the same order (Nielsen, 1992). The fluid particles would appear to move along the streamline cells if they were observed each cycle at a fixed time. Figure 2.10 shows a result obtained by Sleath (1976). It can be noted that for case (a), the pair of cells has the same circulation direction as the lower pair shown in case (b). It then seems that for case (a), the only pair present is the lower pair. Hara and Mei (1990a)
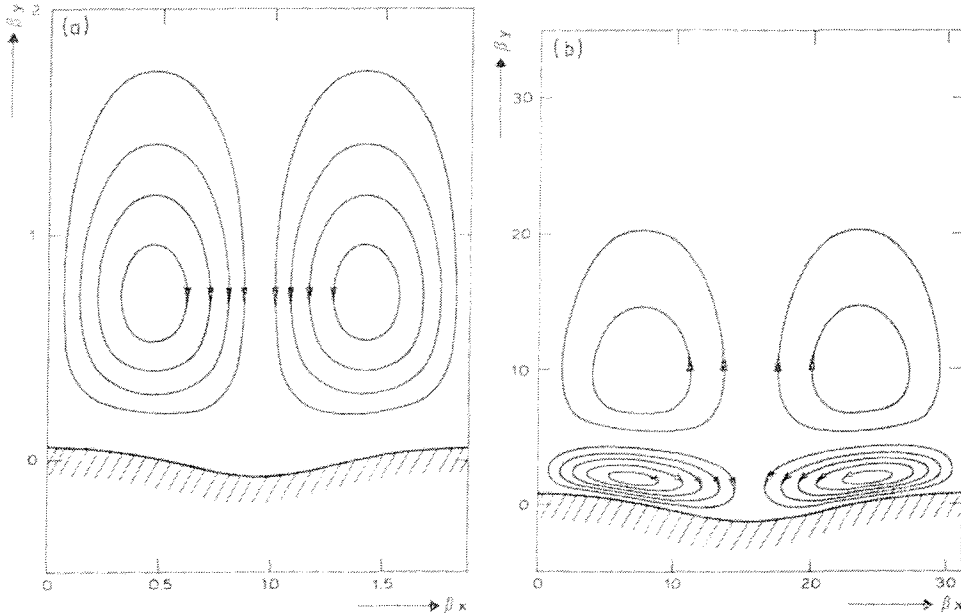
Figure 2.10: Streamlines of the mean drift velocity above a rippled bed in oscillatory flow when $a_0/l_r \ll 1$; $h_r/l_r = 0.03$; (a) $\beta l_r = 2$; (b) $\beta l_r = 30$; $\beta = 1/\delta$. Figure from Sleath (1976, figure 1, p72).

also numerically found the presence of a double pair of standing streaming cells above a rippled bed. Blondeaux and Vittori (1991) similarly concluded that the steady part of their analytical solution consisted of these recirculating cells.

20

2.5.3   Mean Eulerian velocity and mass transport velocity

As mentioned in section 2.4, the oscillatory flow generates a steady drift, but in the case of a rippled bed, calculation of this steady component appears to be more complex. Despite the experimental difficulties, some studies related to the wave-induced drift over ripples have been conducted, but the results are varied and agreement between the various experiments is not always reached. Sleath (1984b) found that for a very rough bed, the drift was enhanced compared to Longuet-Higgins's solution (for a flat bed). More recently, Marin and Sleath (1993) found that for transitional flow conditions and a rough rippled bed, the drift was reduced compared to laminar flow conditions. In their analysis, Davies and Villaret (1997) found that the Eulerian mean velocity could be either increased or decreased by time variation in the eddy viscosity.

Vittori and Blondeaux (1996) numerically found that the steady drift can take place in either direction or may have a more complex profile, with a negative mass transport close to the bed and positive far from it. They found that for a very small Reynolds number R_e the waviness of the wall was increasing the mass transport towards the shore. But when R_e was increased they stated that it was difficult to identify an overall tendency.

Ridler and Sleath (2000) experimentally found that all time-mean velocity profiles (except those at the crest and the trough) show a mean drift towards the nearest crest, in the vicinity of the bed. They pointed out that in most experiments the waves generated were nonlinear, therefore the effect of wave asymmetry would have to be considered in the Eulerian drift.

It appears that analytical and numerical works do not always agree with the experimental results. Further experimental investigations are still needed to provide a full description of the steady drift above a rippled bed. Despite being weak compared to the oscillation amplitude of the wave-induced flow, the steady drift is believed to play a significant role in carrying sand near the bed, and influencing the rippled bed shape and equilibrium (Sleath, 1976; Sleath, 1984a).

2.5.4 Vortex dynamics

It is well known that the presence of sand ripples is due to the horizontal back-and-forth motion of the water near the sea bed (Nielsen, 1981). Moreover, it is accepted that the formation of a certain type of sand ripples called vortex ripples[6] is often linked with the presence of vortex shedding at the ripple crests. Most of the flows above ripples observed in nature are not free from flow separation. Vortices provide an effective mechanism for entraining sand particles into suspension (Sleath, 1984a; Nielsen, 1992). Figure 2.11 is a schematic diagram from Earnshaw and Greated (1998) illustrating a sequence of vortex shedding over a rippled bed.

The detailed dynamics of vortex shedding and its associated sediment transport in oscillatory flow above a rippled bed is not yet completely understood. However, some experimental works provide information on this mechanism, see among others Honji et al. (1980), Sleath (1984a), Marin and Belorgey (1993), Earnshaw and Greated (1998) and Fredsøe, Andersen and Mutlu-Sumer (1999). From these authors, no definite threshold for the flow separation and vortex shedding can be chosen, however it is clear that it happens for both a larger flow oscillation amplitude to ripple wavelength ratio and a larger ripple slope than for the cases for which streaming cells are obtained. During the accelerating phase, the flow separates at the ripple crest creating a vortex structure that can trap sediment just above the lee side of the ripple. Later, the structure tends to increase in size and strength, even through the beginning of the deceleration phase. When the flow reverses, the vortex structure is convected away from the ripple crest by the local velocity, and will weaken because of viscous effects. The gravity force finally prevails, releasing the sediment to the sea bed. At the same time a new vortex is generated and after half a wave cycle, the situation is back to the first stage.

It is believed that a key feature of this flow is its three-dimensional aspect (Hara and Mei, 1990b; Blondeaux and Vittori, 1991; Earnshaw and Greated, 1998). Three-

---

[6]Other ripple types are defined in section 2.7.

22
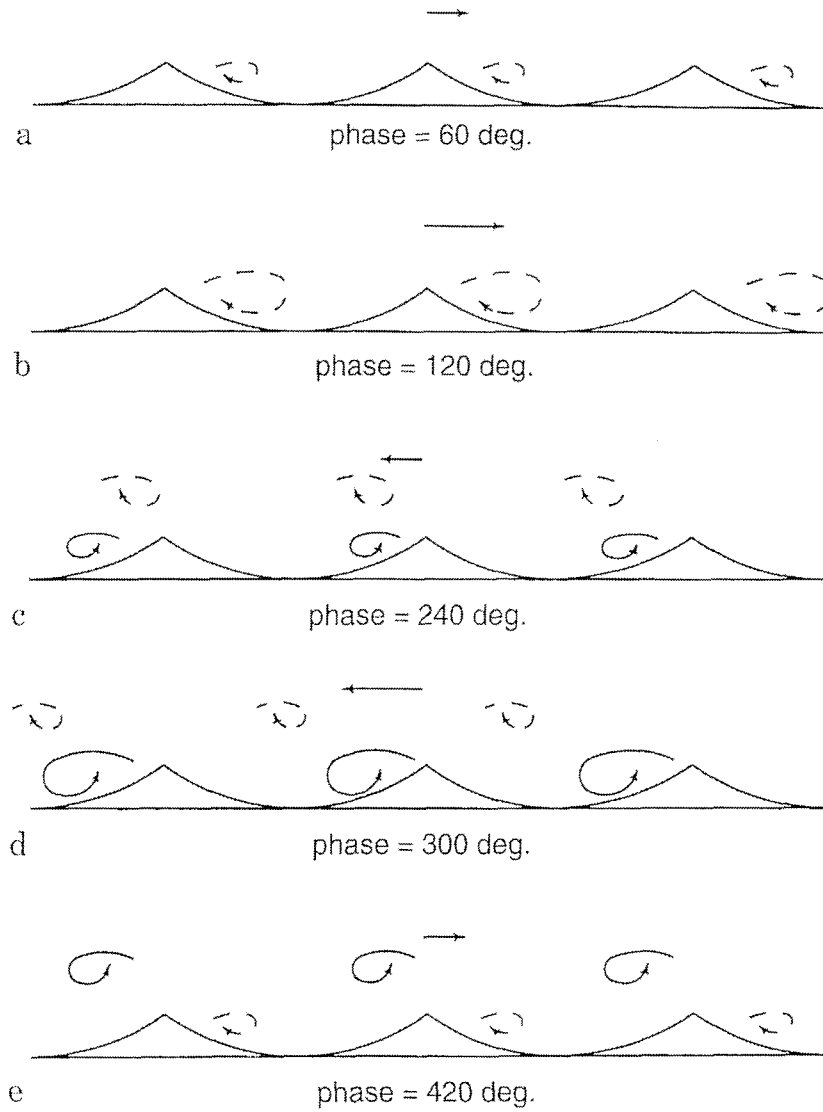
Figure 2.11: Schematic sequence of vortex shedding. The arrows indicate the flow strength and direction. Wave phases φ and vortex sizes are approximate. Figure from Earnshaw and Greated (1998).

23

dimensional instabilities as well as two-dimensional instabilities are believed to play an important role in the ripple dynamics. Due to numerical and experimental difficulties, the study of such a complex three-dimensional flow is far from complete. A model able to compute the complete three-dimensional oscillatory flow over a rippled bed is not available, but several attempts have been made to describe its features.

Hara and Mei (1990a) theoretically studied oscillatory flows over ripples. They showed the existence of vortices drifting with the flow, by tracking stationary cells in a moving coordinate system. They considered the case of fluid oscillation amplitudes of the same order as the ripple wavelength, and small ripple slopes. Blondeaux and Vittori (1991) used spectral methods and finite-difference approximations to describe the flow field close to the rippled bed. They noticed that when a vortex moves towards the bed, a recirculating cell appears underneath it. This cell is then ejected to the inviscid region, leaving in its place a free shear[7] layer that turns into another vortex. This secondary structure interacts with the first vortex and causes it to move away from the bed. This vortex pair mechanism had never been noticed before. Their model was limited to laminar flow. Scandura, Vittori and Blondeaux (2000) studied the growth of vortices above ripples by means of direct numerical simulations of Navier-Stokes and continuity equations, only for low Reynolds numbers. They found that for a fluid displacement comparable to the ripple wavelength, both flow separation and the presence of a free shear layer could destabilize the flow into a three-dimensional one. The study was extended to large oscillation fluid amplitudes and steep ripples.

Malarkey and Davies (2002) have presented two discrete vortex models for oscillatory flows over ripples, a non-viscous model with no diffusion of vorticity and a cloud-in-cell model with diffusion. They found that the simple inviscid model was giving good results in terms of vortex behaviour for cases with wave orbital amplitudes of the same order as the ripple wavelength. But when diffusion played an important role, i.e when the flow was not mainly advectively dominated, usually for orbital am-

---

[7]A free shear (mixing) layer is formed when two parallel streams with different velocities interact.

24

plitudes at least twice larger than the ripple wavelength, the cloud-in-cell model could produce more complex vortex structures and gave, as expected, better agreement with experimental data.

According to Kaneko and Honji (1979), the ejected vortices might be similar to the lower pair of standing cells mentioned in section 2.5.2, as a pair of vortices is created for a complete wave cycle and their rotation is identical to that of the recirculation cells. There are however major differences between the two cases, as for the ejected vortices, the flow separates and the pair do not interact as they do not occur at the same time.

Wave plus current case

Although the present study focuses on the wave-induced flow, it is worth considering the case where wave-induced flow coexists with a current, as it usually happens in coastal environment (e.g tidal current). The wave-current interaction in the boundary layer has been studied extensively (Bakker and Doorn, 1978; Grant and Madsen, 1986; Davies et al., 1988; Ranasoma and Sleath, 1994), but in comparison little is known on the particular case of combined waves with a current over a rippled bed (Fredsøe et al., 1999; Grant and Madsen, 1979). Fredsøe et al. (1999) carried out experiments for waves alone as well as for combined waves plus current flow, both propagating perpendicular to the ripple crests. For the case of a combined flow, the vortex generated in the lee side of the ripple could move over the ripple crest in the direction opposite to the current, as it would do in the case of a waves alone flow. They also concluded that superimposing waves on a current led to a displacement of the velocity profile to higher elevations. Ranasoma and Sleath (1994) measured fluid velocities for an oscillatory current propagating perpendicular to the ripple crests, combined with a steady current parallel to the ripple crests. Their measurements did not show good agreement with any existing model, close to the bed. Vortex formation and ejection was also noticed, by tracking the velocity fluctuations in the direction across the flow.

Although superimposing a steady current from any direction on the wave-induced flow has an effect on the velocity field, it seems that this effect is minimal in the boundary layer when only the oscillatory part of the flow is considered (Nielsen, 1992; Andersen and Faraci, 2003).

Turbulent flow

For practical reasons, very few experiments have been performed for turbulent flows over rippled beds. Several models are able to compute the turbulent wave-induced flow above a flat bed, but very few are available for the case of a rippled bed. Models dealing with a flat and rough bottom and for nonlinear waves usually obtain good agreement with the theory and the available experimental data, see among others Chowdhury, Sato and Ueno (1997), Lee and Cheung (1999), Cotton and Stansby (2000). The models generally used to described this type of fully developed turbulent flow are $k - \varepsilon$ models. Fredsøe et al. (1999) noticed that the turbulence close to the bed increased significantly when the vortex moved over the ripple crest.

Studying a fully developed turbulent flow over ripples is not the purpose of this work. Description of such a flow is very different from a laminar case and needs a different approach. Nevertheless, it is worth pointing out that flow instabilities and the kind of vortices generated over the ripples described in section 2.5.4 can be considered as the onset of turbulence starting from laminar conditions.

2.5.5 Discussion

As reviewed in the previous sections, studying the flow over a rippled bed is complex and still topical. The steady drift due to the oscillating and progressive nature of the flow has no exact analytical solution for the case of a rippled bed, and experimental studies show varied results. Steady streaming cells occurring for small ripple slopes and weak wave orbital motion to ripple wavelength ratio are a very particular feature of this flow and their influence on the flow and the sediment transport is not well known yet.

The flow separation and vortex mechanism occurring for stronger wave orbital motion to ripple wavelength ratio and stronger ripple slopes is believed to play a significant role in sediment transport (Bagnold, 1946; Nielsen, 1992). Numerical studies usually offer a good description of the vortex dynamics when compared to experimental data, but they are still limited to two-dimensional flows. Bursts of turbulence occurring in laminar flow as well as the suspected three-dimensional aspect of this flow make it even more complex to study, limiting experiments and numerical models.

The next section focuses on particular three-dimensional instabilities, triggered in laminar conditions.

2.6 Three-dimensional instabilities: centrifugal instabilities

2.6.1 Introduction

Generally speaking, instability occurs because of disturbances in the equilibrium between external forces, inertia and the viscous stresses. Instabilities occurring in a flow can be of different types, depending on the flow and boundary characteristics. The present section will focus on centrifugal instabilities triggered in laminar flow by curved boundaries.

2.6.2 Taylor-Görtler instabilities

Taylor (1923) showed that flow instability could occur between two rotating cylinders at various speeds. For a certain Taylor number[8] the flow will be destabilized by the centrifugal forces, and vortices with a regular pattern will appear. The disturbances are three-dimensional. Görtler (1941) also studied three-dimensional flow instabilities

---

[8]The Taylor number is usually defined as the ratio of the (destabilizing) centrifugal force to the (stabilizing) viscous force.

in the boundary layer for the case of a curved concave wall[9]. The assumption for the Görtler problem is that the boundary layer thickness is much smaller than the radius of curvature of the wall. For a steady flow, for a certain range of boundary layer Reynolds number R_δ and for a certain range of wall curvature R, vortex structures will tend to appear. The Görtler instability occurs in the form of steady, stream-wise oriented, counter rotating vortices. The vortex structure is spanwise periodic, as shown in figure 2.12.
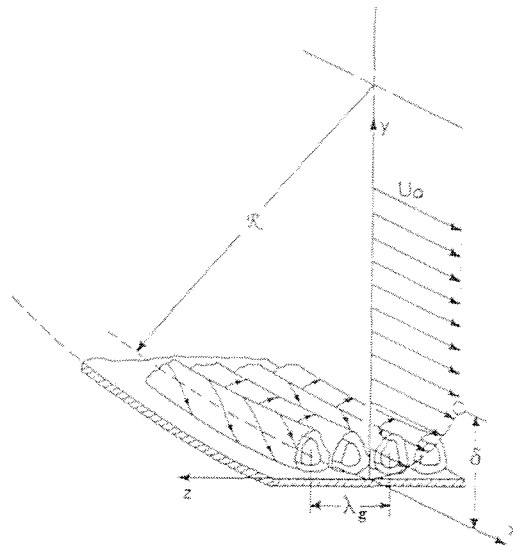
Figure 2.12: Görtler vortices over a concave wall. λ_g is the spanwise instability wavelength. R is the wall radius of curvature. Figure from Schlichting (1979), p 526, figure 17.32.

More recently, Honji (1981) showed that for the case of an oscillating cylinder in initially still water, above a certain threshold, the previously two-dimensional flow was breaking into a three-dimensional flow forming regular streak patterns over the cylinder surface, in the form of mushroom vortex chains. This instability is assumed to be centrifugal. Hall (1984) carried out a linear analysis on the stability of this

---

[9]For more information on Görtler vortices, refer to Schlichting (1979) and Saric (1994).

28

phenomenon, and obtained good agreement with Honji's experimental results. In this case, the critical parameter is the Keulegan-Carpenter number defined as

$$KC = \frac{2\pi a_d}{D_c} \tag{2.31}$$

where a_d is the amplitude of the cylinder motion and D_c the cylinder diameter.

2.6.3 Centrifugal instabilities over ripples

Oscillating flows around a cylinder and a ripple shape are analogous and one can expect Taylor-Görtler vortices or centrifugal instabilities over a rippled bed. Then from the study of centrifugal instabilities occurring along a cylinder in oscillating water (or an oscillating cylinder in still water), the idea of studying centrifugal instabilities over a rippled bed in an oscillatory flow comes next. As assumed to happen in coastal conditions (Sleath, 1984a; Hara and Mei, 1990b; Hansen et al., 2001a), these instabilities may play a significant role in the seabed shape and equilibrium. Even if ripple patterns have been studied for many years, different theories still coexist about the types of instability involved and as mentioned by Hansen et al. (2001a), centrifugal instabilities are strongly believed to be one of them.

Hara and Mei (1990b) numerically studied two cases, one for ripples of finite slope and very weak fluid oscillations, and the other for gentle ripple slopes and moderate fluid oscillations. For the latter case, the flow did not separate and it was found to be centrifugally unstable, with a periodicity of one or two ripple wavelengths. They noted that these instabilities could be relevant to the initiation of brick-pattern ripples[10] (see figure 2.13). The mushroom vortices, strongly similar to vortices visualized by Honji (1981), would be one cause for the building of the bridges between successive ripple crests.

The instability threshold was expected for a value of order one of the Taylor number

---

[10]see Bagnold (1946) and Sleath (1984a, figure 4.14, p142).
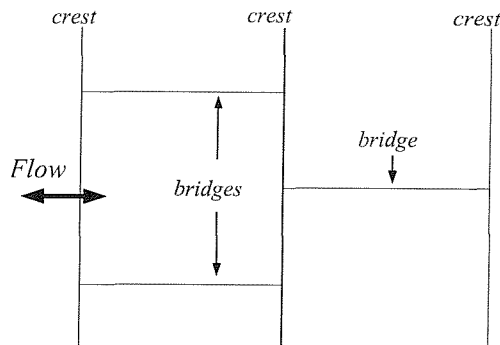
Figure 2.13: Schematic brick pattern ripples (view from above).

defined as:

$$T_a = \frac{a_0^2 h_r}{2l_r^2} \sqrt{\frac{\sigma}{\nu}}. \qquad (2.32)$$

They found that by increasing a_0/l_r to 0.48 (so increasing a_0 to nearly half the ripple wavelength), the instabilities were covering the entire wavelength and the disturbances started to interact with each other. For $a_0/l_r = 0.68$, an accumulation pattern indicated bridges formation between transverse crests that could lead to brick-pattern ripples.

Although Scandura et al. (2000) studied cases for strong fluid oscillations over steep ripples, they also found that for the case of a small fluid displacement, Taylor-Görtler vortices tended to appear.

In Hansen et al. (2001b), a tray of sand was oscillated in a tank of water. They started from already existing ripples and looked at their evolution when changing the amplitude and frequency of oscillation. They found three types of instability leading to different changes in the shape of the ripples. According to the authors, these instabilities are leading to "bulging", "doubling"[11] and "pearling" ripple patterns. The "pearling" is obtained when the driving frequency is increased: new small ripples begin to emerge in the trough of the initial ripples. The "pearling" pattern is periodic.

---

[11]The "bulging" and "doubling" patterns correspond to an increase or a decrease of the ripple wavelength.

Hansen et al. speculate that the "pearling" instability might be related to centrifugal instabilities giving rise to transverse Taylor vortices.

These studies are based on computer modelling and theoretical analysis but not on experiments, except for Hansen et al. (2001b). As seen in section 2.5.4, flow separation leading to the formation of vortices over a rippled bed in laminar flow has been and is still extensively studied, and in comparison, very little is known about centrifugal instabilities over ripples. No recent experiment has been conducted on this phenomenon. Studying the instability threshold and the velocity disturbances, and getting visualizations of this particular flow pattern, would be of great interest for many reasons. It would first help to confirm or not the existing analyses on the subject. It would also provide a better understanding in sea bed ripples formation and equilibrium, and eventually help getting a wider picture of beach processes.

2.7   Ripple characteristics review

While the previous sections use the flow characteristics to describe the physical processes, this section adds new elements to this description by reviewing different sea ripple aspects from a sediment transport approach. A short description of the common two-dimensional ripple types is provided. The formation and evolution of these two-dimensional ripples are then reviewed. Finally, a section on three-dimensional ripples is also developed.

2.7.1   Two-dimensional ripple types

Wave-induced flow over a sandy bed usually changes the bed into a pattern of regular or irregular ripples. Different classifications for regular two-dimensional ripple types can be found in literature.

Rolling-grain and vortex ripples

In Sleath (1984a), as in Bagnold (1946), two typical bed forms can be distinguished: ripples with a significant slope, so that vortices can be formed at the lee side of the crest, called *vortex ripples*, and ripples with a slope too gentle for vortex formation, called *rolling-grain ripples*. From a initially flat, or slightly wavy bed, the rolling-grain ripples will be the first to form, with a small height to wavelength ratio. According to Sleath (1984a), when this ratio exceeds 0.1, the boundary layer can separate behind the crest allowing vortex formation, leading to the vortex ripple formation. Rolling-grain ripples can be found at low to moderate sediment transport rates, if no vortex ripple is already formed, but they can also be found at high sediment transport rates, where the vortex ripple formation is not possible.

The mechanism of rolling grain ripple formation has been clearly explained by Sleath (1984a, p126-127). The steady drift added to the oscillatory motion of the fluid plays an important role: it is directed from the ripple trough to the ripple crest, so that the sediment in motion will be carried away from the trough towards the crest, enhancing the ripple growth. As the ripple height increases, the component of the gravity force opposed to the steady drift carrying particles will become stronger, so that the ripples cannot grow indefinitely. Hence, for given wave characteristics, the rippled height is limited. As mentioned by Andersen (2001), it has to be noted that rolling-grain ripples are rarely observed in the field, mainly because they are dominated by invading vortex ripples.

The vortex ripples are the ripples most commonly found for low to moderate sediment transport flows. The building of these ripples follows a process quite similar to the mechanism of rolling-grain formation. By trapping sediment in their structure, vortices will also enhance the ripple formation. However, Sleath (1984a, p134-135) pointed out that it was not clear why ripples would form for only one wavelength (for given wave conditions) when the vortex formation itself implies that the bed is unstable for all wavelength enabling vortex formation. The wavelength that would form most

32

probably is the one giving the greatest sediment transport toward the crest.

Orbital, anorbital and suborbital ripples

In Wiberg and Harris (1994), another classification is considered with three different ripple types: orbital, anorbital and suborbital ripples. Orbital ripples will have wavelengths proportional to the near-bed wave orbital amplitude, and will be mainly found in laboratory experiments. Anorbital ripples will be approximately proportional to the grain size, quite independent from the orbital amplitude, and mainly found in the field. Suborbital ripples are intermediate forms. Wiberg and Harris (1994) have constructed a method for ripple characteristics prediction avoiding distinctions between these three types, therefore distinction between flume and field cases. The discriminators used are the ratio of boundary layer thickness to ripple height and the ratio of near bed wave orbital amplitude to ripple height.

Discussion on two-dimensional ripple types

From Nielsen (1992), Fredsøe and Deigaard (1992) and Sleath (1984a), it can be concluded that depending on the wave orbital amplitude and the sediment type, the ripple formation goes from a round crested ripple to a sharp crested steep ripple allowing vortices to develop. An increase in the flow oscillation amplitude will usually lead to the formation of vortex ripples. But coarse sand will give more rounded crests. However, for a strong value of orbital motion, vortex ripples would be changed into rolling-grain ripples again. It has to be noted that plane beds can be found at very high sediment transport rates, called *sheet flow*.

2.7.2 Two-dimensional ripple shape model

Formulas from Sleath (1984a, p131-133), derived from measured experimental ripples, provide a good approximation of the ripple profiles:

$$y = \frac{h_r}{2} cos(k_r \xi),$$ (2.33)

and ξ is given by

$$x = \xi - \frac{h_r}{2} sin(k_r \xi),$$ (2.34)

where h_r is the ripple height and k_r the ripple wavenumber. These formulas are valid for ripples of a small height to length ratio. If the ripple slope is weak, the crest is rounded, and the overall shape is close to a sinusoidal profile (rolling-grain ripple type). When the ripple slope increases, the crest sharpens and the trough flattens (vortex ripple type). Figure 2.14 shows different profiles obtained using these formulas. Formula (2.33) defining a two dimensional ripple profile is adopted by the majority of researchers studying vortex ripples, see for example Sleath (1984a), Marin and Belorgey (1993), Blondeaux and Vittori (1991). In the present study, these formulas have been used both in the computer model for the definition of the domain bottom boundary (section 3.4), and in the experiments for the cutting of the rippled panels used as a sea bed (section 5.1).

Figure 2.14: Example of ripple profiles obtained with formula (2.33); (—) $s_r = 0.125$; (–) $s_r = 0.25$; (- -) $s_r = 0.32$.

2.7.3 Two-dimensional ripple characteristics predictions

The prediction of ripple geometry is necessary to the prediction of sand transport under wave action. According to the literature, the main parameter influencing the

ripple wavelength is the orbital amplitude close to the bed defined as:

$$a_0 = \frac{h}{2\sinh kd} \qquad (2.35)$$

where h is the wave height (equal to $2a$). The characteristics of the sand also play an important role. Two relevant parameters using the sand properties are usually considered to describe the ripple characteristics: the mobility number Ψ (Yalin, 1971)

$$\Psi = \frac{(a_0\sigma)^2}{(s-1)gd_{50}}, \qquad (2.36)$$

and the Shields parameter Θ

$$\Theta = \frac{u_\star^2}{(s-1)gd_{50}} = \frac{1}{2}f_w\Psi \qquad (2.37)$$

where s is the relative density of the particle, that is the ratio of the particle density over the water density, d_{50} is the grain mean diameter, and $u_\star$ is the friction velocity. The wave friction factor f_w is a function of a_0 and the roughness length $z_0 = k_s/30$, where k_s is the Nikuradse coefficient, a function of the grain diameter D. Typically, $k_s = 3D$ for fine sands and $k_s = D$ for coarse sands.

Concerning the ripple wavelength, two experimental formulas can be considered. Formula (2.38) is valid for $\Psi < 20$, while formula (2.39) covers a wider range, being valid for $2 < \Psi < 230$ (Nielsen, 1992):

$$l_r = 1.33a_0 \qquad (\Psi < 20), \qquad (2.38)$$

and

$$\frac{l_r}{a_0} = 2.2 - 0.345\Psi^{0.34} \qquad (2 < \Psi < 230). \qquad (2.39)$$

Other empirical formulas exist but they usually give good agreement with flume and field measurements for a more restricted range of orbital amplitude, wave period and sediment characteristics, as shown by O'Donoghue and Clubb (2001) and Wiberg and Harris (1994). Andersen (2001) and Andersen et al. (2001) have also developed numerical models for ripple predictions and reached reasonable agreement with experimental data.

The ripple steepness can also be predicted as a function of the Shields parameter (Nielsen, 1992):

$$\frac{h_r}{l_r} = 0.182 - 0.24\Theta_{2.5}^{1.5} \tag{2.40}$$

where $\Theta_{2.5}$ is the Shields parameter for a grain roughness of $2.5d_{50}$. In order to predict the ripple height, Nielsen (1981) found the empirical formula:

$$\frac{h_r}{a_0} = 0.275 - 0.022\sqrt{\Psi}. \tag{2.41}$$

2.7.4 Three-dimensional ripples

Formation

If the sediment transport rate increases, vortex ripples will tend to become three-dimensional, with a decrease of their steepness. As mentioned by Sleath (1984a), obtaining three-dimensional ripples in wave flumes is difficult since the two-dimensional ripples will always appear first and sometimes for several hours, resulting in a significant loss of sediment when the three-dimensional ripples are likely to form. For light sediment, the quick reformation of rolling-grain ripples might also prevent from seeing any three-dimensional effect in-between the two patterns. O'Donoghue and Clubb (2001) found that the criteria mentioned in section 2.7.3 fail when they are applied to three-dimensional ripples. They also concluded that no criterion was available for three-dimensional ripples prediction for a wide range of sand and flow conditions.

Brick-pattern ripples

For a low sediment transport rate, a particular three-dimensional ripple pattern can develop. Supposedly due to centrifugal instabilities in the form of horseshoe vortices (Sleath, 1984a), the two-dimensional vortex ripples will be changed to a similar shape but with shifted bridges linking each transverse crest, as shown in figure 2.15 (see also section 2.6.3).

36
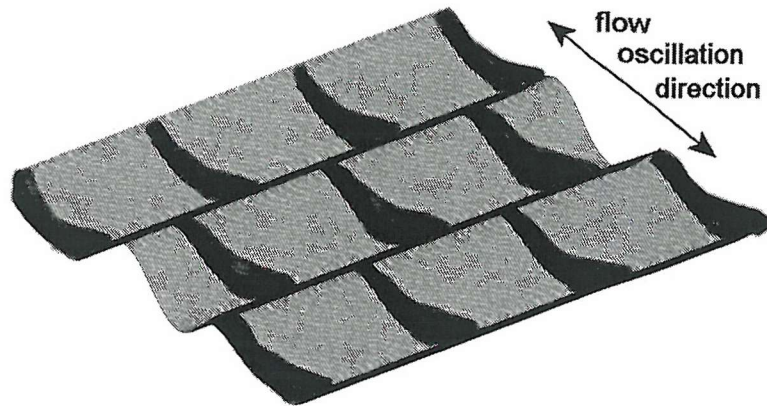
Figure 2.15: Schematic representation of the brick pattern ripples.

It appears that three-dimensional ripples tend to form from two-dimensional vortex ripples when the orbital amplitude increases or the sediment transport rate increases. However, an increase in the sediment transport rate might not lead systematically to a three-dimensional pattern, but will surely change the ripple pattern.

As for any three-dimensional ripple type, the mechanisms involved in the brick-pattern formation need further investigation.

2.8   Summary

Wave-induced flow characteristics have been reviewed for shallow water areas over flat and rippled beds. The presence of a steady drift has been pointed out. For flat bed cases, it has been shown that theory gives acceptable agreement with experiments for instantaneous velocity profiles. However, the measured mass transport velocity is usually different from the theoretical prediction. Despite being widely used, it appears that Longuet-Higgins's solutions for the boundary layer and the interior of the fluid are restricted to cases unlikely to happen in natural cases. Furthermore, it seems that there is a mismatch between the two solutions. Comparisons between experimental data, a numerical model and the theory will be shown in section 4.2.2 to provide discussions

on the discrepancies.

For a rippled bed, no complete valid theory is available yet, especially when the flow is suspected to be three-dimensional. Nevertheless, numerous experimental and numerical studies on oscillating fluids above ripples provide qualitative and quantitative information on the velocity field, the mass transport and the vorticity dynamics. It appears that the flow features depend strongly on three main factors: the ripple height, the ripple wavelength and the fluid oscillation amplitude. When the orbital amplitude is much less than the ripple wavelength, and generally for a weak ripple slope, a double pair of recirculation cells is present above each ripple wavelength. For a strong enough fluid oscillation amplitude, the flow is likely to separate and give rise to vortices. Vortex generation at the ripple crest has a significant effect on the seabed shape. For a weak flow oscillation over steep ripples or for a significant flow oscillation over gentle ripples, centrifugal instabilities are likely to happen. These particular three-dimensional instabilities are suspected to contribute to the formation of a three-dimensional ripple type called brick-pattern ripple. Very few experimental and numerical studies have been done on this particular instability.

The ripple formation itself has been widely studied. Different ripple types can be identified depending on the flow conditions and the sediment type. Various formulas mainly derived from experiments are available for the prediction of two-dimensional ripple features, but they are usually limited to a certain range of flow and sand conditions. Some numerical models have also been developed for ripple prediction, but they are still limited to a certain range of conditions and for two-dimensional ripples.

It appears that studying the wave-induced flow over ripples is a wide subject and further investigations need to be done in different areas. A complete description of such a flow under varied conditions is a huge task and cannot be done in the present thesis. However a classification of the flow features with respect to the wave and ripple characteristics would be a step further in understanding the process involved in this particular area. Providing such a classification including the study of the flow

dimension is one of the main purposes of the present thesis.

Using the general background and the problems pointed out in this review, the following chapters provide further investigations on the wave-induced flow characteristics over a rippled bed. The instantaneous velocity profiles, the mass transport velocity and the vortex mechanism are studied by means of a numerical model. Then, the vortex formation, shape and behaviour and the dimensional aspect of the flow are studied by mean of experimental visualizations.

Chapter 3

Computer Model

3.1 Introduction

A computer model aimed to calculate the flow in the area close to the bed has been written. The model is programmed in FORTRAN, and was run on Irixcompute[1] workstations. The model solves the vorticity transport equation derived from the Navier-Stokes equation and the Poisson equation for vorticity and stream function. The horizontal and vertical velocities are then calculated from the model output.

3.2 Governing equations

3.2.1 Basic equations

The equations used to solve the flow in the vicinity of the bed are the vorticity transport equation

$$\frac{\partial \omega^\star}{\partial t^\star} + u^\star \frac{\partial \omega^\star}{\partial x^\star} + v^\star \frac{\partial \omega^\star}{\partial y^\star} = \nu \nabla^2 \omega^\star, \tag{3.1}$$

and the Poisson equation

$$\omega^\star = -\frac{\partial^2 \psi^\star}{\partial x^{\star 2}} - \frac{\partial^2 \psi^\star}{\partial y^{\star 2}}, \tag{3.2}$$

---

[1]Irixcompute is based on a eight-processor Power Challenge computer from SGI.

where $\omega^\star$ is the vorticity, $\psi^\star$ the stream function and ν the water viscosity. The horizontal and vertical velocities respectively $u^\star$ and $v^\star$ are defined by

$$u^\star = \frac{\partial \psi^\star}{\partial y^\star} \qquad \text{and} \qquad v^\star = -\frac{\partial \psi^\star}{\partial x^\star}. \tag{3.3}$$

The vorticity transport equation may then be changed to

$$\frac{\partial \omega^\star}{\partial t^\star} = -\frac{\partial \psi^\star}{\partial y^\star}\frac{\partial \omega^\star}{\partial x^\star} + \frac{\partial \psi^\star}{\partial x^\star}\frac{\partial \omega^\star}{\partial y^\star} + \nu\left(\frac{\partial^2 \omega^\star}{\partial x^{\star 2}} + \frac{\partial^2 \omega^\star}{\partial y^{\star 2}}\right). \tag{3.4}$$

3.2.2 Dimensionless variables

In order to work with dimensionless variables, the following scales are chosen:

- The length scale is the Stokes boundary layer length $\delta^\star$ defined as

$$\delta^\star = \sqrt{\frac{\nu T^\star}{\pi}}$$

  where $T^\star$ is the water wave period.

- The time scale is

$$\frac{T^\star}{2\pi}.$$

- The velocity scale is $U_0^\star$, that is the amplitude of the horizontal velocity oscillation just outside the considered area.

The dimensionless variables can then be introduced:

$$t = \frac{t^\star 2\pi}{T^\star},$$

$$(x, y) = \frac{(x^\star, y^\star)}{\delta^\star},$$

$$\omega = \frac{\omega^\star \delta^\star}{U_0^\star},$$

$$\psi = \frac{\psi^\star}{U_0^\star \delta^\star}.$$

41

The boundary layer Reynolds number R_δ is also used, defined here as:

$$R_\delta = \frac{U_0^\star \delta^\star}{\nu}. \tag{3.5}$$

Equation (3.4) and (3.2) can then be expressed in dimensionless forms:

$$\frac{2}{R_\delta}\frac{\partial \omega}{\partial t} = -\frac{\partial \psi}{\partial y}\frac{\partial \omega}{\partial x} + \frac{\partial \psi}{\partial x}\frac{\partial \omega}{\partial y} + \frac{1}{R_\delta}\left(\frac{\partial^2 \omega}{\partial x^2} + \frac{\partial^2 \omega}{\partial y^2}\right) \tag{3.6}$$

and

$$\omega = -\frac{\partial^2 \psi}{\partial x^2} - \frac{\partial^2 \psi}{\partial y^2}. \tag{3.7}$$

Equation (3.6) is rearranged to:

$$\frac{\partial \omega}{\partial t} = \frac{R_\delta}{2}\left(\frac{\partial \psi}{\partial x}\frac{\partial \omega}{\partial y} - \frac{\partial \psi}{\partial y}\frac{\partial \omega}{\partial x}\right) + \frac{1}{2}\left(\frac{\partial^2 \omega}{\partial x^2} + \frac{\partial^2 \omega}{\partial y^2}\right). \tag{3.8}$$

3.3 Algorithm for a flat bed case

In order to solve the flow characteristics in the boundary layer for the case of a wave-induced flow a model has been programmed in FORTRAN, using a calculation algorithm similar to the one proposed by Roache (1972) concerning the main loops.

3.3.1 Discrete formulation

The vorticity transport equation (3.8) and the Poisson equation (3.7) can be expressed in a discrete form using a finite-difference scheme. Each term from these equations can be expressed as a finite-difference, using vorticity and stream function values at different points of a previously defined grid, of index i from 0 to i_m for the horizontal axis and index j from 0 to j_m for the vertical axis (figure 3.1). The discrete form of each term is then:

$$\frac{\psi_{i+1,j} - \psi_{i-1,j}}{2\Delta x} \quad \text{for} \quad \frac{\partial \psi}{\partial x}, \tag{3.9}$$

$$\frac{\psi_{i,j+1} - \psi_{i,j-1}}{2\Delta y} \quad \text{for} \quad \frac{\partial \psi}{\partial y}, \tag{3.10}$$

42

$$\frac{\omega_{i+1,j} - \omega_{i-1,j}}{2\Delta x} \qquad \text{for} \qquad \frac{\partial \omega}{\partial x}, \tag{3.11}$$

$$\frac{\omega_{i,j+1} - \omega_{i,j-1}}{2\Delta y} \qquad \text{for} \qquad \frac{\partial \omega}{\partial y}, \tag{3.12}$$

$$\frac{\omega_{i+1,j} - 2\omega_{i,j} + \omega_{i-1,j}}{\Delta x^2} \qquad \text{for} \qquad \frac{\partial^2 \omega}{\partial x^2}, \tag{3.13}$$

$$\frac{\omega_{i,j+1} - 2\omega_{i,j} + \omega_{i,j-1}}{\Delta y^2} \qquad \text{for} \qquad \frac{\partial^2 \omega}{\partial y^2}, \tag{3.14}$$

$$\frac{\omega_{i,j}^{t+\Delta t} - \omega_{i,j}^{t}}{\Delta t} \qquad \text{for} \qquad \frac{\partial \omega}{\partial t}. \tag{3.15}$$

The vorticity transport equation (3.8) can then be expressed in its discrete form:

$$\omega_{i,j}^{t+\Delta t} = \omega_{i,j}^{t} + \Delta t[A] \tag{3.16}$$

where $[A]$ is the discrete form of the right-hand side terms of equation (3.8), all expressed above. The discrete form of the Poisson equation is:

$$\omega_{i,j} = -\left(\frac{\omega_{i+1,j} - 2\omega_{i,j} + \omega_{i-1,j}}{\Delta x^2} + \frac{\omega_{i,j+1} - 2\omega_{i,j} + \omega_{i,j-1}}{\Delta y^2} \right). \tag{3.17}$$
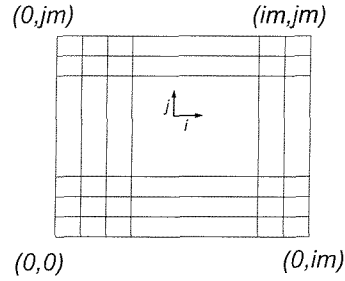
Figure 3.1: Computing grid.

3.3.2   Initial conditions

- The number of points defining the calculation grid is set[2] (typically 80 by 80 points).

---

[2]see section 4.2.1 for convergence tests on grid size.

43

- The wave period $T^\star$ and the velocity amplitude $U_0^\star$ at the top of the domain are defined. The boundary layer Reynolds number R_δ is then calculated with formula (3.5).

- The domain length is defined equal to the wave wavelength L.

- The domain height is defined equal to a multiple of the Stokes length or to a chosen value (typically a few centimetres).

- The mesh sizes Δx and Δy are calculated with the domain size and the number of points defining the grid.

- The time-step and the total time of calculation are defined. The time-step Δt is a fraction of the dimensionless wave period: $\Delta t = 2\pi/N$ where N is an integer number[3].

- At instant $t = 0$, all vorticity and stream function values are set equal to 0.

3.3.3   Boundary conditions

1. **On the bottom of the domain**

    - The stream function is null for $y = 0$

    $$\psi_0 = 0. \tag{3.18}$$

    - A Woods condition is applied for the vorticity:

    If ψ_0 is any point on the sea bed and ψ_1 is the point just above it, we have

    $$\psi_1 = \psi_0 + \frac{\partial \psi}{\partial y}\Delta y + \frac{1}{2}\frac{\partial^2 \psi}{\partial y^2}(\Delta y)^2.$$

    As $U_{bed} = \dfrac{\partial \psi}{\partial y} = 0$, it follows that:

    $$\frac{\partial^2 \psi}{\partial y^2} = 2\frac{(\psi_1 - \psi_0)}{(\Delta y)^2}.$$

---

[3]see section 4.2.1 for the choice of N.

44

As $\dfrac{\partial^2 \psi}{\partial x^2} = 0$ on the bed, we also have:

$$\omega_0 = -\frac{\partial^2 \psi}{\partial y^2}.$$

Then with condition (3.18), the Woods condition is:

$$\omega_0 = -\frac{2\psi_1}{(\Delta y)^2}. \tag{3.19}$$

2. On the top of the domain

- The horizontal velocity imposed at the top of the domain is:

$$\frac{\partial \psi}{\partial y} = u_s + U_0 \cos(\sigma t - kx) \tag{3.20}$$

This imposed velocity represents the wave-induced velocity where only the fundamental mode is shown, but in several cases other harmonic terms may be added to the definition (see section 4.2.2). The velocity u_s is the value that has to be chosen to match the steady drift value at the top of the domain. The choice of the steady drift value is an important issue (Riley, 1978). Three different methods can be used for the choice of u_s. The top mean vorticity can be minimized by a specific loop: by simple bisection, a value of u_s is chosen for the smaller possible top mean vorticity. Figure 3.2 is an example showing the final value of u_s chosen for the minimum vorticity found with this loop. The velocity u_s can also be set equal to the top value of the mean Eulerian theoretical velocity obtained with formula (2.20). But u_s can also be set equal to the top value of a mean experimental velocity. All three methods are discussed in section 4.2.

- As described by the theory, the vorticity on top of the domain should be null. As the top vorticity is minimized (see previous point) and is very weak, instead of imposing a zero vorticity value at the top of the domain, a simple condition is applied:

$$\omega_{i,j_m} = \omega_{i,j_m-1} \tag{3.21}$$

45
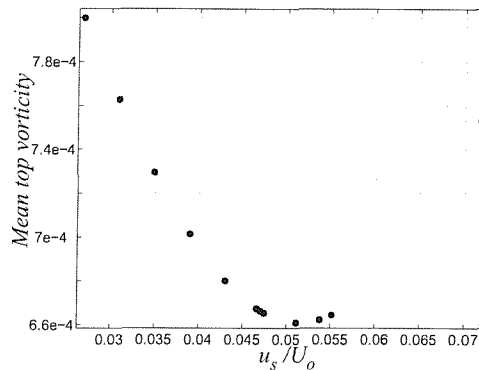
Figure 3.2: Mean vorticity at the top of the domain for different values of u_s.

where the top vorticity is set equal to the value of vorticity at the point just underneath (see grid example on figure 3.1).

3. **On the sides of the domain:**

Values of point outside the defined grid (left and right sides) will be needed in order to calculate the vorticity and stream function values along the edges of the domain. For both variables, as the domain is symmetrical (equal to one wavelength), any value needed just outside the right side will be taken equal to the last corresponding value on the left side at the same elevation. In the same way, any value needed just outside the left side of the domain will be put equal to the first value of the right side of the domain. On a finite-difference point of view, any value of the stream function ψ or the vorticity ω of index $i = 0$ or $i = i_m$ will need, in order to be calculated, values outside the mesh, say $i = -1$ and $i = i_m + 1$, so non-existing values. Any variable of index $i = -1$ will then be replaced by the same variable of index $i = i_m$; the same way, any variable of index $i = i_m + 1$ will be replaced by the same variable of index $i = 0$. In other words, for any j:

$$\psi_{-1,j} = \psi_{i_m,j} \qquad , \qquad \psi_{i_m+1,j} = \psi_{0,j} \tag{3.22}$$

46

and

$$\omega_{-1,j} = \omega_{i_m,j} \qquad , \qquad \omega_{i_m+1,j} = \omega_{0,j}. \tag{3.23}$$

3.3.4 Main loops

The main loop of the model is a time loop, calculating the vorticity and stream function values at any point of the mesh, each time-step. This main structure includes three important loops:

1. **The vorticity loop:**

   It calculates the vorticity at any point except at the top and bottom of the domain using formula (3.16), the discrete form of equation (3.8).

2. **The stream function loop:**

   It calculates the stream function at any point except on the bottom line[4] using formula (3.17), the discrete form of equation (3.7). A *Successive Over Relaxation* loop is done for each iteration, increasing the calculation accuracy. This method can be explained as follows: if five points are defined anywhere in the grid as shown in figure 3.3, then ψ_0 is calculated using the formula
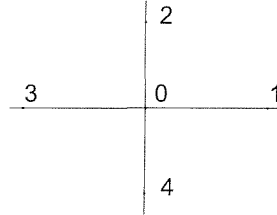
Figure 3.3: Mesh example.

$$\psi_0 = \psi_0^p + \frac{\lambda}{2(1 + \beta_\Delta^2)}(\psi_1 + \psi_3 + \beta_\Delta^2\psi_2 + \beta_\Delta^2\psi_4 + J\Delta x^2\omega_0 - 2(1 + \beta_\Delta^2)\psi_0^p) \tag{3.24}$$

---

[4]See boundary condition (3.18)

with:

- ψ_0^p : previous value of ψ at point 0
- $\beta_\Delta = \dfrac{\Delta x}{\Delta y}$
- λ: convergence parameter set to 1.65 .

This calculation is repeated until $|\psi_0 - \psi_0^p| \leq \varepsilon \psi_0$, for each time-step, with ε as the convergence parameter. (ε *is set to* 10^{-5}).

3. **The vorticity boundary loop:**

   It calculates the vorticity values at the bottom using the Woods condition (3.19), and at the top of the domain using the boundary condition (3.21).

3.3.5   Convergence criteria

- A convergence criterion is applied on the time-step Δt (Roache, 1972):

$$\Delta t \leq \frac{R_\delta}{2} \Big(\frac{1}{\Delta x^2} + \frac{1}{\Delta y^2} \Big)^{-1}. \tag{3.25}$$

- The Courant condition for both axes must also be satisfied:

$$u \frac{\Delta t}{\Delta x} + v \frac{\Delta t}{\Delta y} \leq 1. \tag{3.26}$$

3.4   Algorithm for a rippled bed case

The equations and the boundary conditions used in the model have to be modified for the case of a rippled boundary.

3.4.1   Modified equations

A wavy bottom profile is considered, described by the following equations:

$$x^\star = \xi^\star - \frac{h_r^\star}{2} \sin(k_r^\star \xi^\star), \tag{3.27}$$

$$y^\star = \frac{h_r^\star}{2} \cos(k_r^\star \xi^\star), \tag{3.28}$$

48

where $h_r^\star$ is the ripple height, $k_r^\star$ is the ripple wavenumber and $\xi^\star$ is a dummy variable[5]. The bed profile will then have crests sharper than troughs, as observed for real sea beds (Sleath, 1984a). The dimensionless ripple wavelength l_r and height h_r are

$$(l_r, h_r) = \frac{(l_r^\star, h_r^\star)}{\delta^\star}$$

and the dimensionless ripple wavenumber k_r is:

$$k_r = k_r^\star \delta^\star.$$

In order to solve the equations (3.6) and (3.7) a new orthogonal coordinate system (ξ, η) is used:

$$x = \xi - \frac{h_r}{2} e^{-k_r \eta} \sin(k_r \xi), \qquad (3.29)$$

$$y = \eta + \frac{h_r}{2} e^{-k_r \eta} \cos(k_r \xi). \qquad (3.30)$$

This system will map the sea bed profile into the line $\eta = 0$. The real domain is shown in figure 3.4.
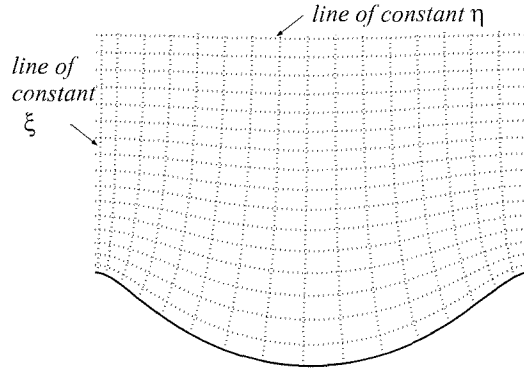
Figure 3.4: Grid in real domain.

By substituting (3.29, 3.30) into (3.6, 3.7), we get the new system of equations:

$$\frac{\partial \omega}{\partial t} = \frac{R_\delta}{2J} \left(-\frac{\partial \psi}{\partial \eta} \frac{\partial \omega}{\partial \xi} + \frac{\partial \psi}{\partial \xi} \frac{\partial \omega}{\partial \eta} \right) + \frac{1}{2J} \left(\frac{\partial^2 \omega}{\partial \xi^2} + \frac{\partial^2 \omega}{\partial \eta^2} \right), \qquad (3.31)$$

---

[5]Examples of ripple profiles obtained with the formulas (3.27) and (3.28) are shown in figure 2.14, section 2.7.2.

49

$$Jw = -\frac{\partial^2\psi}{\partial\xi^2} - \frac{\partial^2\psi}{\partial\eta^2} \qquad (3.32)$$

where J is the Jacobian of transformation

$$J = \frac{\partial(x,y)}{\partial(\xi,\eta)}. \qquad (3.33)$$

With (3.29) and (3.30), it follows that:

$$J = 1 + \frac{1}{4}h_r^2 k_r^2 e^{-2k_r\eta} - h_r k_r e^{-k_r\eta}\cos(k_r\xi). \qquad (3.34)$$

The velocity definitions are also changed to:

$$u = \frac{\partial\psi}{\partial\xi}\frac{\partial\xi}{\partial y} + \frac{\partial\psi}{\partial\eta}\frac{\partial\eta}{\partial y}, \qquad (3.35)$$

$$v = -\frac{\partial\psi}{\partial\xi}\frac{\partial\xi}{\partial x} - \frac{\partial\psi}{\partial\eta}\frac{\partial\eta}{\partial x}. \qquad (3.36)$$

Then with the Cauchy-Riemann equations

$$\frac{\partial x}{\partial\xi} = \frac{\partial y}{\partial\eta} \qquad , \qquad \frac{\partial x}{\partial\eta} = -\frac{\partial y}{\partial\xi} \qquad (3.37)$$

$$\frac{\partial\xi}{\partial x} = \frac{\partial\eta}{\partial y} \qquad , \qquad \frac{\partial\xi}{\partial y} = -\frac{\partial\eta}{\partial x} \qquad (3.38)$$

and formula (3.33), we can write:

$$\frac{\partial\xi}{\partial x} = \frac{\partial\eta}{\partial y} = \frac{1}{J}\frac{\partial x}{\partial\xi} = \frac{1}{J}\frac{\partial y}{\partial\eta}, \qquad (3.39)$$

$$\frac{\partial\xi}{\partial y} = -\frac{\partial\eta}{\partial x} = -\frac{1}{J}\frac{\partial x}{\partial\eta} = \frac{1}{J}\frac{\partial y}{\partial\xi}. \qquad (3.40)$$

After substitutions, (3.35) and (3.36) become:

$$u = \frac{1}{J}\left(\frac{\partial\psi}{\partial\xi}\frac{\partial y}{\partial\xi} + \frac{\partial\psi}{\partial\eta}\frac{\partial x}{\partial\xi}\right), \qquad (3.41)$$

$$v = \frac{1}{J}\left(\frac{\partial\psi}{\partial\eta}\frac{\partial y}{\partial\xi} - \frac{\partial\psi}{\partial\xi}\frac{\partial x}{\partial\xi}\right). \qquad (3.42)$$

The parameters $\frac{\partial x}{\partial\xi}$ and $\frac{\partial y}{\partial\xi}$ are calculated from definitions (3.29) and (3.30):

$$\frac{\partial x}{\partial\xi} = 1 - \frac{k_r h_r}{2}e^{-k_r\eta}\cos(k_r\xi), \qquad (3.43)$$

$$\frac{\partial y}{\partial\xi} = -\frac{k_r h_r}{2}e^{-k_r\eta}\sin(k_r\xi). \qquad (3.44)$$

50

3.4.2 Discrete formulation

As done in section 3.3.1, equations (3.31) and (3.32) can be expressed in a discrete form using a finite-difference scheme. Each term from these equations can be expressed as a finite-difference. The discrete form of each term is:

$$\frac{\psi_{i+1,j} - \psi_{i-1,j}}{2\Delta\xi} \qquad \text{for} \qquad \frac{\partial\psi}{\partial\xi}, \tag{3.45}$$

$$\frac{\psi_{i,j+1} - \psi_{i,j-1}}{2\Delta\eta} \qquad \text{for} \qquad \frac{\partial\psi}{\partial\eta}, \tag{3.46}$$

$$\frac{\omega_{i+1,j} - \omega_{i-1,j}}{2\Delta\xi} \qquad \text{for} \qquad \frac{\partial\omega}{\partial\xi}, \tag{3.47}$$

$$\frac{\omega_{i,j+1} - \omega_{i,j-1}}{2\Delta\eta} \qquad \text{for} \qquad \frac{\partial\omega}{\partial\eta}, \tag{3.48}$$

$$\frac{\omega_{i+1,j} - 2\omega_{i,j} + \omega_{i-1,j}}{\Delta\xi^2} \qquad \text{for} \qquad \frac{\partial^2\omega}{\partial\xi^2}, \tag{3.49}$$

$$\frac{\omega_{i,j+1} - 2\omega_{i,j} + \omega_{i,j-1}}{\Delta\eta^2} \qquad \text{for} \qquad \frac{\partial^2\omega}{\partial\eta^2}, \tag{3.50}$$

$$\frac{\omega_{i,j}^{t+\Delta t} - \omega_{i,j}^{t}}{\Delta t} \qquad \text{for} \qquad \frac{\partial\omega}{\partial t}. \tag{3.51}$$

Equation (3.31) can then be expressed in its discrete form:

$$\omega_{i,j}^{t+\Delta t} = \omega_{i,j}^{t} + \Delta t [A] \tag{3.52}$$

where $[A]$ is the discrete form of the right-hand side terms of equation (3.31), all expressed above. The discrete form of the Poisson equation (3.32) is:

$$\omega_{i,j} = -J\left(\frac{\omega_{i+1,j} - 2\omega_{i,j} + \omega_{i-1,j}}{\Delta\xi^2} + \frac{\omega_{i,j+1} - 2\omega_{i,j} + \omega_{i,j-1}}{\Delta\eta^2}\right). \tag{3.53}$$

3.4.3 Initial conditions

Initial conditions similar to the flat bed case are used (section 3.3.2), except for the domain size. A few other initial conditions need to be defined:

- The ripple wavelength l_r and ripple height h_r are defined.

- The real domain length is then defined equal to a ripple wavelength, while the domain height is a fraction of the ripple wavelength (typically 2/3).

- The mesh sizes $\Delta\eta$ and $\Delta\xi$ are calculated with l_r, h_r and the number of points defining the grid.

3.4.4 Boundary conditions

1. **On the bottom of the domain**

   - The stream function is null for $\eta = 0$

   $$\psi_0 = 0. \tag{3.54}$$

   - A Woods condition[6] similar to the flat bed case is applied for the vorticity:

   $$\omega_0 = -\frac{2\psi_1}{(\Delta\eta)^2}. \tag{3.55}$$

2. **On the top of the domain:**

   - The horizontal velocity imposed at the top of the domain is:

   $$\frac{\partial\psi}{\partial\eta} = U_0\cos(\sigma t). \tag{3.56}$$

   This imposed velocity represents the wave-induced velocity in a shallow water case, where it is considered that the wavelength of the wave is much larger than the water depth and the ripple wavelength. On the scale of a ripple wavelength, it is considered that the fluid is oscillating uniformly[7], through the entire domain. Therefore, the term kx in $\cos(\sigma t - kx)$ disappears, and so does the steady drift term u_s.

---

[6]see boundary condition (3.19)

[7]See figure 2.3

52

- The boundary condition (3.21) for the vorticity remains unchanged.

3. **On the sides of the domain**

   The boundary conditions are similar to the ones applied in the flat bed case (see section 3.3.3).

3.4.5 Main loops

The structure of the calculation loops is similar to the flat bed case model (see section 3.3.4).

3.4.6 Convergence criteria

The convergence criteria are similar to the ones applied in the flat bed case (see section 3.3.5).

Chapter 4

Model results

4.1 Introduction

In this chapter, results obtained with the numerical model are presented. Convergence tests have been done for the case of a flat bed, using the available theory for comparison. The model output is then compared to experimental data for the case of a flat bed. Discrepancies between the experimental data, the model output and the theory are discussed and further investigations are done by bringing some modifications to the model. Then the model is run for rippled bed cases and the results are compared to another numerical model and a set of experimental data. Particular flow features are then studied such as the steady streaming recirculation cells above the rippled boundary[1] and the mean Eulerian velocity profiles at different locations along the ripple.

4.2 Flat bed case

Convergence tests on the model have been done for the case of a flat bed, as the existing theoretical solution offers a convenient base for comparison. The model output

---

[1]See section 2.5.2.

is then compared to a set of experimental data in order to check the model ability to predict the flow features over a flat bed, before testing it for rippled bed cases in section 4.3. Mean Eulerian velocities from the model are also compared to the theoretical solution. Finally, tests on the vorticity behaviour at the top of the computed domain are done to explain the discrepancies obtained when the modelled and the experimental mean Eulerian velocities are compared.

4.2.1 Convergence tests

Grid size

By changing the number of points i_m and j_m defining the calculation grid[2] along the horizontal and vertical axes, the influence of the mesh sizes Δx and Δy is checked against the maximum time-mean velocities and the time-mean velocity profiles (see figure 4.1). Convergence is quickly reached and a grid of size 80 by 80 points will then be chosen for most cases.

Time-step

In figure 4.2, the mean vorticity over a wave period is plotted with decreasing values of the time-step Δt. Convergence is reached for $\Delta t < 2\pi/12000$.

4.2.2 Comparisons with experimental data

Experimental characteristics

The experimental data have been kindly provided by Mouazé (2001). Two series of experiments have been conducted by Mouazé (2001) in two different wave flumes, both aiming to measure the velocity field in the bottom boundary layer under waves. One series of experiment was set in the Franzius institute wave flume in Hanover and the other series was set in the university of Caen wave flume. The dimensions for the

---

[2]see figure 3.1
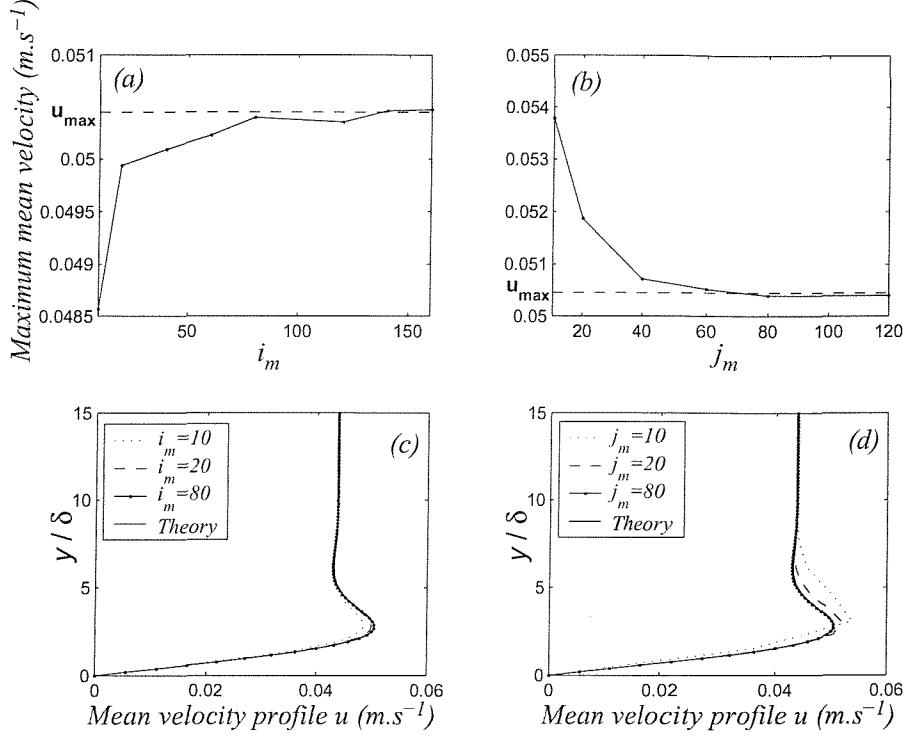
Figure 4.1: Convergence of the time-mean velocity for different values of i_m and j_m.
$i_m = L/(\delta \Delta x)$; $j_m = 0.01/(\delta \Delta y)$; $\delta = \sqrt{\nu T/\pi}$. $T = 1.33$ s; $L = 2.39$ m; $u_0 = 0.1049$
$m.s^{-1}$. *(a) and (b): maximum time-mean velocity for different values of i_m and j_m.*
(c) and (d): time-mean velocity profiles for different values of i_m and j_m compared to
the theoretical profile obtained with formula (2.20). Tests on i_m: value default for j_m
is 80. Tests on j_m: value default for i_m is 80.

Hanover wave flume are: 120 m in length, 2.2 m in width with a still water depth of
1.0 m and a floor roughness of 0.8 mm. In Caen, the wave flume is 22 m long, 0.8 m
wide with a still water depth of 0.5 m and its floor can be considered as smooth. Both
wavemakers have active absorption control; reflections from the beach were around
10% in the Hanover flume and much smaller in the Caen flume. The experimental
flow characteristics are shown in table 4.1. Mouazé (2001) optically determined the
Nikuradse coefficient k_s. With the diagram from Kamphuis (1975), it was then possible
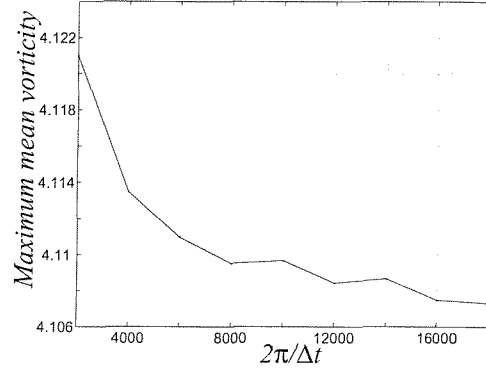
Figure 4.2: Convergence of the mean vorticity for decreasing time-steps. The flow characteristics are similar to those in figure 4.1.

to determine the bed friction factor f_w, and then the flow regimes. From Mouazé (2001), the flow is always laminar for the Caen cases, and in a transitional state for the Hanover cases.

Case	T(s)	h (m)	L (m)	u_0 $(m.s^{-1})$
C1	1.33	0.08	2.39	0.1045
C2	1.5	0.13	2.82	0.1953
C3	1.8	0.16	3.57	0.2822
C4	2.2	0.16	4.53	0.287
H1	2.0	0.15	5.21	0.1538
H2	3.0	0.15	8.69	0.196
H3	3.5	0.22	10.36	0.2194
H4	5.0	0.18	15.24	0.2655

Table 4.1: Experimental flow characteristics from Mouazé (2001).

Model input

All the parameters needed to run the computer model (wave period, wavelength, wave-induced velocity) are taken from the experimental data. In order to get a velocity definition at the top of the domain close enough to the experimental profile, a Fourier analysis is made on the experimental velocity fluctuation (during a wave period) at a certain depth (corresponding to the computed domain height, typically 10 mm) and the fundamental harmonic and other significant subharmonic coefficients are found. The velocity definition will then be:

$$u = u_s + u_{0c}\cos(\sigma t - kx) + u_{0s}\sin(\sigma t - kx) + u_{1c}\cos 2(\sigma t - kx) + u_{1s}\sin 2(\sigma t - kx)... \quad (4.1)$$

where u_{0c} and u_{0s} are the maximum velocity amplitudes of the fundamental mode for the cosine and sine terms respectively; u_{1c} and u_{1s} are the maximum velocity amplitudes of the first subharmonic for the cosine and sine terms respectively. u_s is the mean experimental velocity calculated for one wave cycle at a height of 10 mm, and will be used as the steady component value.

Comparison results

- ### Gentle case: Caen1

    In this case, the wave period is 1.33 s and the wavelength is 2.39 m. Figure 4.3 shows that the velocity profile on top of the studied domain ($y = 10$ mm) can be modelled by a simple cosine shape

    $$u = u_s + u_0 \cos(\sigma t - kx)$$

    where $u_0 = 0.1045$ $m.s^{-1}$ and $u_s = 0.0031$ $m.s^{-1}$. The modelled velocity profiles for different wave phases, from the bottom to an elevation of 10 mm are shown in figure 4.4 and compared to the experimental data and the profiles calculated from the second order theory (see Sleath (1972) and section 2.4.2). Agreement between the experimental data, the theory and the model results is good. However, if

Figure 4.3: Gentle case - Caen 1 - Horizontal velocity at the top of the domain. Comparison Model (+) / Experimental data (-) .

the mean Eulerian velocity is calculated for one wave period, agreement is less satisfactory, as shown in figure 4.5. The mean Eulerian velocity profiles from the experimental data and the Longuet-Higgins theory[3] are close in the vicinity of the bed. It has to be noted that the mean flow calculated from the model cannot be similar to the theoretical mean Eulerian flow as the velocity imposed at the top of the computed domain uses the steady component taken from the calculation of the mean experimental velocity at $y = 10$ mm and not the theoretical value for the steady drift in these conditions[4]. In this case $u_s = 0.0031$ $m.s^{-1}$ while the theory predicts a value of 0.0046 $m.s^{-1}$.

- **Steep wave Case: Caen 4**

    In this case, the wave period is 2.2 s and the wavelength is 4.53 m. Figure 4.6 shows the modelled velocity profile on top of the studied domain compared

---

[3]See section 2.4.2.

[4]At the top of the domain, the mean theoretical flow tends to $\dfrac{3u_0^2 k}{4\sigma}$, see section 2.4.2.

59

Figure 4.4: Gentle case - Caen 1 - Comparison Model (-) / Experimental data (•) / Second order theory (- -). Horizontal velocity profiles for different wave phases. The corresponding wave phases are shown in the small graphs plotting the top horizontal velocity.

to the experimental and velocity. The modelled velocity is

$$u = u_s + u_{0c}\cos(\sigma t - kx) + u_{0s}\sin(\sigma t - kx) + u_{1c}\cos 2(\sigma t - kx) + \ldots$$

$$\ldots + u_{7c}\cos 8(\sigma t - kx) + u_{7s}\sin 8(\sigma t - kx)$$

where $u_{0c} = 0.287\ m.s^{-1}$ and $u_s = 0.0105\ m.s^{-1}$. Eight frequency components are needed in order to fit closely to the experimental velocity. The velocity profiles
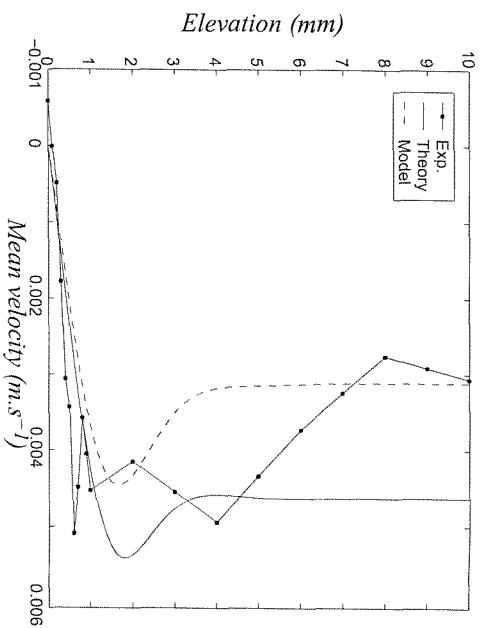
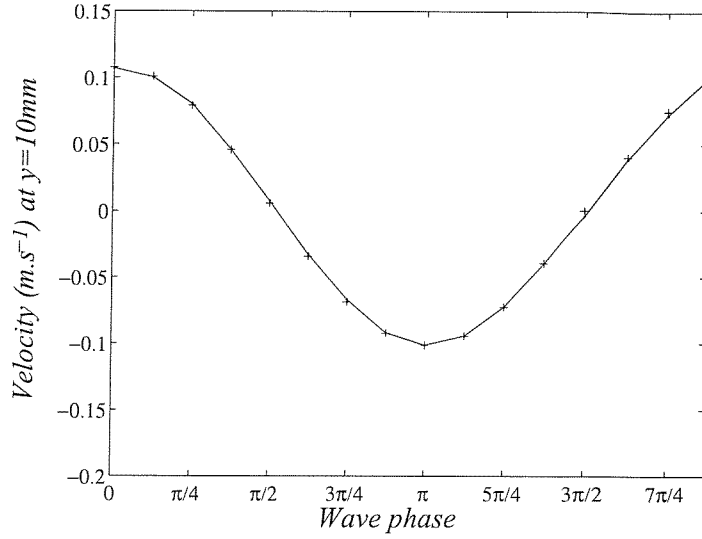Figure 4.5: Gentle case - Caen 1 - Mean Eulerian velocity. Comparison Model / Experimental data / Theory.
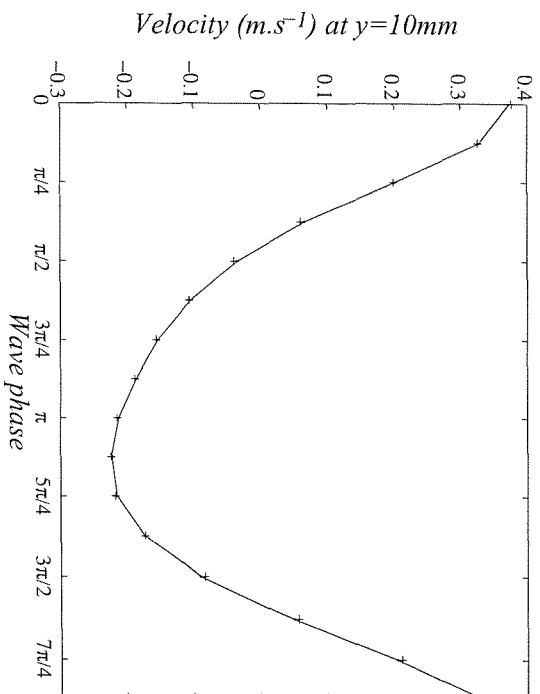
Figure 4.6: Steep wave case - Caen 4 - Horizontal velocity at the top of the domain. Comparison Model (+) / Experimental data (-) .

for different wave phases, from the bottom to an elevation of 10 *mm* are shown in figure 4.7. Agreement is generally good, but the overshoot velocity very close
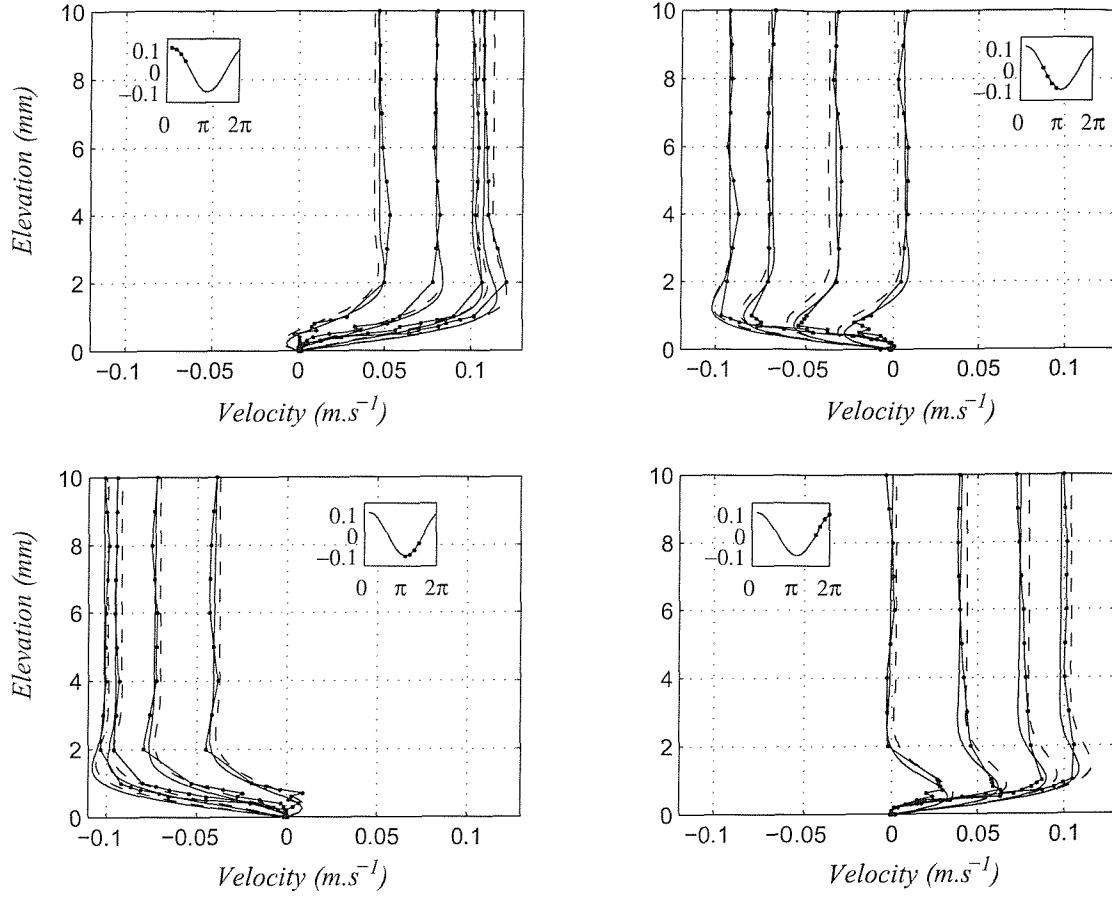

Figure 4.7: Steep wave case - Caen 4 - Comparison Model (-) / Experimental data (•) / Second order theory (- -). Horizontal velocity profiles for different wave phases. The corresponding wave phases are shown in the small graphs plotting the top horizontal velocity.

to the bottom predicted by the model can be different in magnitude from the experimental results. For a few wave phases, the velocity profiles calculated with the second order theory are significantly different from the experiments and the

model. This can be explained by the fact that in this case the actual flow has components at harmonics higher than the second. If the mean flow for a wave period is calculated (see figure 4.8), the profiles from the experiments and the model agree well at the top of the boundary layer, but as pointed out in the phase to phase comparison, the overshoot predicted by the model differs from the experimental results. The experimental measurements show that the theory overestimates the value of the mean flow on top of the domain, although the overshoot velocity predicted by the theory is close to the experimental value. From the Fourier analysis $u_s = 0.0105\ m.s^{-1}$, while the theory gives a steady drift equal to $0.03\ m.s^{-1}$, so nearly three times larger.
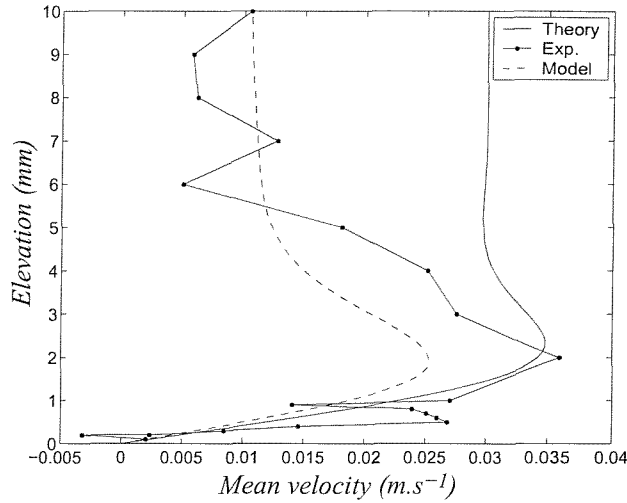
Figure 4.8: Steep wave case - Caen 4 - Mean Eulerian velocity. Comparison Model / Experimental data / Theory.

- **Rough bed and steep wave Case: Hanover 4**

    In this case the wave period is 5.0 s and the wavelength is 15.24 m. Figure 4.9 shows that the velocity profile on top of the studied domain can be modelled

by

$$u = u_s + u_{0c}\cos(\sigma t - kx) + u_{0s}\sin(\sigma t - kx)u_1 + u_{1c}\cos 2(\sigma t - kx) + ...$$

$$... + u_{7c}\cos 8(\sigma t - kx) + u_{7s}\sin 8(\sigma t - kx)$$

where $u_{0c} = 0.2655 m.s^{-1}$ and $u_s = -0.0152 m.s^{-1}$. Again, eight frequency components were used and agreement is generally good. The velocity profiles for
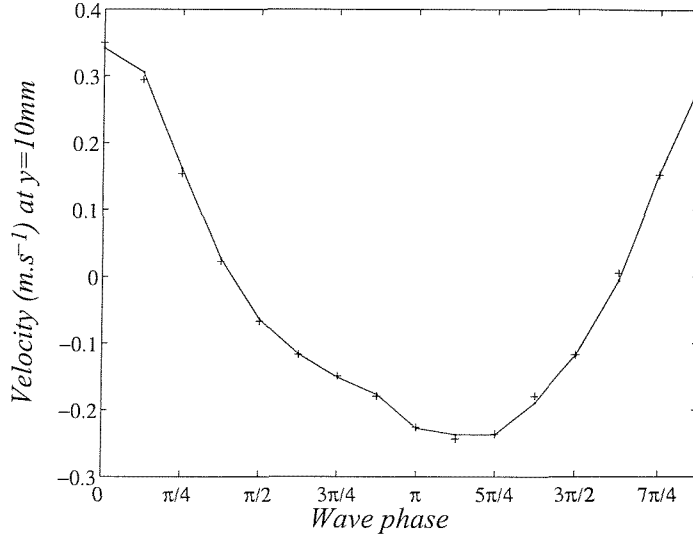
Figure 4.9: Rough case - Hanover 4 - Horizontal velocity at the top of the domain. Comparison Model (+) / Experimental data (-).

different wave phases, from the bottom to an elevation of 10 mm are shown in figure 4.10. Agreement between the model and the experiments is generally good but some significant discrepancies appear when compared to the second order theory for reasons given earlier. The mean Eulerian flow calculated from the model, the experiments and the theory are shown in figure 4.11. The experimental mean velocity and the modelled mean velocity are both negative on the top of the domain, as opposed to the positive mean flow predicted by the theory.
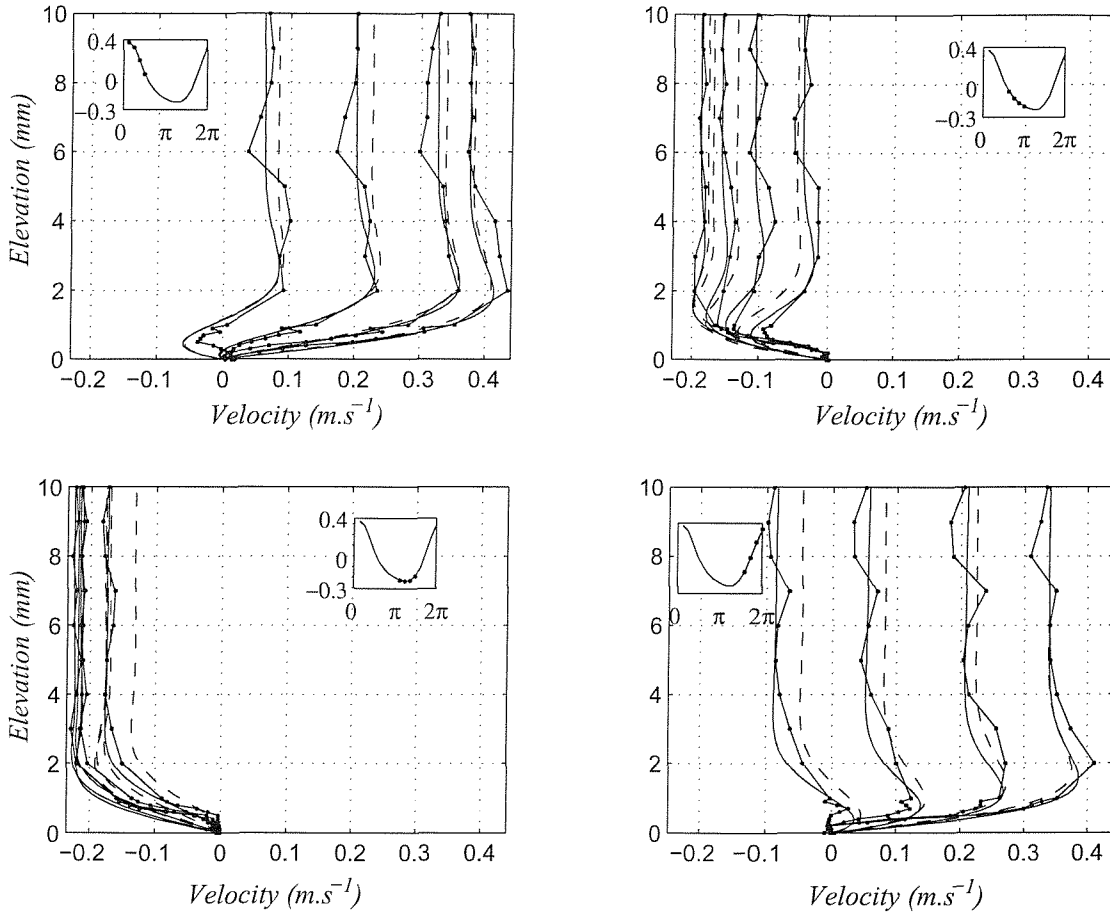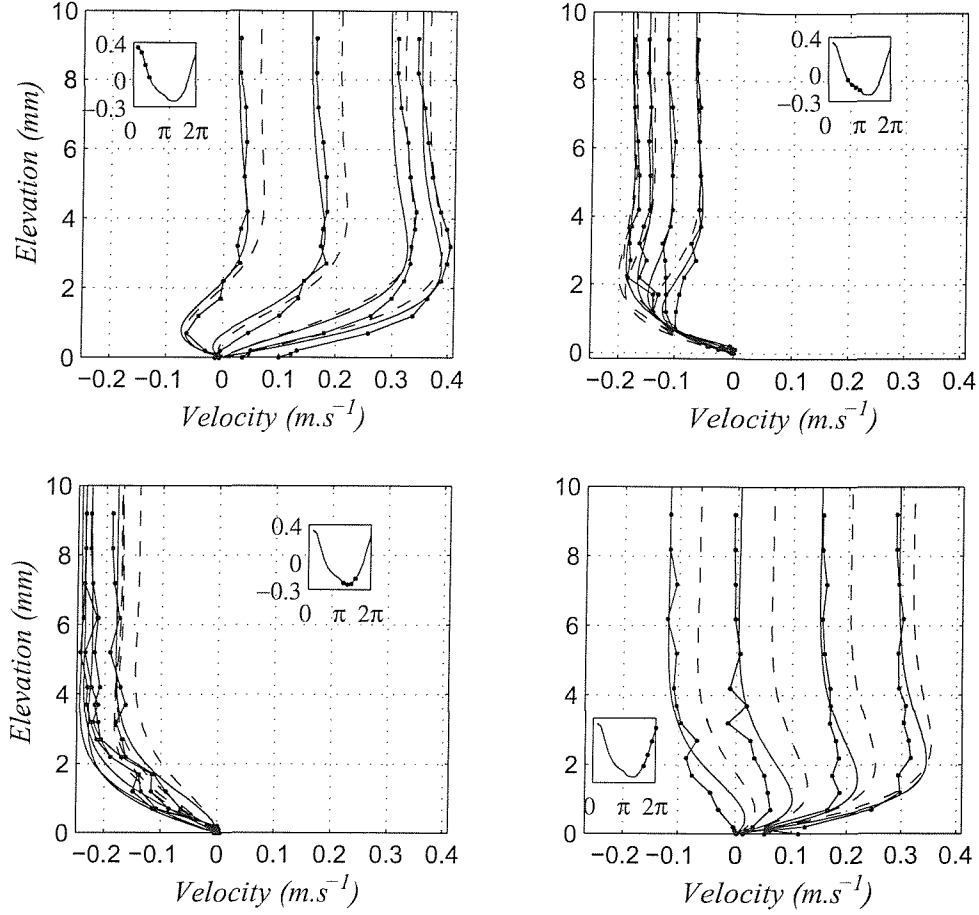
Figure 4.10: Rough case - Hanover 4 - Comparison Model (-) / Experimental data (•) / Second order theory (- -). Horizontal velocity profiles for different wave phases. The corresponding wave phases are shown in the small graphs plotting the top horizontal velocity.

The mean experimental velocity at $y = 10\ mm$ is $u_s = -0.0152\ m.s^{-1}$ while the theory predicts $u_s = 0.0173\ m.s^{-1}$.
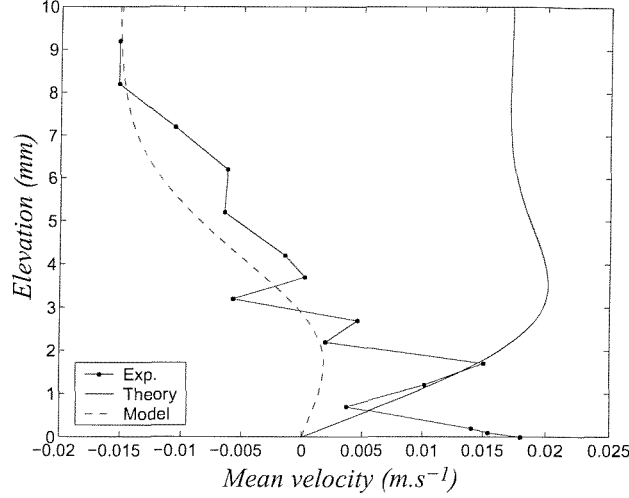
*Figure 4.11: Rough case - Hanover 4 - Mean Eulerian velocity. Comparison Model /
Experimental data / Theory.*

4.2.3   Mean Eulerian drift: model, experiment and theory

Comparison theory - model

In section 4.2.2, when the model is compared to the experimental data, the mean
experimental velocity value at the top of the domain is used in the velocity definition
imposed on top of the numerical domain. Similarly if the top mean velocity predicted
by the theory is used in the model as u_s, the constant component of the velocity
imposed in the computed domain, the model gives a mean velocity profile identical to
the theoretical mean profile. When a loop minimizing the top mean vorticity is used in
the model[5], results from the model are not strictly identical but are very close to the
theory. Figure 4.12 shows the comparison for the case Hanover 4. The model profile is
not strictly superposed on the theoretical curve as it would be the case if the theoretical
steady component of the velocity u_s were imposed as the steady part of the velocity

---

[5]See section 3.3.3.

66

definition in the model. However, the difference is very small when compared to u_0, as

$$\frac{U_{max}^{theo} - U_{max}^{model}}{u_0}$$

is of order 10^{-3} where U_{max}^{theo} and U_{max}^{model} are the maximum velocity amplitudes from the theory and the model respectively. It means that the difference is negligible in terms of the magnitude of the instantaneous velocity profiles. If only the Eulerian velocity is considered, the difference is still acceptable as

$$\frac{U_{max}^{theo} - U_{max}^{model}}{U_{max}^{theo}} = 0.055$$

which means that there is a maximum error of 5.5% between the two mean profiles. However, a more important issue is that, as shown in figure 4.12, agreement between the
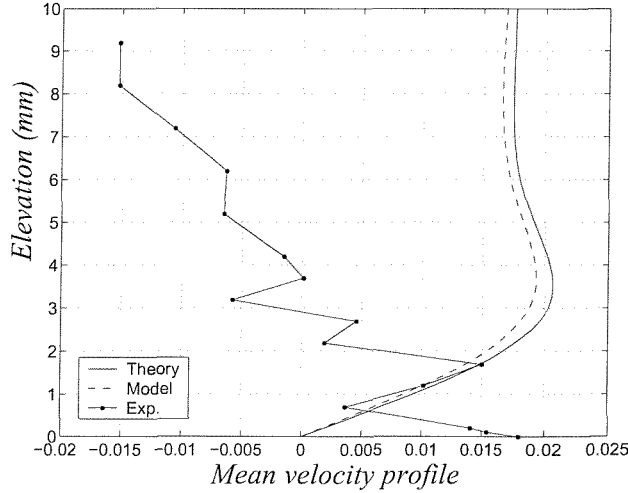

Figure 4.12: Hanover 4 - Mean Eulerian velocity - Comparison Experimental data / Theory / Model with vorticity minimized at the top of the computed domain.

experimental and the theoretical mean velocity is not good; the experimental conditions might not respect the theoretical assumptions such as a vanishing vorticity at the top of the boundary layer.

Comparison experiments - model with imposed vorticity

When the instantaneous velocity profiles from the experiments and the second order theory[6] are compared, acceptable agreement is reached (figures 4.4, 4.7 and 4.10). All the instantaneous velocity profiles from the Hanover and Caen cases have been compared to the second order theory in Mouazé et al. (2002), and good agreement was reached. However, as previously shown, there is usually a significant difference between the experimental data and the Longuet-Higgins theoretical solution for the mean Eulerian velocity value at the top of the domain. As explained in section 3.3.3, the theory assumes a zero vorticity at the top of the boundary layer, giving a vertical velocity profile. When the mean Eulerian velocity is calculated, several experimental cases feature a slope at the top of the measured domain. This might be explained by the presence of a significant mean vorticity in this area. In order to study this possibility, the top boundary condition (3.21) has been modified. Instead of minimizing the vorticity by trying different values of u_s, a mean vorticity is imposed at the top of the computed domain. This mean vorticity is calculated from the experimental data, and u_s is deduced from the predicted slope obtained with the corresponding vorticity. It is assumed that imposing such a vorticity could induce a slope in the computed mean Eulerian velocity profile similar to the experimental one. Unfortunately, the results obtained with an imposed vorticity are not convincing so far. An example is shown in figure 4.13, where the slopes from the modelled and experimental profiles are close and the overshoot amplitudes are of same order. However in order to reach such a agreement, in this case, the steady component of the velocity u_s has to be very different from the experimental one. Further investigations need to be done on this subject. When the present numerical model is compared to the experimental data, the mean Eulerian velocity can either have a slope close to the experimental one but with a steady component u_s usually very different from the top value of the mean experimental velocity or it can feature a steady component close to the top value of

---

[6]See section 2.4.2 and Sleath (1972).

the mean experimental velocity but will not present a similar slope.
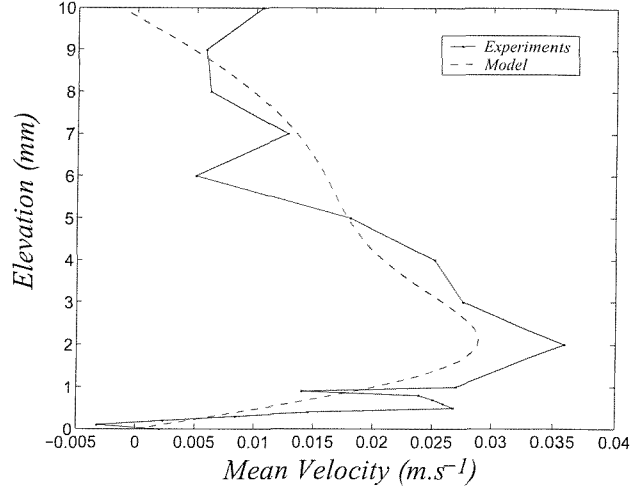
Figure 4.13: Caen 4 - Mean Eulerian velocity - Comparison Experimental data / Model with imposed vorticity at the top of the domain.

4.2.4 Discussion

1. Concerning the comparisons of the **instantaneous velocities**, the model showed good agreement with the experimental data for the prediction of the wave-induced oscillatory flow for weak conditions (small wave height, small wavelength). In strong flow conditions, differences appear on a phase to phase comparison despite a general behaviour quite similar for a wave period. This problem might be explained by the following factors:

   - The roughness of the floor in the Hanover flume is 0.8 *mm*, but as no element of roughness has been included in the boundary conditions of the model, discrepancies have to be expected.

   - The presence of turbulence, especially in the Hanover flume can also induce discrepancies.

2. Concerning the **mean Eulerian velocity**:

- Comparisons between the experimental and the modelled mean velocity profiles highlight the problem of the velocity definition in the model. The velocity definition appears to be a key boundary condition, and the combination of a steady component with a series of sines and cosines can be difficult to set properly when compared to experimental data.

- Discrepancies between the experimental and the theoretical mean Eulerian profiles might be explained by a weak but significant vorticity existing outside the considered domain in the experimental case when the theory assumes a vorticity vanishing at the top of the boundary layer. In none of the studied cases did the top value of the mean experimental velocity agree with the theoretical top velocity. This might also be explained by the fact that the vorticity influencing the flow is the vorticity convected from the upstream and downstream of the domain, taking over the weak vorticity generated in the bottom boundary layer. It appears that the boundary layer solution from Longuet-Higgins (section 2.4.2) may not be adapted for the present cases.

- The discrepancies previously discussed could also be explained by the presence of a counter flow in the wave flume, induced by the Stokes drift. This counter flow localized outside the boundary layer could induce a non-vanishing vorticity at the top of the measured domain. Progressive wave trains travelling along the flume independently from the incident waves and disturbances caused by the wave paddle can also be sources of discrepancies but are difficult to quantify.

4.3   Rippled bed case

4.3.1   Introduction

In this section, the model output is compared to another numerical model (Blondeaux and Vittori, 1991), and experimental data (Marin, 1992). For both cases, the present model is run using all relevant parameters being as close as possible to the values used in the previously mentioned studies. These parameters are the ripple characteristics (height and wavelength), the wave period and the maximum amplitude of the wave-induced velocity. Then, in section 4.3.4, a series of runs is done for different flow conditions, in order to study the recirculation cells mentioned in section 2.5.2. Finally, in section 4.3.5, the mean Eulerian flow calculated by the model is studied at different locations along the ripple.

4.3.2   Comparison with Blondeaux and Vittori's numerical model

This comparison uses the work from Blondeaux and Vittori (1991) that was aimed at studying the vorticity dynamics over a rippled bed in oscillatory flows. The comparisons presented here are mainly qualitative, as the plotted results used are just taken from the figures available in their article.

First case

The first comparison is made for $R_\delta = 50$. The amplitude of fluid displacement over the ripple wavelength ratio is equal to $r = 0.75$ and the ripple slope is $s_r = 0.15$. Figure 4.14 shows the vorticity development for different wave phases as computed by the present model and can be compared to figure 4.15 showing the results from Blondeaux and Vittori (1991) for the same case. In the same way, figure 4.16 shows the stream function evolution as computed by the model and can be compared to the results from Blondeaux and Vittori (1991) shown in figure 4.17. Figure 4.18 shows the model results for the vorticity contours after several wave periods and is compared to

figure 4.19 from Blondeaux and Vittori (1991).

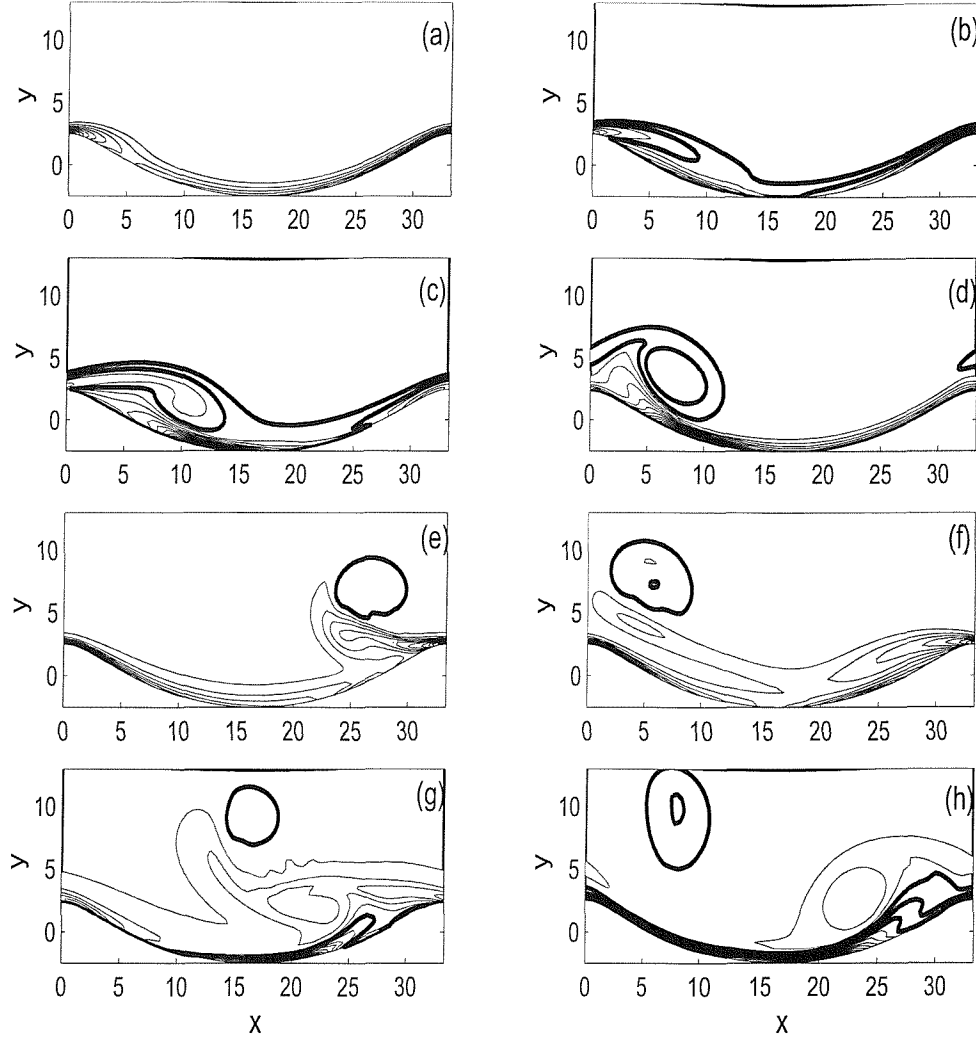*Figure 4.14: Vorticity contours; numerical model - first case; $\Delta\omega=0.15$; (—) clockwise vorticity; (-) counterclockwise vorticity - $R_\delta = 50$; $r = 0.75$; $s_r = 0.15$; (a) $t = \pi/4$; (b) $t = \pi/2$; (c) $t = 3\pi/4$; (d) $t = \pi$; (e) $t = 5\pi/4$; (f) $t = 3\pi/2$; (g) $t = 7\pi/4$; (h) $t = 2\pi$. $x=x'/\delta^\star$; $y=y'/\delta^\star$.*

Good agreement is generally reached in these comparisons, with a very close matching of the vortices development with respect to the wave phase. However, in figure 4.19 (Blondeaux and Vittori), after 5 wave periods, secondary vortex structures seem to last longer while they have already vanished in figure 4.18 (present results).

Second case

For this case, R_δ is equal to 100, while r and s_r remain unchanged. Vorticity contours at different wave phases as computed by the present model are shown in figure 4.20 and can be compared to the results from Blondeaux and Vittori (1991) shown in figure 4.21. For such a large R_δ, the comparison reaches a good agreement for the timing of the vortex generation. Nevertheless, the present results show vortices vanishing or getting washed over the disturbed layer quicker than for the results from Blondeaux and Vittori (1991).

Discussion

For both cases, the comparisons between the results from the model described in chapter 3 and those from Blondeaux and Vittori (1991) reach a good agreement. Both models show a vortex generation for each half wave cycle, but the vortices' lifetime seems to be longer for Blondeaux and Vittori's model. These comparisons stay however qualitative. In the next section, as a step further in the validation of the computer model, a set of experimental data are compared to the model output.

Figure 4.15: Vorticity contours; Blondeaux and Vittori (1991) results (figure 6, p273) - first case; $\Delta\omega$=0.15; (—) clockwise vorticity; (–) counterclockwise vorticity - $R_\delta = 50$; $r = 0.75$; $s_r = 0.15$; (a) $t = \pi/4$; (b) $t = \pi/2$; (c) $t = 3\pi/4$; (d) $t = \pi$; (e) $t = 5\pi/4$; (f) $t = 3\pi/2$; (g) $t = 7\pi/4$; (h) $t = 2\pi$.

74
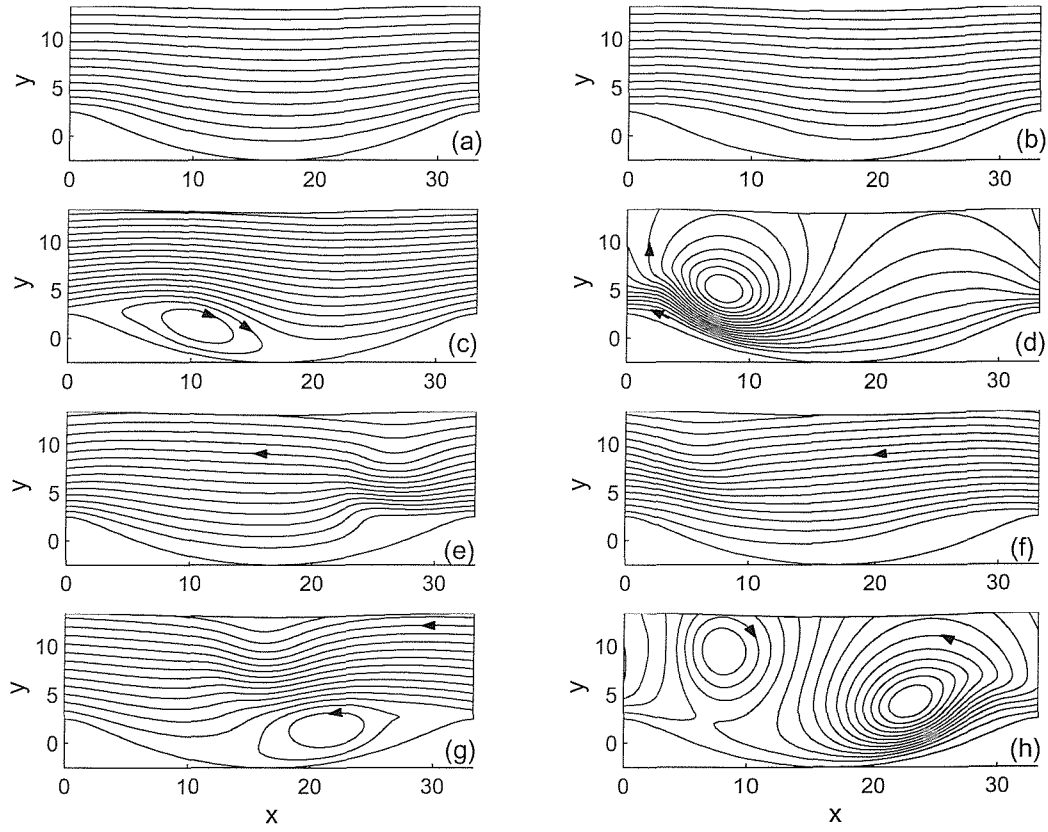
Figure 4.16: Streamline time development; numerical model - first case; $R_\delta = 50$; $r = 0.75$; $s_r = 0.15$; (a) $t = \pi/4$; (b) $t = \pi/2$; (c) $t = 3\pi/4$; (d) $t = \pi$; (e) $t = 5\pi/4$; (f) $t = 3\pi/2$; (g) $t = 7\pi/4$; (h) $t = 2\pi$. $x = x'/\delta^\star$; $y = y'/\delta^\star$.
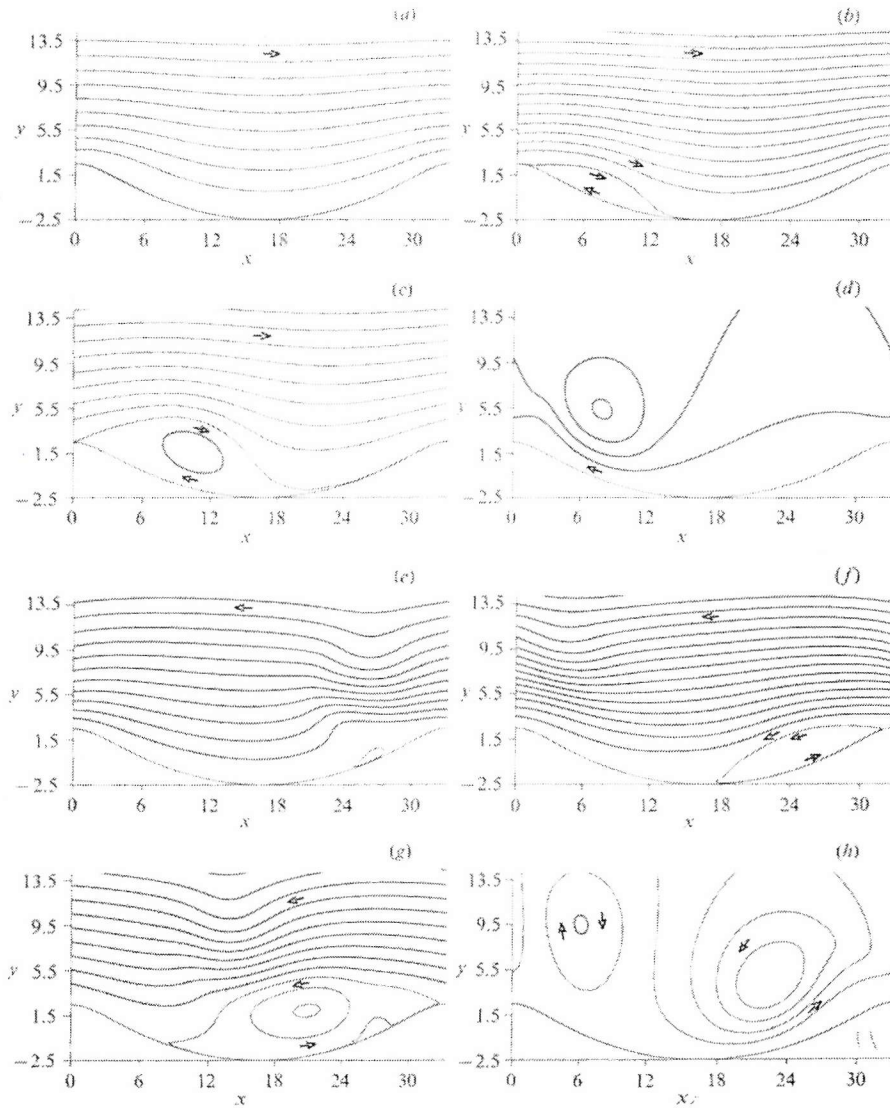
Figure 4.17: Streamline time development; Blondeaux and Vittori (1991) results (figure 8, p276) - first case; $R_\delta = 50$; $r = 0.75$; $s_r = 0.15$; (a) $t = \pi/4$; (b) $t = \pi/2$; (c) $t = 3\pi/4$; (d) $t = \pi$; (e) $t = 5\pi/4$; (f) $t = 3\pi/2$; (g) $t = 7\pi/4$; (h) $t = 2\pi$.
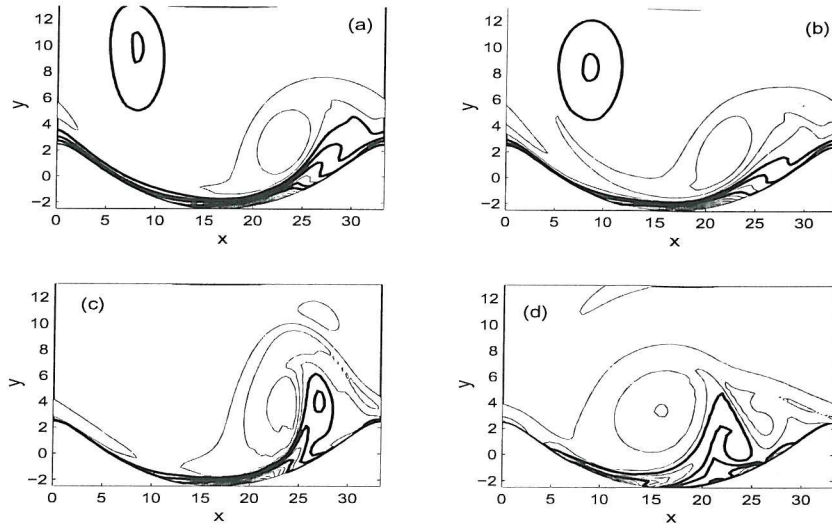
Figure 4.18: Vorticity contours; numerical model - first case; $\Delta\omega=0.15$; ($\longrightarrow$) clockwise vorticity; ($-$) counterclockwise vorticity - $R_\delta = 50$; $r = 0.75$; $s_r = 0.15$; (a) $t = 2\pi$; (b) $t = 4\pi$; (c) $t = 6\pi$; (d) $t = 10\pi$. $x=x'/\delta^\star$; $y=y'/\delta^\star$.

Figure 4.19: Vorticity contours; Blondeaux and Vittori (1991) results (figure 18, p283) - first case; $\Delta\omega=0.15$; ($\longrightarrow$) clockwise vorticity; ($-$) counterclockwise vorticity - $R_\delta = 50$; $r = 0.75$; $s_r = 0.15$; (a) $t = 2\pi$; (b) $t = 4\pi$; (c) $t = 6\pi$; (d) $t = 10\pi$.

Figure 4.20: Vorticity contours; numerical model - second case; $\Delta\omega=0.15$; (—) clockwise vorticity; (–) counterclockwise vorticity - $R_\delta = 100$; $r = 0.75$; $s_r = 0.15$; (a) $t = \pi/2$; (b) $t = \pi$; (c) $t = 3\pi/2$; (d) $t = 2\pi$. $x=x'/\delta^\star$; $y=y'/\delta^\star$.
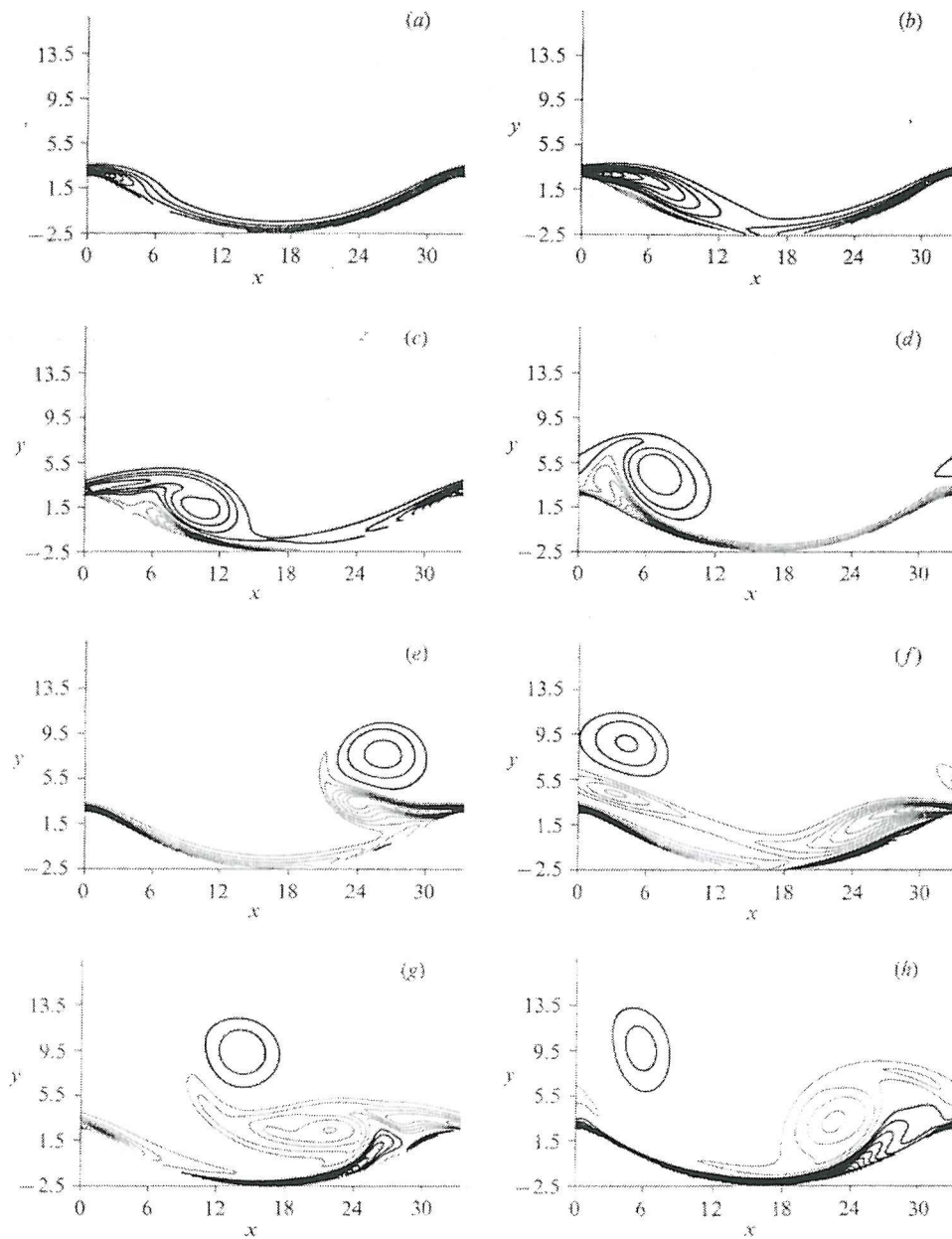

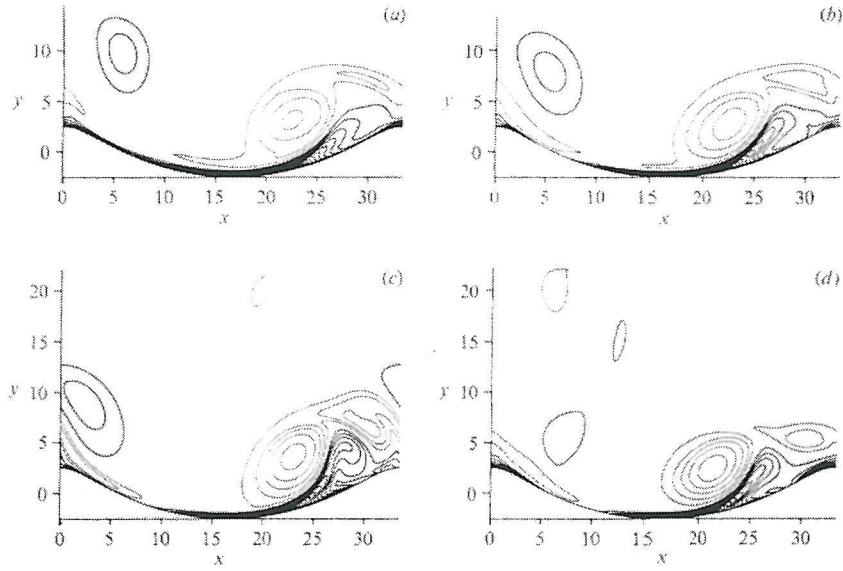*Figure 4.21: Vorticity contours; Blondeaux and Vittori (1991) results (figure 7, p275) - second case; $\Delta\omega=0.15$; (—) clockwise vorticity; (–) counterclockwise vorticity - $R_\delta = 100$; $r = 0.75$; $s_r = 0.15$; (a) $t = \pi/2$; (b) $t = \pi$; (c) $t = 3\pi/2$; (d) $t = 2\pi$.*
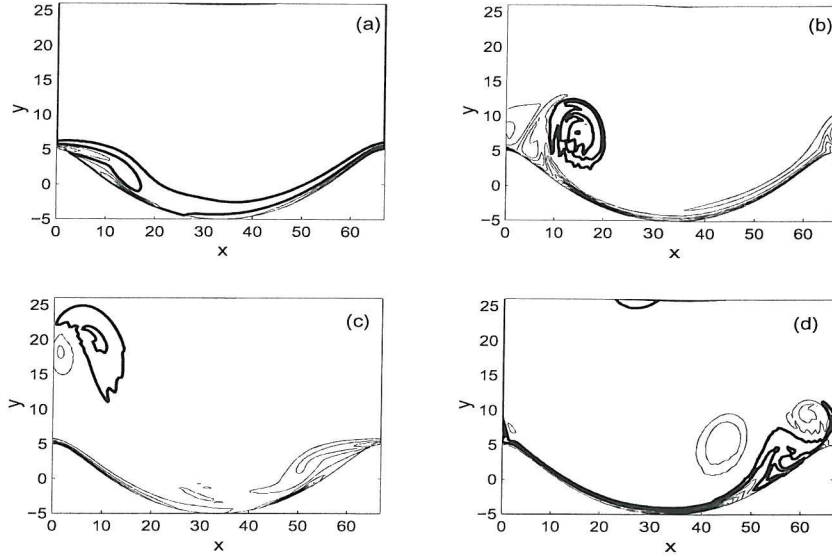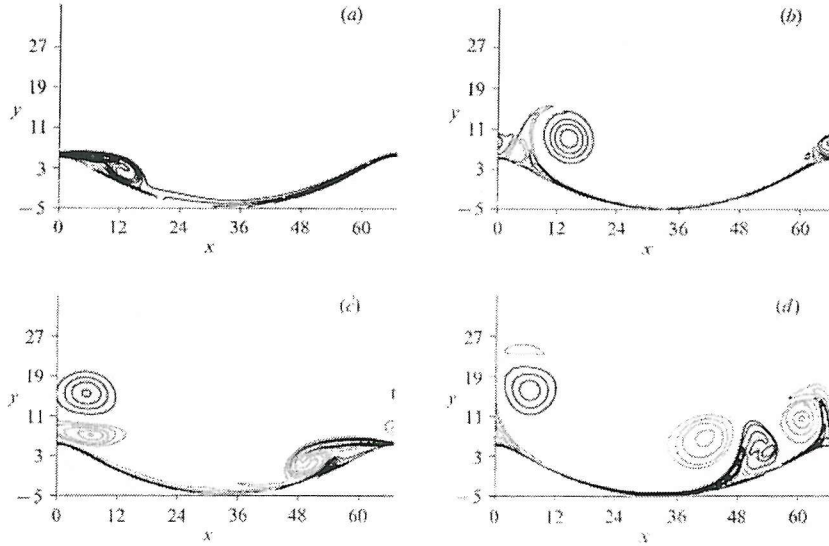
4.3.3 Comparison with Marin's experimental results

This comparison uses the experimental data from Marin (1992), kindly provided for this purpose. The experiments consisted in using Laser Doppler Velocimetry to study the vorticity dynamics in the vicinity of a rippled bed subjected to water waves. The rippled bottom was cut out from an aluminium plate. Formulas (2.33) and (2.34) were used to model the surface. The rippled section was 1 m long placed at the bottom of a 9 m long wave flume. The velocity field has been mapped over a ripple wavelength, for different wave phases. The Reynolds number R_δ was equal to 58, with a wave period of 1.08 s, a wavelength of 1.46 m, while the ripple height was equal to 3 mm and the ripple wavelength to 18 mm, giving a ripple slope $s_r = 0.17$. The flow and ripple characteristics were close to the first case studied by Blondeaux and Vittori (1991).

Velocity fields

The figures 4.22 to 4.27 are comparisons of the model output with Marin's experimental data, representing the velocity field over the entire domain at a certain wave phase. The vortex evolution can be seen, from the beginning of the second half of the wave period (figure 4.22) to the end of the wave period (figure 4.27). The represented domain height is 10 mm above the ripple crest.

Mean velocity profiles

The mean velocity profiles at the ripple crest, at mid-distance between the crest and the trough in the ripple slope and at the ripple trough are calculated from the model and compared to Marin's experimental data in figure 4.28. Agreement is acceptable for the different locations except for the profile above the trough where the model predicts a positive profile very close to the bed while the experimental mean velocity is negative. This type of discrepancy could not be noticed in the comparisons of the instantaneous velocity fields as the velocities involved are much larger. In the intermediate location, the experimental overshoot amplitude takes place in a layer thicker than the model prediction, but the modelled profile follows a curve similar to the experimental one.
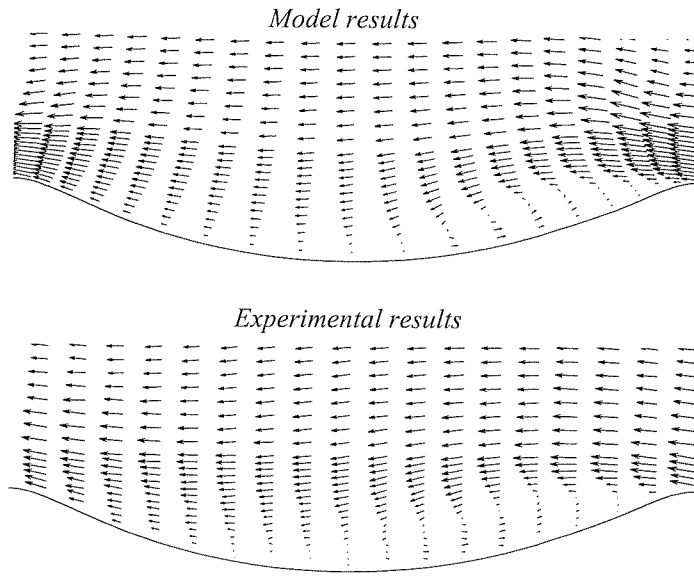
Figure 4.22: Velocity field over one ripple. Wave phase $\sigma t = 3.1416$. Maximum velocity: $0.16 \ m.s^{-1}$.

Model results

Experimental results
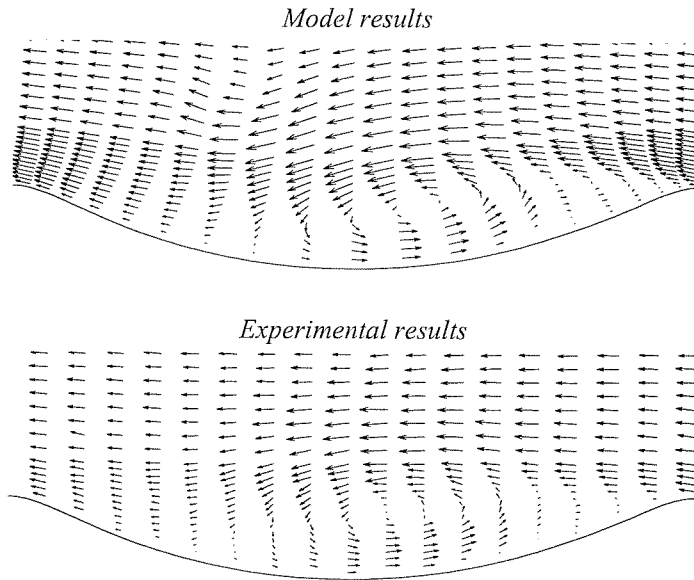
Figure 4.23: Velocity field over one ripple. Wave phase $\sigma t = 3.77$. Maximum velocity: $0.11 \ m.s^{-1}$.

Model results

Experimental results
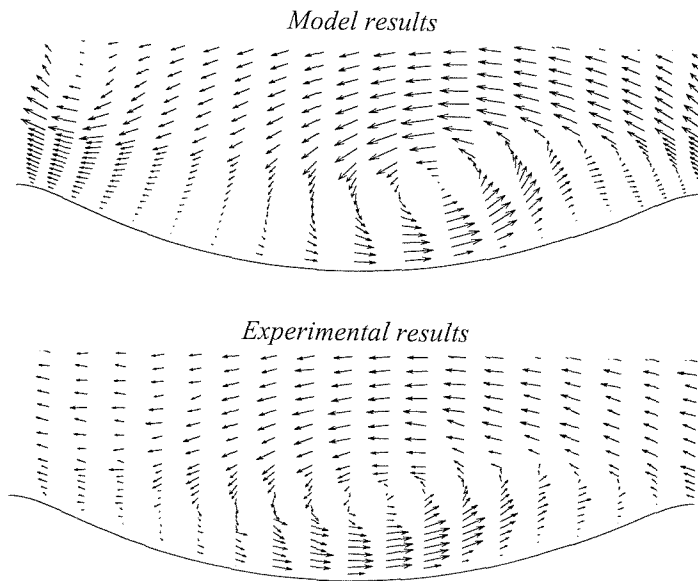
Figure 4.24: Velocity field over one ripple. Wave phase $\sigma t = 4.2726$. Maximum velocity: 0.11 m.s^{-1}.

Model results

Experimental results
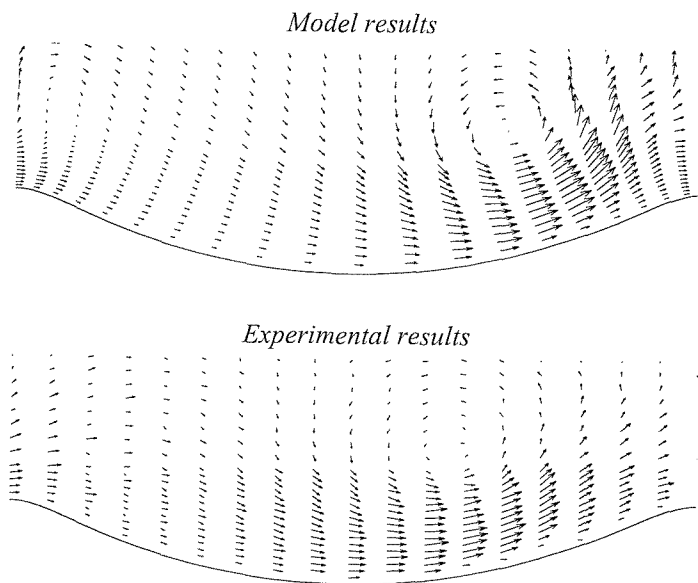
Figure 4.25: Velocity field over one ripple. Wave phase $\sigma t = 4.7752$. Maximum velocity: 0.10 m.s^{-1}.

Model results

Experimental results
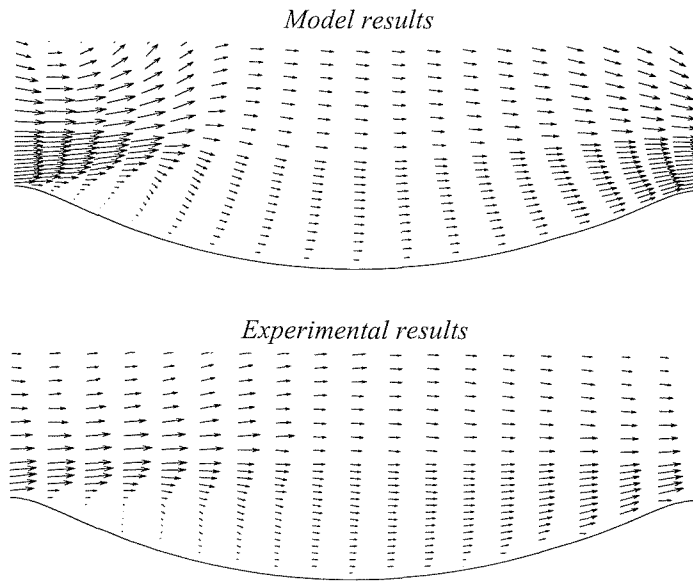
Figure 4.26: Velocity field over one ripple. Wave phase $\sigma t = 5.4035$. Maximum velocity: $0.17\, m.s^{-1}$.

*Model results*

Experimental results
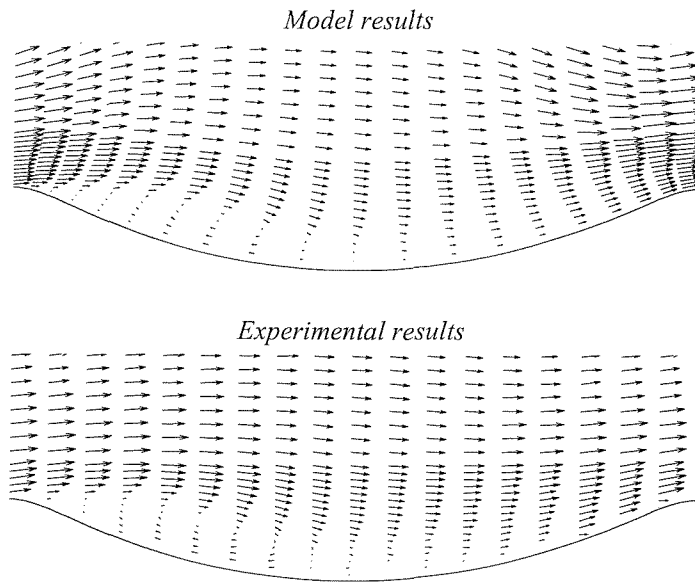
Figure 4.27: Velocity field over one ripple. Wave phase $\sigma t = 6.1575$. Maximum velocity: $0.20\, m.s^{-1}$.
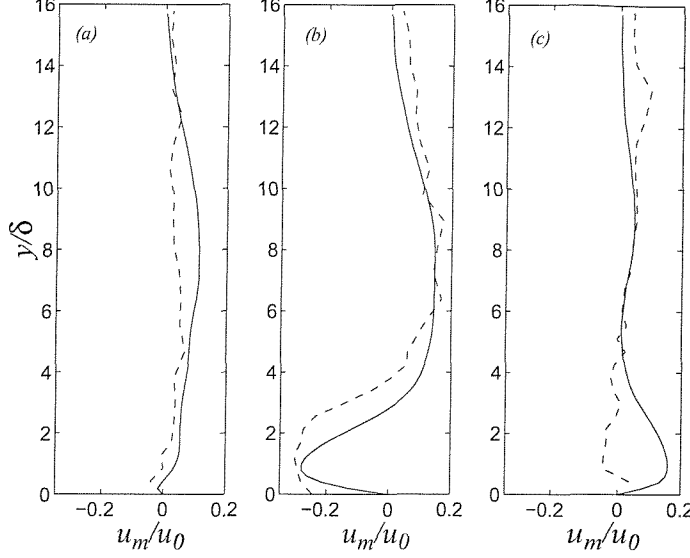
Figure 4.28: Mean velocity profiles u_m/u_0; (a) above the ripple crest; (b) at mid-distance between the crest and the trough; (c) above the trough. (- -) experiments, (-) model; Marin's experimental conditions: $s_r = 0.17$; $r = 0.95$; $T = 1.08$ s.

Discussion

- It is worth noting that the matching of the data in their exact location is approximate as it was not possible to define a grid for the model strictly similar to the measurement grid used for the experiments.

- The major differences take place on the bottom of the domain. The experimental velocities close to the bed are usually smaller than the modelled velocities. The layer of strong acceleration in the flow is usually thicker for the model than for the experiments. This layer is also mainly located above the ripple crests for the model, but it can be stretched along the entire ripple length for the experiments. This difference might be partly explained by the fact that the model does not consider any bed roughness, while in the experimental case, even though being weak, a bed roughness exists.

- A simple cosine shape for the imposed velocity seems to match correctly the experimental velocity at the top of the studied domain. The shallow water approximation (section 3.3.3) appears to be accurate enough to model the wave-induced velocity in these conditions.

- When the mean velocities from the model and the experiments are compared, good agreement is not always reached, especially above the ripple trough. These discrepancies are negligible when the instantaneous velocities are considered.

4.3.4   Steady streaming circulation cells

As pointed out in section 2.5.2, for a weak flow oscillation amplitude compared to the ripple wavelength, and usually for a gentle ripple slope, steady streaming cells tend to appear. These cells are regions of closed streamlines for the mean flow[7]. The model has been tested for a medium ripple slope[8] $s_r = 0.1$ and for a very weak orbital amplitude to ripple wavelength ratio $r = 0.18$. Streamlines of the computed mean flow for a wave period are shown in figure 4.29. The double structure of circulation cells is shown. This test uses the same physical parameters (r, s_r, T) as the experimental test shown in section 6.2.1, figure 6.5. Figure 4.30 shows the streamlines for conditions similar to the previous case except for the orbital amplitude to ripple wavelength ratio, increased to $r = 0.33$. According to Honji et al. (1980), if r is significantly increased, only the upper pair of cells should be left. But from figure 4.30, it seems that only the lower cells are present. The large upper pair might still exist but outside the computed domain. This case does not agree with Honji et al. (1980) as the lower pair of cells does not seem to have changed for a value of r nearly doubled from the case shown in figure 4.29 where the double pair is visible.

---

[7] See section 2.5.2

[8] Corresponding to the medium slope used in the present experimental study. See table 5.1 in chapter 5 (experimental arrangements).
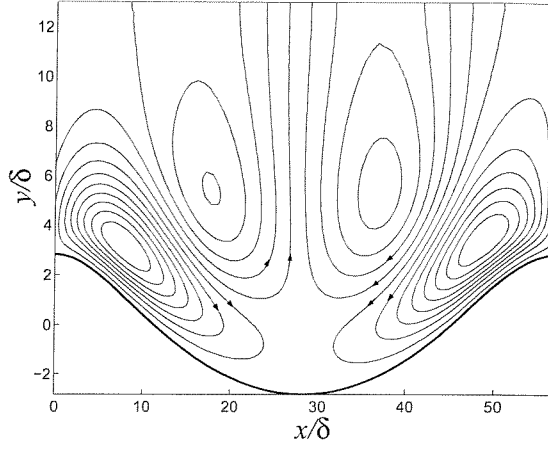
Figure 4.29: Steady streaming circulation cells; ripple slope $s_r = 0.1$; $r = 0.18$; wave period $T = 1.43$ s; $\delta/l_r = 0.0176$.
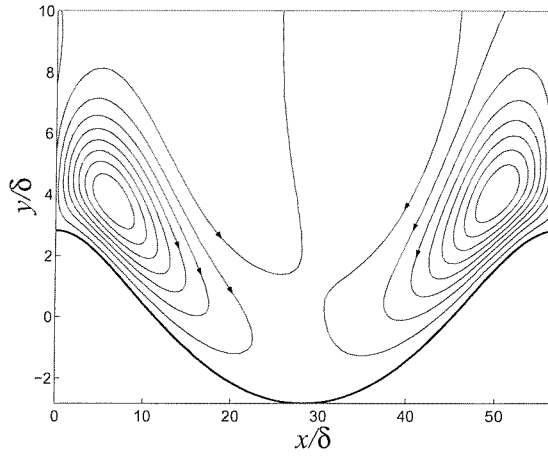
Figure 4.30: Steady streaming circulation cells; ripple slope $s_r = 0.1$; $r = 0.33$; wave period $T = 1.43$ s; $\delta/l_r = 0.0176$.

Another test is run for a weak ripple slope[9] $s_r = 0.05$, a very weak $r = 0.09$ and a wave period $T = 1$ s. Streamlines of the mean computed flow for a wave period are

---

[9]Corresponding to the weakest slope used in the present experimental study, see table 5.1.

shown in figure 4.31. The upper pair of circulation cells is so large that only the lower part of the cells can be seen. The lower pair of cells is present, but their disturbed shape might indicate that even for such a weak r, the upper cells begin to make their way to the rippled boundary pushing away the lower pair of cells. The model has also been run for the same ripple slope, the same wave period but for an increased $r = 0.31$. Streamlines of the mean computed flow for a wave period are shown in figure 4.32. This test uses physical parameters similar to the experimental conditions of the flow visualization shown in section 6.2.1, figure 6.6. For this case, r is larger than for the previous case ($r = 0.31$ instead of $r = 0.09$) and only one pair of circulation cells appears. In these conditions, according to Honji et al. (1980), the lower vortex layer is usually so small that only the upper layer can be seen. However, in figure 4.32, the circulation direction indicates that the only pair of circulation cells left is the lower pair. This case would then give better agreement to the results from Sleath (1976) shown in section 2.5.2, figure 2.10 (a).
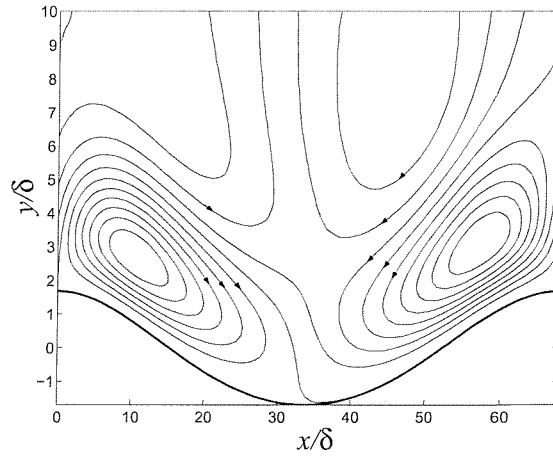
Figure 4.31: Steady streaming circulation cells; ripple slope $s_r = 0.05$; $r = 0.09$; wave period $T = 1$ s; $\delta/l_r = 0.0148$.

The presented numerical results agree well with the analysis mentioned in section 2.5.2, for the description of streamlines circulation cells over a very weak slope and for

86
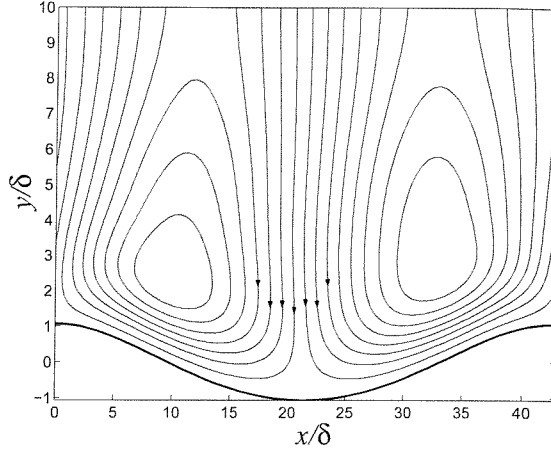
Figure 4.32: Steady streaming circulation cells; ripple slope $s_r = 0.05$; $r = 0.31$; wave period $T = 2.5$ s; $\delta/l_r = 0.0234$.

a weak flow oscillation, but as soon as the ripple slope becomes more significant, the structures seem to behave differently. In the present investigation, the cases studied are mainly for slopes of significant steepness, closer to real ripple slopes. The effects of these structures on the mean and instantaneous flow need further investigation, especially for cases of significant ripple slopes. Such studies are beyond the scope of the present work.

4.3.5 Mean velocity drift

A series of mean profiles was computed for a ripple slope $s_r = 0.175$ corresponding to the steepest slope used in the present experimental study[10], and for a wave period $T = 2$ s. Figures 4.33 and 4.34 show the mean velocity profiles for $r = 0.31$ and $r = 0.52$ respectively. The general tendency for an increase in r is an increase in the overshoot amplitude[11] of the profiles and the layer where the overshoot is located also becomes

---

[10]See table 5.1, in chapter 5 (experimental arrangements).

[11]In the present cases, the overshoot amplitude is the maximum amplitude located close to the bottom that exceeds the amplitude at the top of the studied domain.

thicker. In these two examples, the velocity overshoot is negative above the crest and at mid-slope, but can be either positive or negative in the trough. The profiles at mid-slope and above the trough are close to Marin's experimental mean profiles (figure 4.28), despite not being for the same flow conditions but for a ripple slope of same order.

Figure 4.33: Mean velocity profiles u_m/u_0; (a) above the ripple crest; (b) at mid-distance between the crest and the trough; (c) above the trough; $s_r = 0.175$; $r = 0.31$; $T = 2$ s.

Two other tests with wave conditions close to these cases were also run. The wave period is still $T = 2$ s, but the ripple slope is decreased to $s_r = 0.05$. Figures 4.35 and 4.36 show the mean velocity profiles for $r = 0.4$ and $r = 0.54$ respectively. Both profiles at the crest and at mid-slope feature a negative overshoot, similarly to the profiles in figures 4.33 and 4.34. The profile at the trough features a very weak negative overshoot. Regardless to the sign of the profiles, a tendency similar to figures 4.33 and 4.34 shows an increase of the overshoot amplitudes when r is increased.

It appears that in all the numerical tests presented, the mean velocity profiles above the ripple crest and at mid-slope always featured a negative overshoot. The
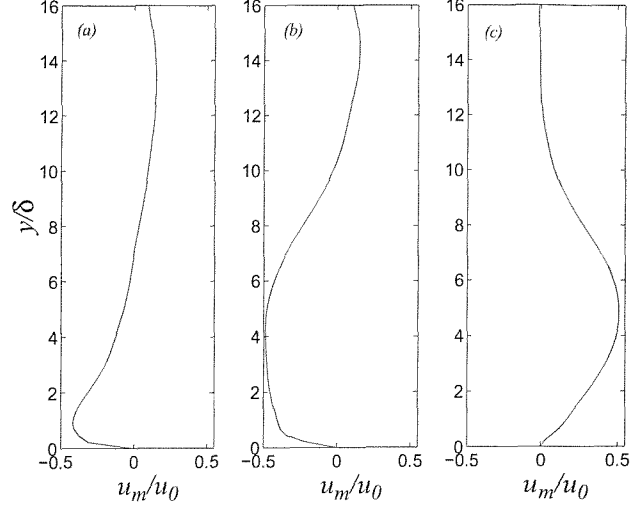
Figure 4.34: Mean velocity profiles u_m/u_0; (a) above the ripple crest; (b) at mid-distance between the crest and the trough; (c) above the trough; $s_r = 0.175$; $r = 0.52$; $T = 2$ s.

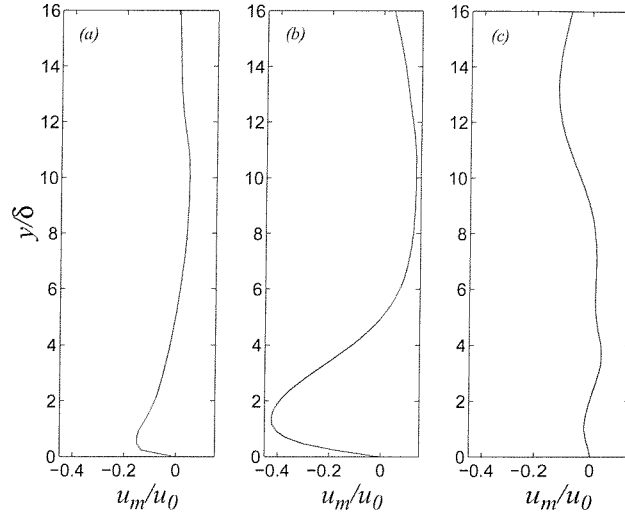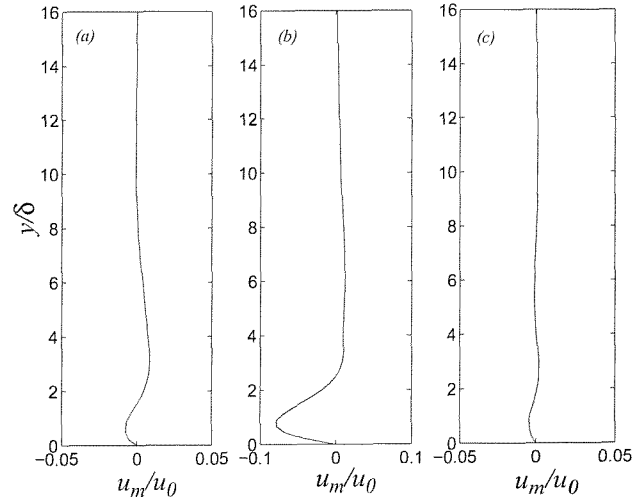*Figure 4.35: Mean velocity profiles u_m/u_0; (a) above the ripple crest; (b) at mid-distance between the crest and the trough; (c) above the trough; $s_r = 0.05$; $r = 0.4$; $T = 2$ s.*
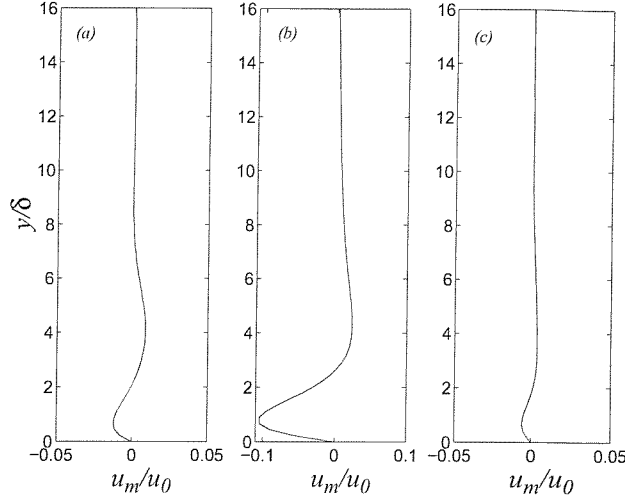
Figure 4.36: Mean velocity profiles u_m/u_0; (a) above the ripple crest; (b) at mid-distance between the crest and the trough; (c) above the trough; $s_r = 0.05$; $r = 0.54$; $T = 2$ s.

mean velocity profiles above the trough featured both negative and positive overshoots for different flow and ripple conditions.

4.4 Discussion on the model results and comparisons

The computer model results have been compared to data from three different sources: experimental results for a flat bed case (Mouazé, 2001), numerical results for a rippled bed case (Vittori and Blondeaux, 1991) and eventually experimental results for a rippled bed case (Marin, 1992). In all comparisons, agreement was quite good. In the case of a flat bed, some comparisons raised the problem of the choice of an accurate wave-induced velocity definition to reproduce the experimental flow at the top of the studied domain. The validity of the theoretical solutions for the mean boundary layer flow and the mass transport velocity has been questioned. Discrepancies between the experimental data and the theory might be explained by an inappropriate choice of

theoretical solution. The assumptions made to obtain the theoretical boundary layer solution appear to be incorrect when compared to the experimental data from Mouazé (2001).

On the other hand, concerning the velocity definition, comparisons with the experimental study from Marin (1992) for a rippled bed showed that a simple definition for the wave-induced velocity in shallow water such as $u = u_0 \cos(\sigma t)$ could reproduce the flow at the top of the domain[12]. It has also been shown that the computer model can predict vortex formation in a very similar way to its real occurrence. However, the lifetime and behaviour of the vortices can slightly differ from the experiments or the other numerical model.

When the mean streamlines over a wave period are considered, the presence of a double pair of steady streaming cells has been shown for a weak ripple slope and a weak flow oscillation amplitude to ripple wavelength ratio r. When r is increased only the upper pair appears. In the case of steep enough ripples, the lower pair of cells is still present for a significant r. An increase in wave amplitude does not give a pattern similar to the gentle slope case as the lower pair does not vanish. Further investigations need to be done on the mechanism and the effect of these structures on the flow.

The computed mean velocities showed that different profiles could be obtained depending on the location along the ripple. Mean velocity profiles at mid-slope always featured a negative overshoot near the boundary, with a larger amplitude than the profiles above the crest and the trough. For the mean profiles above the crest and the trough, velocity overshoots have been found in both directions, but most of the profiles above the ripple crest featured a negative maximum velocity, i.e in the direction opposite to that of the waves. This study needs to be completed by experiments using Laser Doppler Velocimetry or Particle Image Velocimetry in order to get the mean experimental velocity profiles at different locations along the ripple for different flow conditions. Such experiments have not been conducted for the present thesis.

---

[12]see section 3.4.4 for the velocity definition applied to the model.

Good agreement is generally reached in the comparisons between the model and the other sources. However, as mentioned in chapter 2, the wave-induced flow above ripples can have three-dimensional aspects. Therefore, the results from the present model have to be treated with caution. To consider the three-dimensional aspect of this motion and to provide a wider description of such a flow, experiments in a wave flume have been conducted. The next chapters present the experiments conducted and the results obtained, using the information provided by chapter 2 and the numerical results shown in this chapter.

Chapter 5

Experimental arrangements

5.1   Wave flume and rippled bed characteristics

All the experiments have been carried out in the hydraulics laboratory of the Department of Civil and Environmental Engineering (University of Southampton). The experiments were carried out in a glass-sided wave flume 17 m long and 0.43 m wide internally. The wave generator is of the flap type and has active absorption (figure 5.1). The other end of the flume is fitted with foam, in order to reduce wave reflection (figure 5.2). During the experiments, wave reflection was lower than 2%. The bed of the test section, approximately 9 m long, was composed of different plates, made out of PVC plastic sheets, some featuring ripples and others just being flat, all of them being smooth. The rippled section which was 1.8 m long, constituted of five rippled panels, and was located in the middle of the tank. The water depth over the test section was 0.56 m. A sketch of a top and side view of the wave tank is shown in figure 5.3.

The ripples have been cut out from PVC sheets originally 25 mm thick. The surface cutting was done using a computer-linked machine with equations describing the rippled surface as the input. These relations are derived from measured experimental ripples and are recognized to give a good approximation of natural sea ripples (Sleath
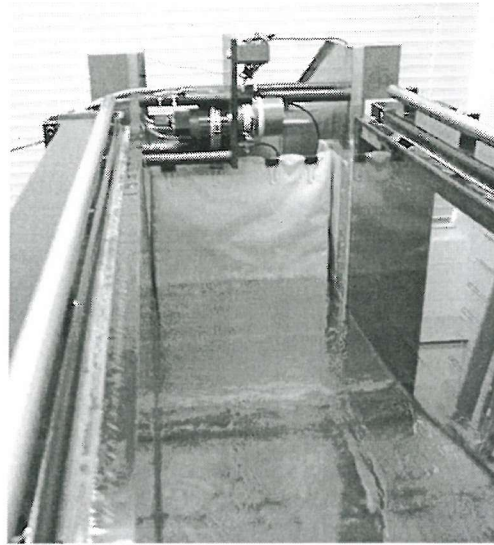
Figure 5.1: Picture of the wave-generator.
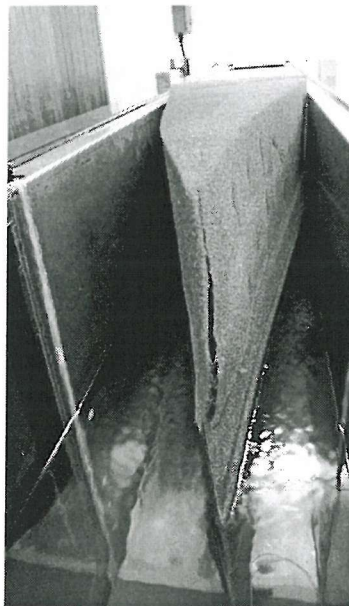
Figure 5.2: Picture of the triangular-shaped foam used to avoid wave reflection, fitted at the end of the wave flume.
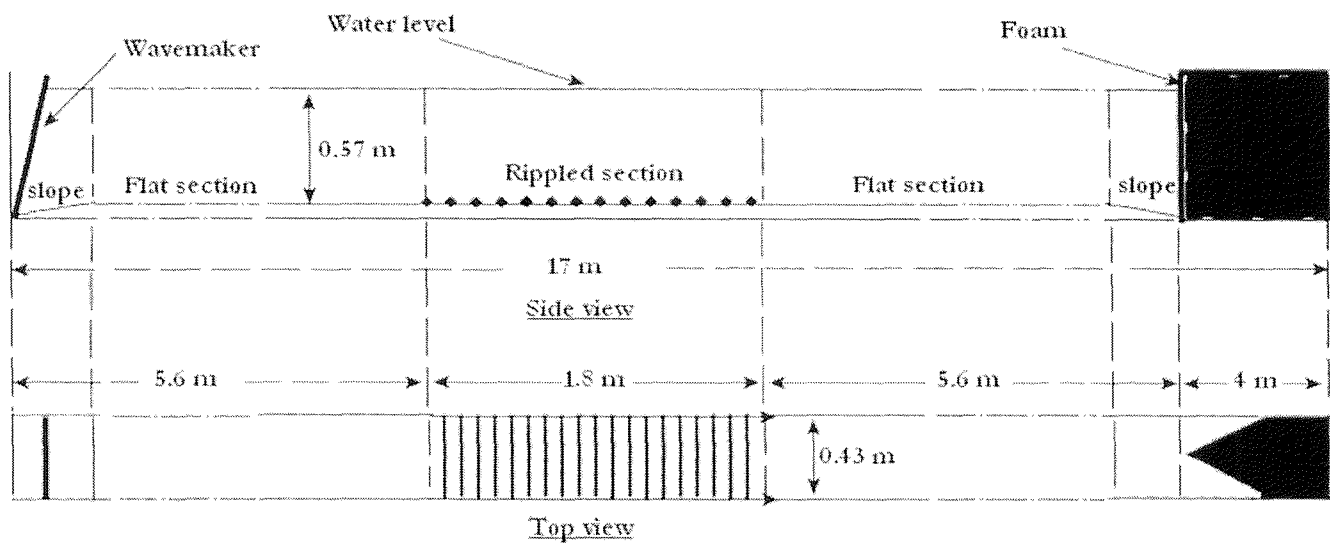
Figure 5.3: Top and side view of the wave flume, fitted with a rippled section on the bottom.

(1984a, p131-133) and section 2.7.2). These equations are:

$$x = \xi - \frac{h_r}{2} sin(k_r \xi), \tag{5.1}$$

$$y = \frac{h_r}{2} cos(k_r \xi) \tag{5.2}$$

where h_r is the ripple height, k_r the wave number and ξ a dummy variable. A photograph of the rippled section is shown in figure 5.4.
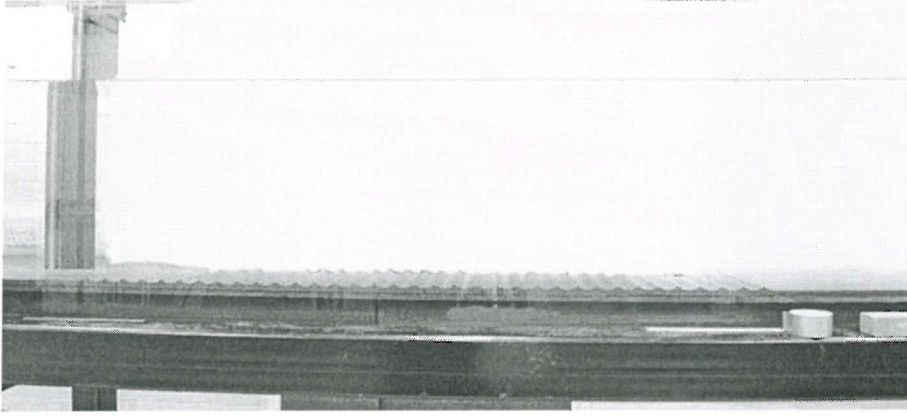
Figure 5.4: Picture of the rippled section.

Four different sets of rippled panels were manufactured and used in the wave tank. In terms of ripple slope, the range covered goes from a gentle to a steep slope (table 5.1). In cartesian coordinates, the radius of curvature of a surface is:

$$R = \left(1 + (\frac{dy}{dx})^2\right)^{3/2} \left(\frac{d^2y}{dx^2}\right)^{-1}. \tag{5.3}$$

Then, from formulas (5.1) and (5.2) the radius of curvature of the present ripples is:

$$R_\xi = \frac{(4 - 4h_r k_r \cos(k_r \xi) + h_r^2 k_r^2)^{3/2}}{2h_r k_r^2 (2\cos(k_r \xi) - h_r k_r)}. \tag{5.4}$$

The radius of curvature at the crest, for $\xi = 0$, is then

$$R_c = \frac{1}{2} \frac{(h_r k_r - 2)^2}{h_r k_r^2} \tag{5.5}$$

96

and the radius of curvature at the trough, for $\xi = \pi/k_r$, is

$$R_t = \frac{1}{2}\frac{(h_r k_r + 2)^2}{h_r k_r^2}.$$

(5.6)

The radius of curvature at the crest for the present ripples is in the range 3 mm < R_c < 28.8 mm. Table 5.1 is a summary of the characteristics of the ripples used for the experiments. Figure 5.5 shows the four different ripple profiles used in the experiments.

Ripple set	l_r (mm)	h_r (mm)	slope $s_r = h_r/l_r$	R_c (mm)	R_t (mm)
1	40	2	0.05	28.8	54.3
2	40	4	0.1	9.5	35.0
3	40	4.8	0.12	6.6	32.0
4	51.4	9	0.175	3	35.8

Table 5.1: Experimental ripple characteristics.
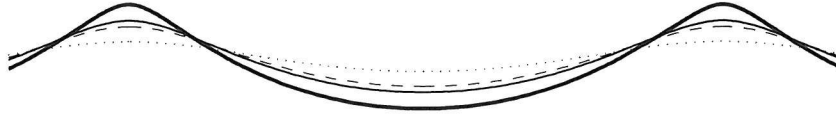
Figure 5.5: Ripple profiles used in the experiments obtained with formulas (5.1) and (5.2); (...) s_r=0.05; (- -) s_r=0.1; (–) $s_r = 0.12$; (—) $s_r = 0.175$.

5.2   Technique of visualization

Flow visualizations were carried out with a system releasing a fluorescent mixture through a hole located at a ripple trough, in the middle of the rippled section. A bottle was fitted with a 2 mm diameter flexible tube at its bottom. The tube was placed underneath the false floor, in the wave tank, and led to a copper pipe of 1

mm diameter going through the rippled panel. With the bottle placed above the wave tank water level, the dye was released at a satisfactory constant rate, controlled by a valve. The mixture used for the flow visualization was obtained by adding few drops of fluorescein to 50 *cl* of water. The temperature difference between the mixture and the water in the flume was minimized by the time of travel of the mixture from the bottle to the injection point (around 10 minutes). It seems reasonable to assume than the mixture had a density very similar to water. Figure 5.6 is a picture of the dye coming out from the hole located in the ripple trough.
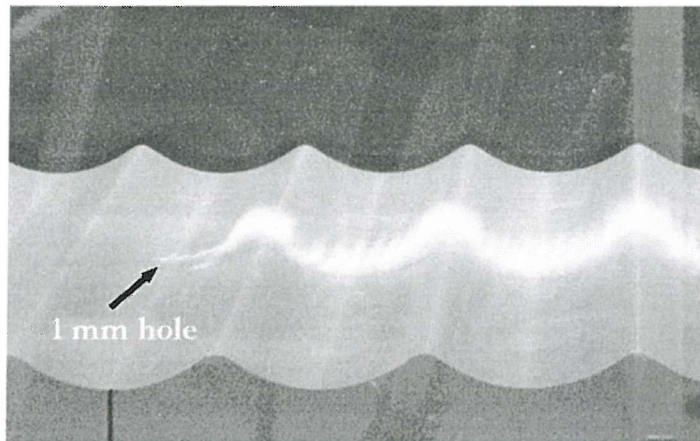
Figure 5.6: Picture of the dye coming through the 1 mm hole.

The flow patterns were then videoed using a monochrome high speed digital video camera (PULNIX TM-6710). Its speed of acquisition is 120 frames per second, for a resolution of 648(H)x484(V) pixels. Visualizations were made from the side and from above the flume.

5.3 Wavemaker set-up

The wavemaker was controlled with a computer generated analogue input signal. The wavemaker was programmed to play waves of definite wave periods and wave

amplitudes. The range of wave period used for the experiments was 1 to 3.13 s, while the wave height (crest to trough) range was 0.8 to 10 cm.

For large wave amplitudes, a *step method* was adopted; when the flow oscillation was too strong, it was not possible to see any flow pattern but a cloud of quickly vanishing dye. In order to delay the dye mixing, for strong flow oscillations, the wavemaker was programmed to increase the wave amplitude by chosen steps (for a fixed wave period), generating an large number of waves at each step, to make sure the flow pattern was established. In this way, strong flow oscillations could be observed, without the dye becoming too diluted. The possibility of videoing 120 frames per second in these cases was particularly helpful, as patterns could not be clearly seen for a long time.

Chapter 6

Experimental results

6.1 Introduction

As explained in chapter 5, flow visualizations have been conducted in a flume, over a rippled bed, under the influence of waves, using a neutrally buoyant dye. The dye was released through the bed, so that it could show the flow behaviour just above the ripples, in a layer very close to the bottom. Experiments have been conducted for four different ripple types from a gentle to a steep slope type. For each set of ripples a range of wave periods was used and for each wave period, different wave amplitudes were applied. The tests were all videoed from the side and from above the tank, so that two-dimensional and three-dimensional patterns could be recorded.

It is assumed that studying the flow patterns just above the ripples will help in understanding the sediment transport and the ripple evolution under various flow characteristics. It is also believed that identifying different flow regimes occurring above the ripples will help in understanding typical ripple shapes and sizes. The images showed the presence of circulation cells for weak flow, vortex ejection process above the ripple crest for stronger flow, two-dimensional instabilities and three-dimensional instabilities possibly leading to a significant change in the ripple shape (Sleath, 1984a; Hansen et al., 2001a). As the ripples are fixed, no change in ripple shape is possible but by an-

alyzing significant changes in the flow patterns, speculations can be made about the possible bed reactions and the mechanism of the instabilities involved.

The experiments conducted for this study revealed various types of flow patterns, mainly influenced by the ripple slope, the wave orbital amplitude to ripple wavelength ratio and possibly the wave period. The wide variety of flow patterns observed during these experiments can be seen in the following figures 6.1, 6.2 and 6.3. For each of these figures, the video camera was placed at the side of the tank. Each frame from figures 6.1, 6.2 and 6.3 is for a given flow and ripple characteristics. The time at which each picture was taken is arbitrary.
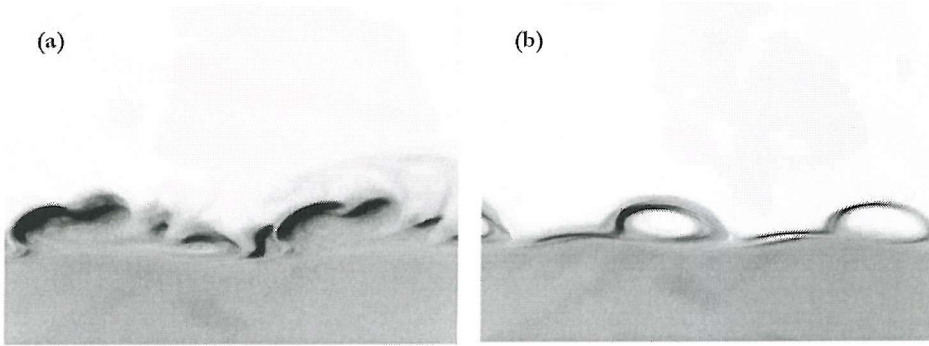
Figure 6.1: Side-view of the dye pattern over ripples; ripple slope: 0.05; (a) T=3.13 s, a=0.02 m; (b) T=2.5s, a=0.01 m; T: wave period, a: wave amplitude.

It is recalled that only the wave periods, the wave heights and the ripple characteristics are experimentally measured parameters. Parameters such as the orbital amplitude and the velocity amplitude have been calculated from formulas (2.13) and (2.35).

Important note*: in the following sections, time sequences of the flow pattern evolution are shown. It is not possible to give the exact wave phase at which each sequence starts as the high speed recording was manually triggered and not connected to any device enabling the wave phase to be recorded, such as a wave gauge for example.*

101

Figure 6.2: Side-view of the dye pattern over ripples; ripple slope: 0.175; (a) T=2 s, a=0.008 m; (b) T=2s, a=0.015 m; (c) T=1.42 s, a=0.022 m; (d) T=1 s, a=0.03 m; T: wave period, a: wave amplitude.

*However, sequences of the exact time length of the wave periods considered were isolated and studied. Hence, the wave phases shown are only **relative wave phases**, but in a sequence of images of one wave period, all the features of the oscillatory wave-induced flow are represented. It is also important to keep in mind that for all the sequences, the waves are propagating from the **left to the right**. This note applies to all the sequences showed in this chapter.*
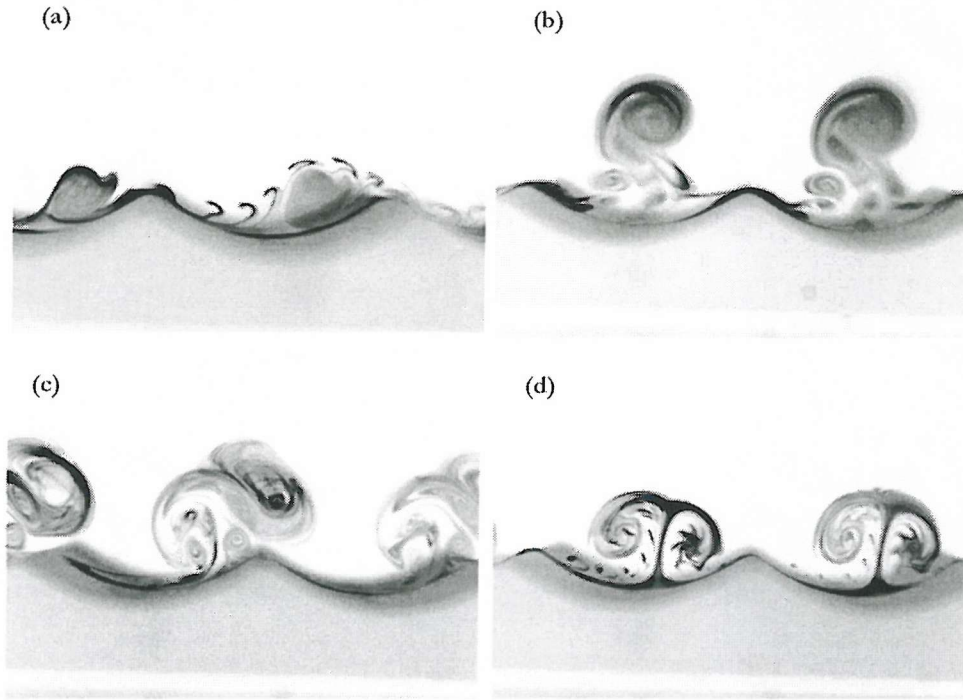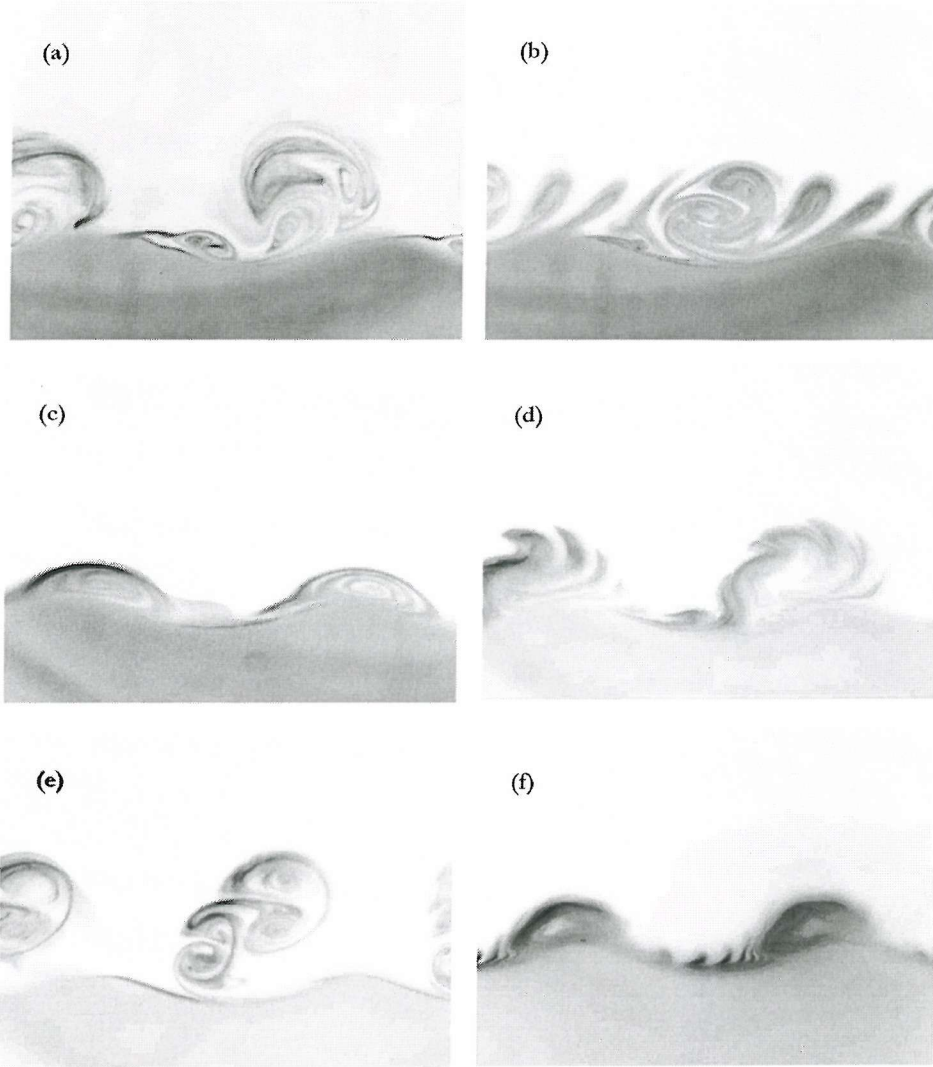
Figure 6.3: Side-view of the dye pattern over ripples; ripple slope: 0.1; (a) T=3.13 s, a =0.015 m; (b) T=2s, a=0.015 m; (c) T=1 s, a=0.03 m. Ripple slope: 0.12; (d) T=2.5 s, a=0.01 m; (e) T=2.5 s, a=0.015 m; (f) T=1.43 s, a=0.015 m; T: wave period, a: wave amplitude.

6.2 Two-dimensional regimes identification

The following sections present the main flow patterns obtained during the experiments and discuss the different mechanisms that are revealed. Started from still water, each experiment was repeated to check the consistency of the results and avoid possible effects of residual currents.

Four different regimes are identified. Their identification relies on the dye patterns observed during the experiments and are restricted to laminar conditions. The cases with strong flow oscillations, when the flow was turbulent and the dye quickly vanished or went into a blurred cloud were not studied. Each particular regime is usually found when the relevant parameters describing the experimental characteristics are in a certain range. These main parameters are: the ripple slope, the wave orbital amplitude to ripple wavelength ratio and the wave period. The classification of these regimes will rely on these parameters. It is worth recalling that the orbital amplitude to ripple wavelength ratio is defined as

$$r = \frac{a_0}{l_r} \tag{6.1}$$

and the ripple slope definition is:

$$s_r = \frac{h_r}{l_r}. \tag{6.2}$$

The Taylor number is also believed to be a relevant parameter for three-dimensional flows but it will also be used in this section for convenient comparison:

$$T_a = \frac{a_0 h_r \sqrt{R_e}}{2 l_r^2}. \tag{6.3}$$

This definition is equivalent to formula (2.32). The parameter β is used as the dimensionless form of the wave period:

$$\beta = \frac{4 R_c^2}{\nu T}. \tag{6.4}$$

6.2.1   Stable mode: "roll" pattern

For a small r in the range 0.095 to 0.8 (mean value $r = 0.26$), structures looking like cells or rolls will appear on each crest. The rolls will move slightly back and forth, oscillating with the wave-induced flow. These structures are very stable and typically two-dimensional. They are obtained for a very weak flow oscillation. To obtain this pattern, the steeper the ripple slope is, the weaker the orbital amplitude must be. The wave period seems to have a minor influence as the roll structures were obtained for any of the periods tested for a β in the range $32 < \beta < 3016$. However, for the steepest ripple slope, $s_r = 0.175$, the pattern was only obtained for the longest wave periods corresponding to $\beta = 10.45$ and $\beta = 13$. Figure 6.4 plots the Taylor number range with respect to r for which the roll structures are obtained. This regime is mainly observed for a ratio $T_a/r < 0.9$.

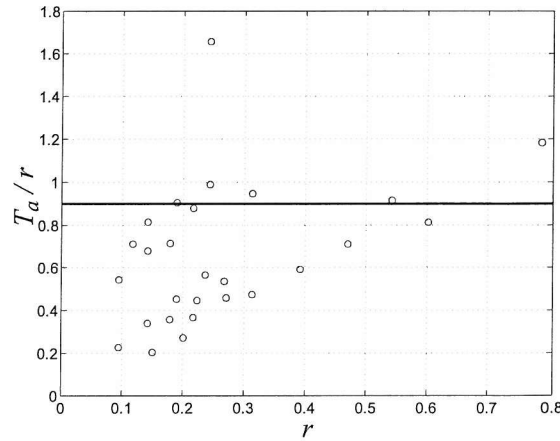*Figure 6.4: T_a/r range with respect to r for which the roll structures are observed. The horizontal line is for visual help and is arbitrary.*

Figures 6.5 and 6.6 show two typical sequences for this regime, during a wave period. As can be seen on both figures the structures are repeated on each crest. They were not observed upstream of the dye release point, as the dye could only spread downstream

following the steady drift[1] motion. Their shape is influenced by the ripple slope: for a steep ripple slope, or a strong curvature of the boundary, the rolls will be very round, as shown in figure 6.5. But for a weak ripple slope, or a weak boundary curvature, the rolls will have a more elliptic and stretched shape, as shown in figure 6.6.

These cells might be the result of a steady streaming induced when the flow oscillation amplitude is much smaller than the ripple wavelength. According to Honji et al. (1980), in such a case the flow does not separate and the regime would correspond to a rolling-grain[2] motion if the bed was movable. Honji et al. (1980) pointed out that the steady streaming above ripples for a weak flow oscillation was characterized by a double structure consisting of an upper and a lower pair of counter-rotating circulation cells[3]. In the present experiments, even in the presence of dye injected far above the ripples, no upper pair of vortices has been visualized and only one cell was present, counter-rotating from the wave propagation direction and oscillating around each crest. Honji's experiments were done in an oscillating water tunnel, while the present experiments were conducted in a wave flume. Therefore, there is at least one significant difference between the two types of oscillating flow: waves propagating in a wave flume will generate a steady drift while no such feature should be present in a flow generated in an oscillating tunnel. This difference might be very important in the case of weak flow oscillation, where the velocities close to the bed are small and could be significantly influenced by the steady drift. Moreover, according to Kaneko and Honji (1979), when the ratio of the amplitude of the wavy wall to the thickness of the Stokes layer is increased, the upper pair of circulation cells makes its way towards the boundary in the gap between the lower pair of cells, at the trough, pushing the lower cells apart. In the present experiments, this ratio is always larger than any of the ratios considered by Kaneko and Honji (1979), possibly also partly explaining the differences. The computer model presented in chapter 3 has been run for flow and

---

[1] See section 2.4

[2] See section 2.7.1

[3] See also Kaneko and Honji (1979) and other references in section 2.5.2.

Figure 6.5: *Stable regime - roll patterns; ripple slope* $s_r = 0.1$; $r = 0.18$; $\beta = 231$; *(a)* $\sigma t = 0$; *(b)* $\sigma t = 2\pi/5$; *(c)* $\sigma t = 4\pi/5$; *(d)* $\sigma t = 6\pi/5$; *(e)* $\sigma t = 8\pi/5$; *(f)* $\sigma t = 2\pi$; *all wave phases are relative phases.*

(a)　　　　　　　　　　　**(b)**

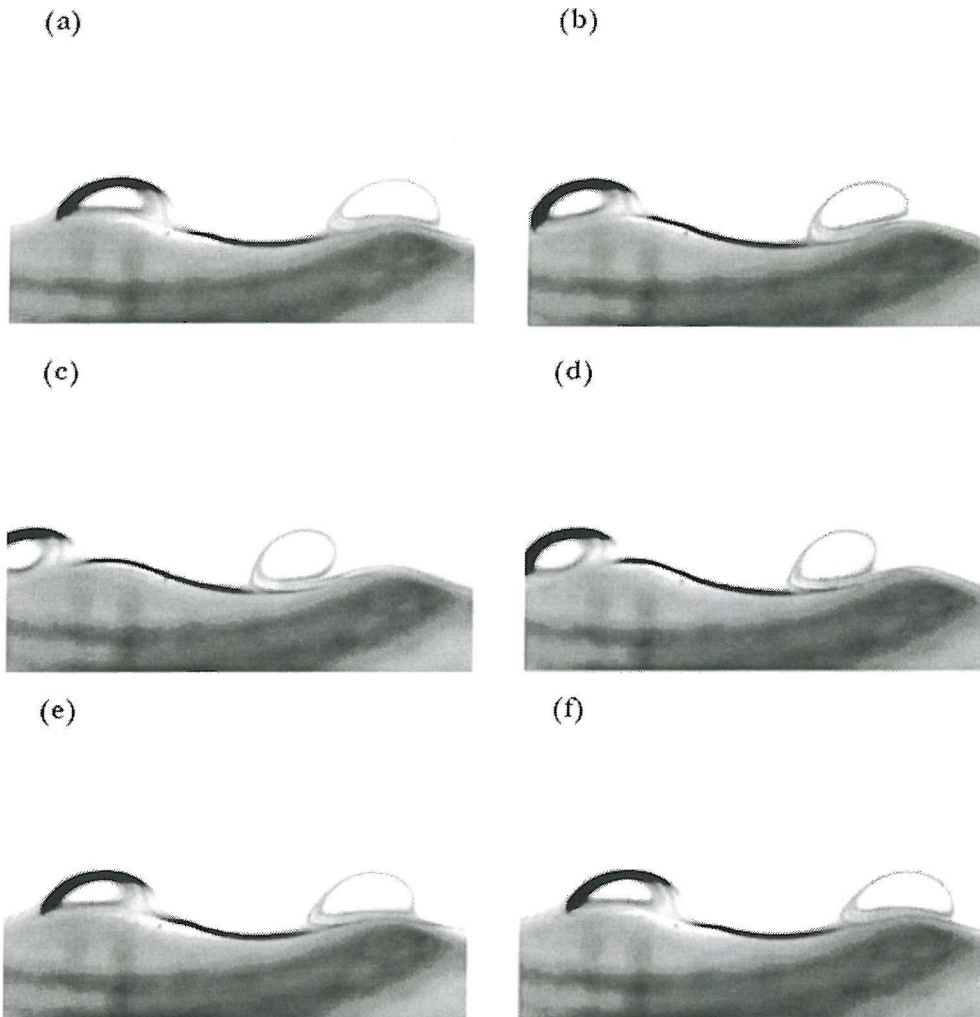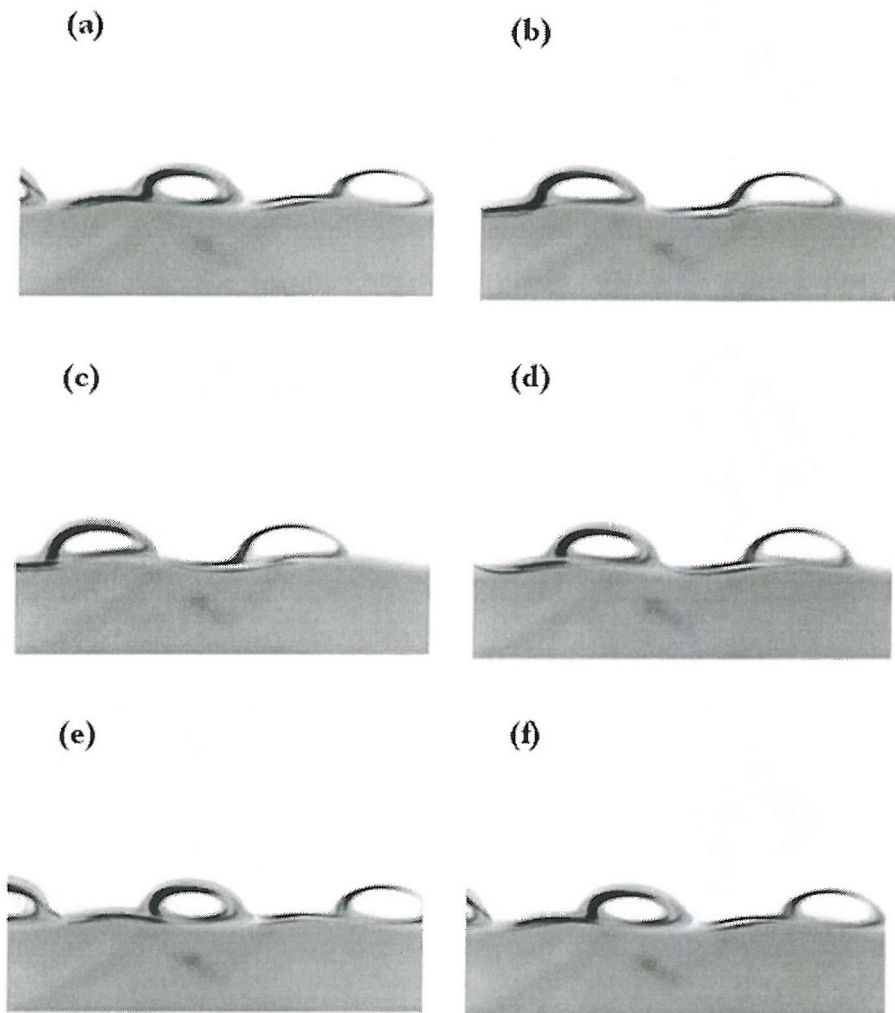**(c)**　　　　　　　　　　　**(d)**

(e)　　　　　　　　　　　**(f)**

Figure 6.6: Stable regime - roll patterns; ripple slope $s_r = 0.05$; $r = 0.31$; $\beta = 1206$; (a) $\sigma t = 0$; (b) $\sigma t = 2\pi/5$; (c) $\sigma t = 4\pi/5$; (d) $\sigma t = 6\pi/5$; (e) $\sigma t = 8\pi/5$; (f) $\sigma t = 2\pi$; all wave phases are relative phases.

108

ripple characteristics similar to the experimental conditions shown in figure 6.5. The computed mean streamlines, plotted in figure 4.29 in section 4.3.4, present a double pair of circulation cells as predicted by the theory. Similarly, figure 6.6 uses physical parameters identical to the ones used in the model when the mean streamlines are plotted in figure 4.32, section 4.3.4. The model gives only one pair of cells, as expected when the ripple slope is very small and r is significant ($r = 0.31$). The two results from the model are quite different, one presenting a double pair of cells and the other only one pair. On the other hand, the two experimental results are quite similar. Some experimental factors may have a greater influence on the flow so that the circulation structures cannot be identical to the modelled cells. It may be due to the mean drift which is present in the experiments but not in the model as a shallow water velocity definition is used[4]. Moreover, the absence of a mean drift may be a major condition for the existence of these cells pairs, as neither the experiments in an oscillating tunnel nor the analytical solutions feature a steady component in the oscillatory flow velocity.

The inside of the cells tends to fill up with time, giving the roll pattern. This filling is probably due mainly to the successive layers rolling up inside the cell and to the diffusion process. This particular cell pattern shows that there is a stable circulation over the crest of the ripples even for a very slow motion and not very steep slope as it is present for a slope as weak as s_r=0.05 (figure 6.6). This circulation might be involved in the ripple construction and its influence on the typical ripple shape might be not negligible. However, due to the very weak velocities involved, the typical mass transport for this regime must be weak, as the cells will not move away from the crests.

---

[4]See section 3.4.4.

6.2.2 Weakly unstable mode: "roll" plus jets pattern

If the orbital amplitude is slightly increased but the other parameters are kept constant, the roll patterns will turn into a more disturbed shape, with the appearance of "tongues" of dye surrounding the round structures. The range for r in these experiments is 0.075 to 1, with a mean value of 0.35. This regime occurred for all the wave periods tested ($10.45 < \beta < 3016$), and for any of the ripple slopes used[5]. This regime is mainly obtained for a ratio of Taylor number over r in the range $0.9 < T_a/r < 1.6$, as can be seen in figure 6.7.
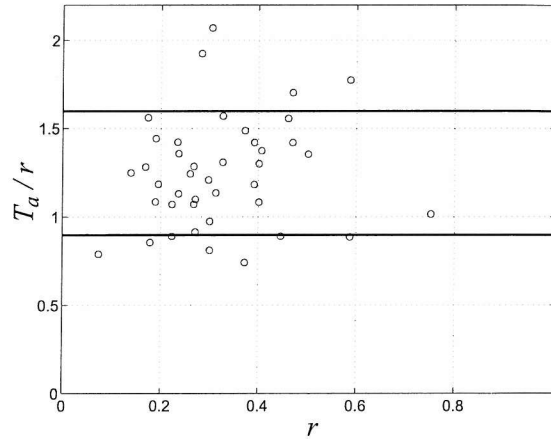
Figure 6.7: T_a/r with respect to r for which the rolls with jet structures are obtained. The horizontal line is for visual help and is arbitrary.

These weak instabilities are in the form of small tongues probably created by a jet directed upward. It seems that each layer moving over the ripple crest and starting to travel down the lee side of the crest will be subjected to this disturbance when the flow reverses. Indeed, the flow reversal seems to make the layer take off from the curved boundary, producing a jet of dye directed upward, and eventually giving a curved shape to the jet pushing the jet backward (with respect to the wave propagation direction). Then each small "tongue" of dye will drift downstream, leaving the ripple crest, for

---

[5]See table 5.1 in chapter 5 for the ripple slopes characteristics.

another jet to be created. The shapes stay very sharp as the flow oscillation is weak and the dye dilution process is very slow. The calculated flow velocity amplitude is in the range 0.02 to 0.08 m/s. For a weak r of order 0.2 on a steep slope $s_r = 0.175$ the instabilities occur quickly, but r needs to be of order 0.5, for them to happen on a weak ripple slope $s_r = 0.05$. Figure 6.8 is an example of the pattern obtained in this flow regime. The first roll on the left is just after the release point, and does not feature the small curved structures, but once the dye goes over the first crest, the small curved structures are present. It then seems that the jets are generated after moving over the ripple crest. Figure 6.8 also shows the very good repeatability of the pattern.

Figure 6.8: Roll plus jet structures; $s_r = 0.175$; $r = 0.23$; $T_a = 0.33$; $\beta = 10.45$.

The formation process of the small jets added to the still present roll patterns can be seen in the sequence showed in figure 6.9. Patterns (a) and (f) are at the same relative wave phase and are strongly similar, the structures are then stable in time. Once the jet is created, the layer marked by the dye keeps a quasi-steady shape and drifts with the flow, the instability is therefore only present at the lee side of every crest. The "tongues" reaching the next circulation cell located over the next crest will usually go over it but can eventually be incorporated in the cell.

Staying in the same regime, if r is increased, the jets of dye tend to thicken, giving a more disturbed shape added to the roll structures. This might be explained by the fact that as the wave orbital amplitude increases, the boundary layer grows, making the instability occur in a thicker layer. It can also be emphasized by a stronger dilution of the dye, giving the impression of a thicker shape. As can be seen in figure 6.10, the

Figure 6.9: *Weakly unstable mode - roll plus jet pattern; ripple slope $s_r = 0.175$; $r = 0.17$; $\beta = 16.4$; (a) $\sigma t = 0$; (b) $\sigma t = 2\pi/5$; (c) $\sigma t = 4\pi/5$; (d) $\sigma t = 6\pi/5$; (e) $\sigma t = 8\pi/5$; (f) $\sigma t = 2\pi$; (g) $\sigma t = 12\pi/5$; (h) $\sigma t = 14\pi/5$; (i) $\sigma t = 16\pi/5$; (j) $\sigma t = 18\pi/5$; all wave phases are relative phases.*

112

curved vertical"tongues" are wider than in the previous figure 6.9 and are very tight all together. The roll structure is now made out of two or three thick unstable layers rolled together. The structures are still very regular from one crest to the next.

As in the previous regime, the shape of the structures is also influenced by the curvature of the boundary or the ripple slope. In figure 6.11, where the only difference between (a) and (b) is the ripple slope, the pattern above the slope $s_r = 0.012$ (a) is rounder and thicker than the pattern above the slope $s_r = 0.01$ (b) being more flat. For the same flow conditions, the thickness of the disturbed layer seems to grow when the slope increases. The acceleration involved in the vertical jet must also be stronger for a steeper slope as the jet marked by the dye will go further upward for case (a) than for case (b), where the only difference in the physical parameters involved is the ripple slope.

In this regime, the circulation cells resulting from a steady streaming are still present, but small jets drifting in the wave propagation direction are now added to these structures. Therefore, the sediment transport must be stronger as there is an obvious drift of the jets, but the cells are still staying above each ripple.

Particular pattern: mushroom shape

A very particular pattern has been obtained during the experiments. This pattern was obtained only for one flow condition and one ripple slope. This case is placed in this section as the mechanism for obtaining such a pattern definitely involves a jet process. Figure 6.12 shows the two-dimensional mushroom shape of dye obtained for a steep slope $s_r = 0.175$, a weak orbital amplitude oscillation to ripple wavelength ratio $r = 0.11$, and $\beta = 32.7$ (wave period $T = 1$ s). Small jets similar to the ones described in the previous section can be seen, but the presence of a larger jet makes it look very different from the other pattern. This jet directed upward and approximately located at the ripple trough gets divided in two, each new section forming a vortex-like structure. This pattern deserves to be mentioned not only because of its very peculiar

113

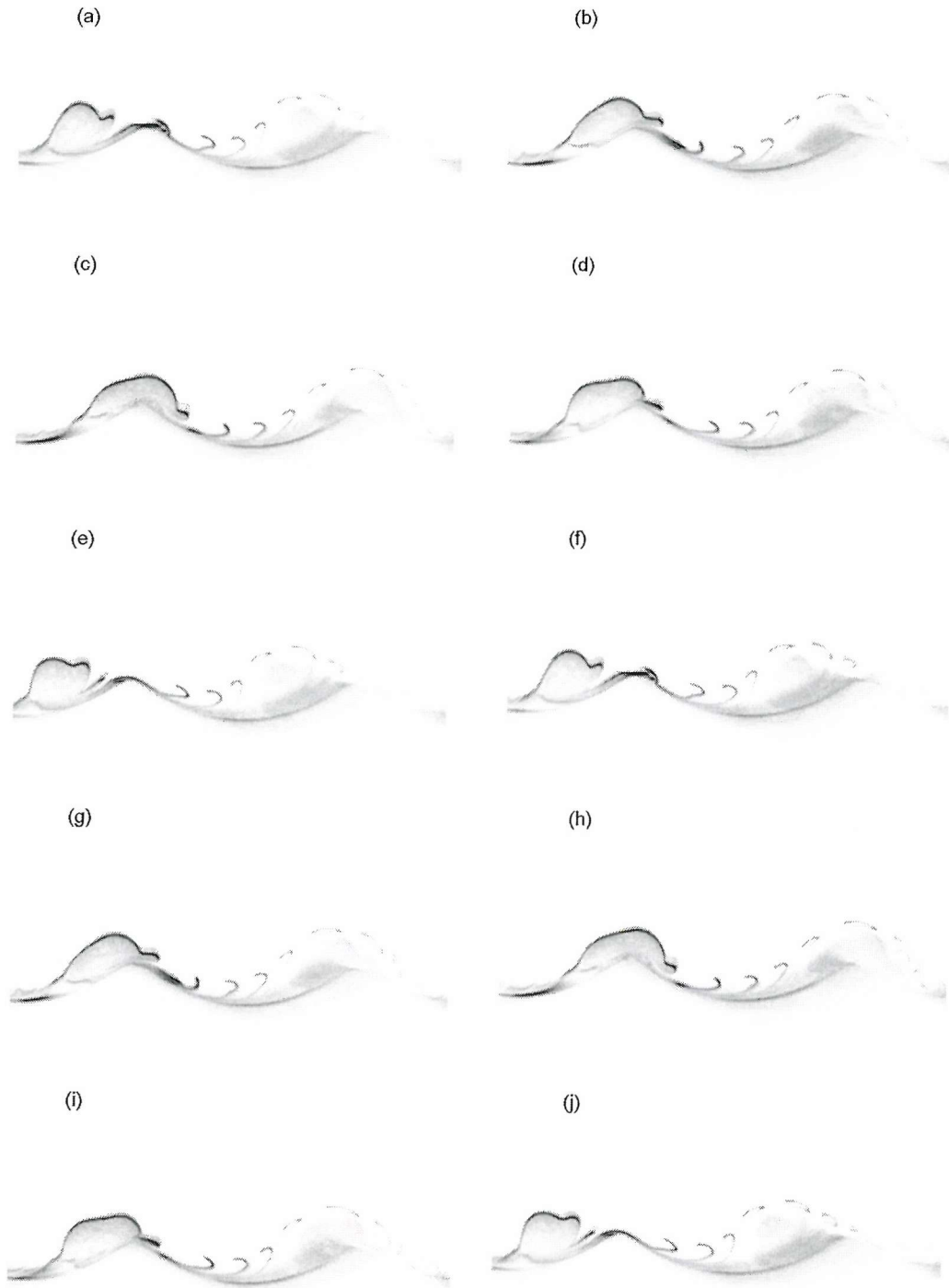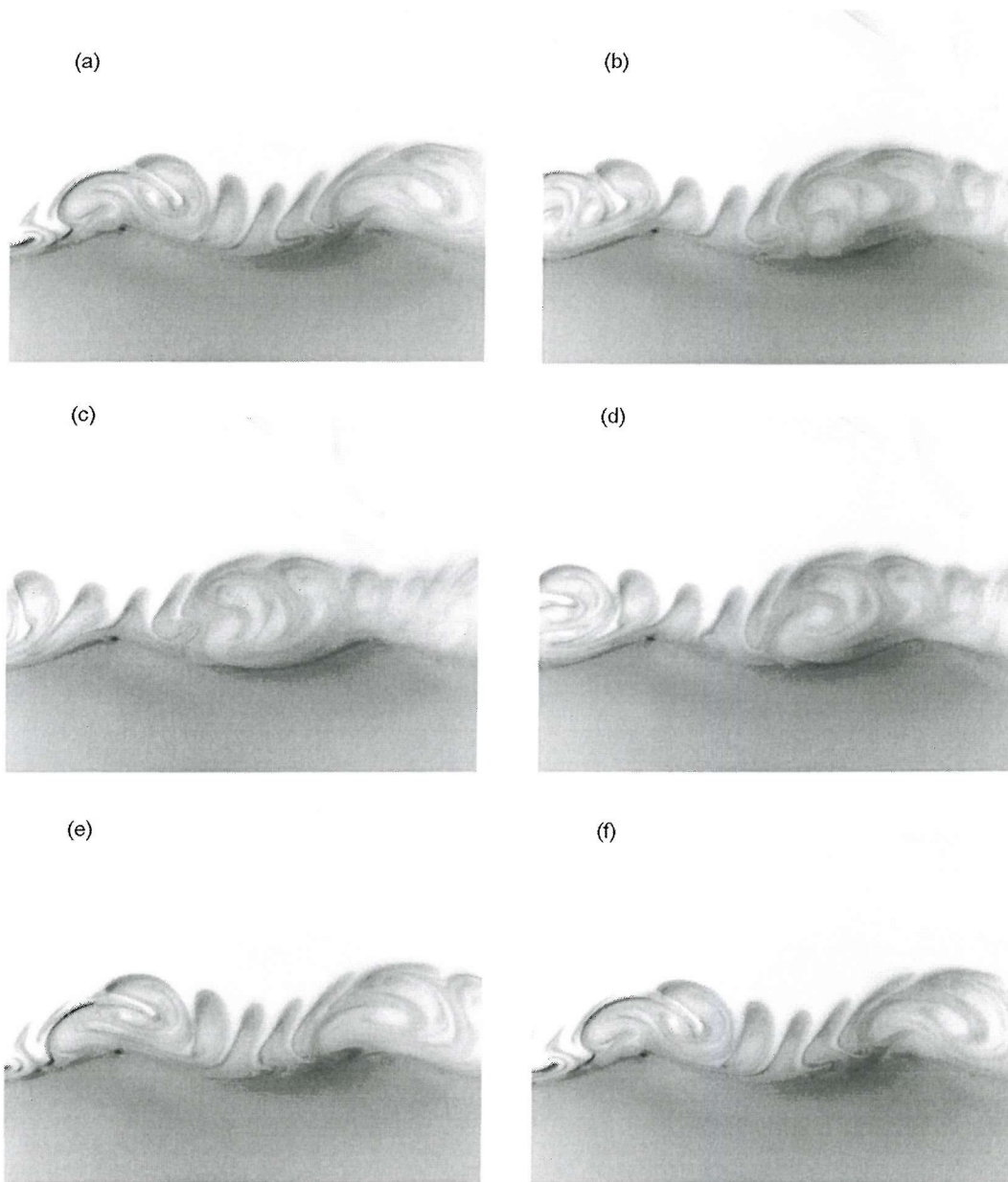(a)   (b)

(c)   (d)

(e)   (f)

Figure 6.10: Weakly unstable mode - roll plus jet pattern; ripple slope $s_r = 0.12$; $r = 0.33$; $\beta = 110.8$; (a) $\sigma t = 0$; (b) $\sigma t = 2\pi/5$; (c) $\sigma t = 4\pi/5$; (d) $\sigma t = 6\pi/5$; (e) $\sigma t = 8\pi/5$; (f) $\sigma t = 2\pi$; all wave phases are relative phases.
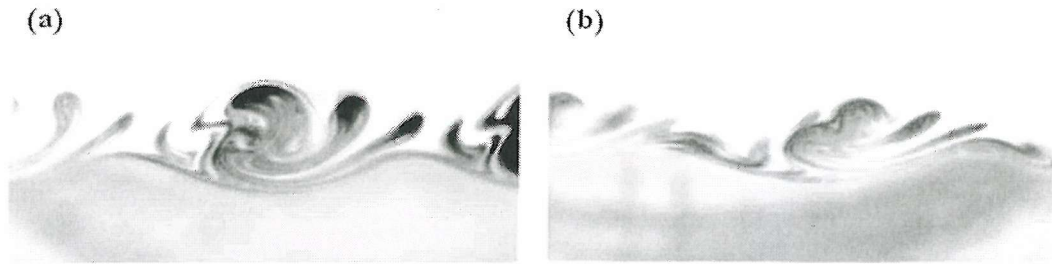
114

Figure 6.11: Influence of the boundary curvature on the dye pattern in a weakly unstable mode; $r = 0.47$; wave period $T = 2.5$ s; (a) ripple slope $s_r = 0.012$; (b) $s_r = 0.01$.

shape but also because, to the author's knowledge, it has only been previously reported by Honji et al. (1980). They carried out experiments in an oscillatory water tunnel fitted with a rippled floor made out of metal. Flows were visualized using white dye produced electrochemically. Despite not being for the exact same ripple slope and flow conditions, the similarity between figure 6.12 and figure 6.13 is striking, especially for such a complex pattern. Honji's article does not provide enough data to allow a very accurate comparison. It is worth noticing that such a structure was obtained by Honji for an oscillation frequency of 1.65 Hz, and that for the present experiment it was observed for the shortest wave period tested corresponding to an oscillation frequency of 1 Hz. Similarly, Honji stated that such a pattern was obtained for a water displacement very small compared to l_r, while it can be said the same for the present experimental case as $r = 0.11$ is small. Honji pointed out that in a case like figure 6.13, the lower vortex layer discussed in the previous regime is so small because of the low viscosity of water that only the upper layer is seen. The mushroom shape in figure 6.13 is standing vertically, while the structures in figure 6.12 are slightly tilted. It may be explained by the presence of a steady drift in a wave flume which is not a feature of the flow when a water tunnel is used. It can be assumed that such a structure can drag particles from the trough to the crest, following the path of the mushroom or tree shape as mentioned in Leeder (1999).
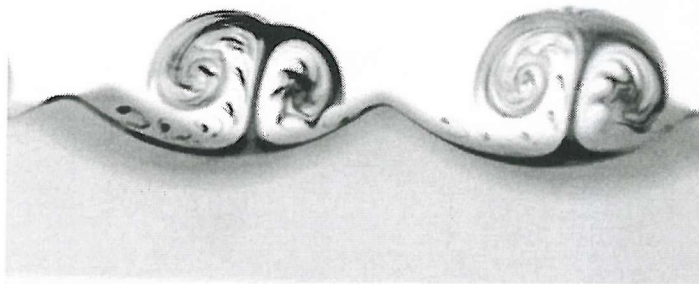
Figure 6.12: Mushroom shape - present experimental visualization; ripple slope $s_r = 0.175$; $r = 0.11$; $\beta = 32.7$ (wave period $T = 1$ s).
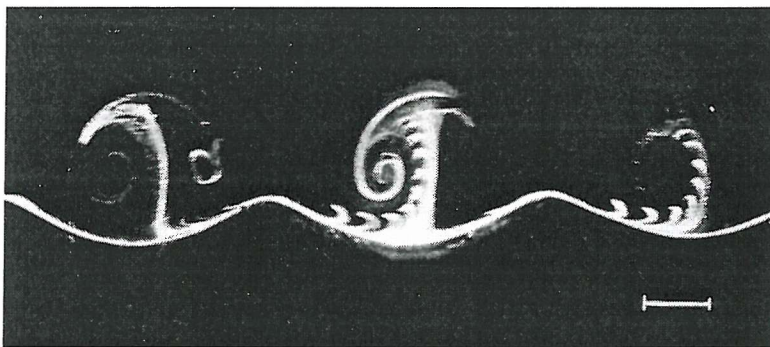
Figure 6.13: Photograph from Honji (1980, fig. 2 p226); T=0.6 s; piston displacement: 1.2 cm; scale bar: 1 cm. Visualization done with white dye educed electrochemically. Approximate ripple slope $s_r = 0.173$.

6.2.3   First flow separation regime

For r in the range 0.15 to 1.5 with a mean value increased to 0.66, the rather stable regimes previously discussed will change significantly and turn into a third regime characterized by the flow separation at the ripple crest. As seen in figure 6.14 this regime is mainly obtained for T_a/r in the range $1.6 < T_a/r < 1.8$. The mean value $r = 0.66$ is nearly twice as large as the mean value obtained for the previous regime. The flow oscillation amplitudes and the velocities involved in this regime are then remarkably stronger than for the previous regimes. It seems that having the orbital amplitude larger than half the ripple wavelength is a significant threshold for the flow characteristics.
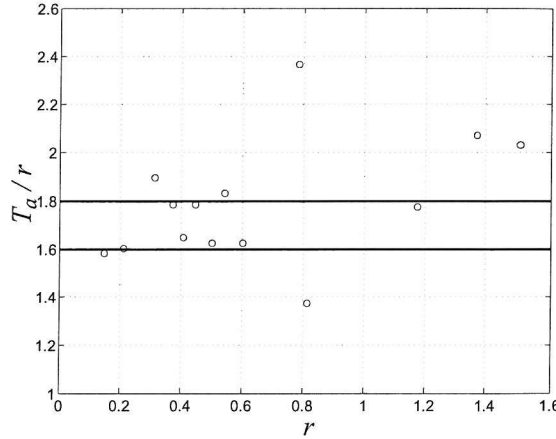
Figure 6.14: T_a/r with respect to r for which first separation occurs. The horizontal line is for visual help and is arbitrary.

The flow features in this transitional regime have to be distinguished from the previous modes typically two-dimensional and very stable in terms of spatial and time repeatability. It is also distinct from the regime detailed in the next section 6.2.4 where the main feature is the regular vortex ejection from each ripple crest occurring during each half-wave period. This regime has then to be considered as a transitional state between two significant regimes: the regimes previously described in sections 6.2.1 and

117

6.2.2 and the vortex ejection regime. As will be seen in section 6.3, this regime is also important as it usually corresponds to the transition between two-dimensional and three-dimensional flow patterns. Both circulation cells and vortices ejected from the ripple crests can be obtained. The complex dye patterns observed make the interpretation of the typical mechanisms involved in this regime particularly difficult.

The circulation cells tend to be very disturbed, but their overall shape is still almost round. The strong velocities creating the jets of dye make the cells look wider and moving higher upward from the crest. The flow separates at the ripple crest, creating a vortex structure. The vortices will drift along the boundary, moving over the crest, then down the lee-side before being lifted by the jets observed in the previous mode. The circulation cells now feature vortices as well as jets in their structure. The vorticity of each vortex structure vanishes very quickly once in the cell, as the vortex pattern is not much modified after its inclusion in the cell. Figure 6.15 is an example of the patterns obtained for $r = 0.5$. Figure 6.16 is another example for a weaker ripple slope and a stronger flow oscillation, with $r = 0.78$. In figure 6.16, the vortices can be clearly distinguished. As mentioned before, the vortices are not ejected from the ripple crest, but will eventually move upward away from the boundary at the lee-side of the ripple. In the experiments, as the flow oscillation is stronger than for the previous regimes, the dye tends to dilute quite quickly giving blur patterns. One possible effect is to give larger patterns, as the dye diffuses quicker through the neighbouring layers. In figure 6.16, pictures (a) and (f) taken at the same relative wave phase do not show a similarity as good as for the previous cases. However, the most important mechanism in this regime is the flow separation. The cloud of dye more or less detached from the bottom is less important, and its existence mainly shows that once the vortex is pushed upward by the jet, and joins the cloud of dye, the velocity at this depth above the ripples mostly has a horizontal component. Figure 6.17 shows similar patterns but for a very weak ripple slope $s_r = 0.05$ and a strong $r = 0.81$. In figure 6.17, due to the strong flow oscillation the vortices are nearly ejected from the ripple crest, but the

118

Figure 6.15: First flow separation regime; ripple slope $s_r = 0.12$; $r = 0.5$; $\beta = 50.6$; (a) $\sigma t = 0$; (b) $\sigma t = 2\pi/5$; (c) $\sigma t = 4\pi/5$; (d) $\sigma t = 6\pi/5$; (e) $\sigma t = 8\pi/5$; (f) $\sigma t = 2\pi$; all wave phases are relative phases.

very weak slope makes them have a nearly horizontal trajectory. It then seems that the vortices are still moving along the slightly curved boundary, being eventually pushed

upward at the flow reversal by the jet process. The vortices generated during the previous wave periods can be distinguished, accumulated in the cloud of dye located above the ripples.

Figure 6.16: First flow separation regime; ripple slope $s_r = 0.1$; $r = 0.78$; $\beta = 131.3$; (a) $\sigma t = 0$; (b) $\sigma t = 2\pi/5$; (c) $\sigma t = 4\pi/5$; (d) $\sigma t = 6\pi/5$; (e) $\sigma t = 8\pi/5$; (f) $\sigma t = 2\pi$; all wave phases are relative phases.
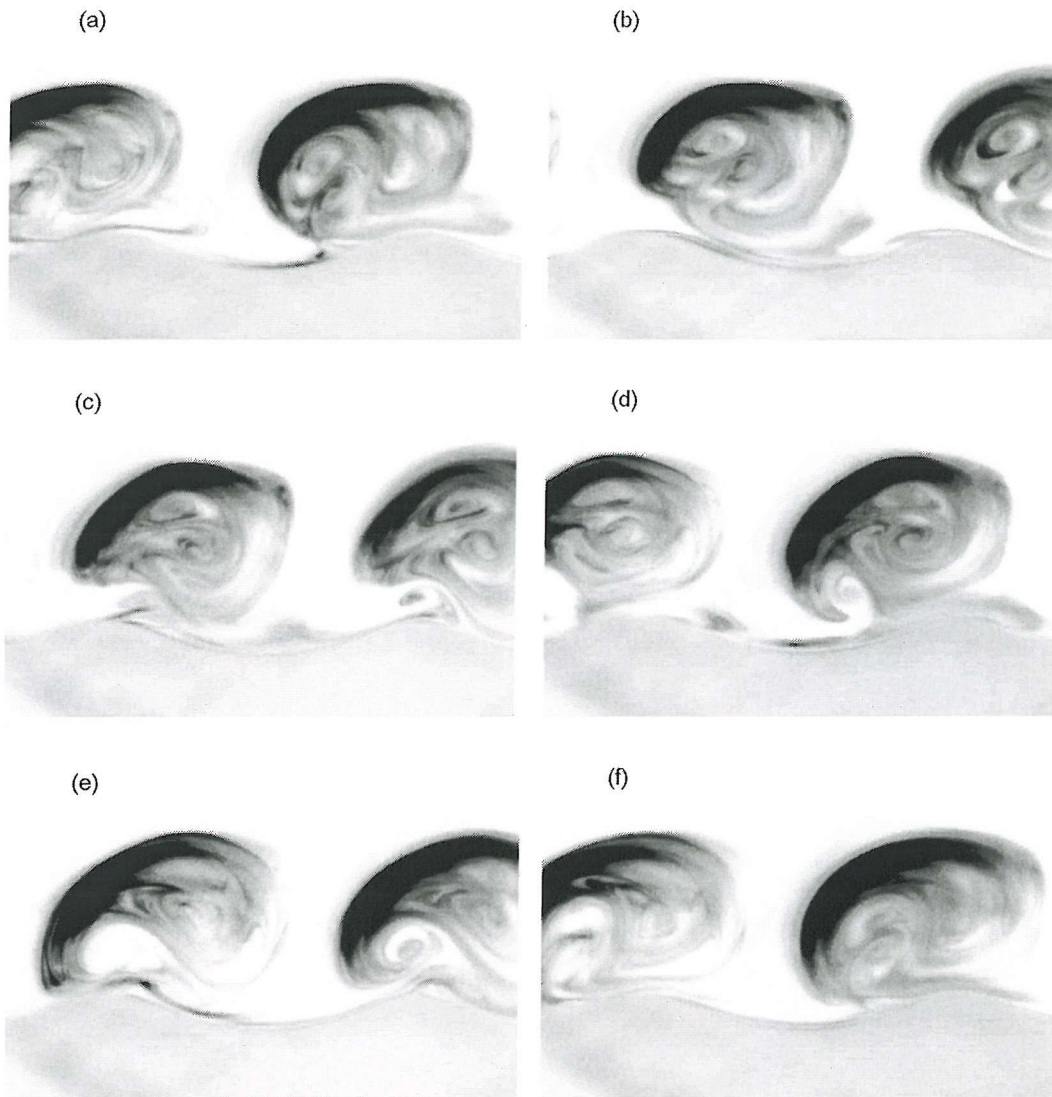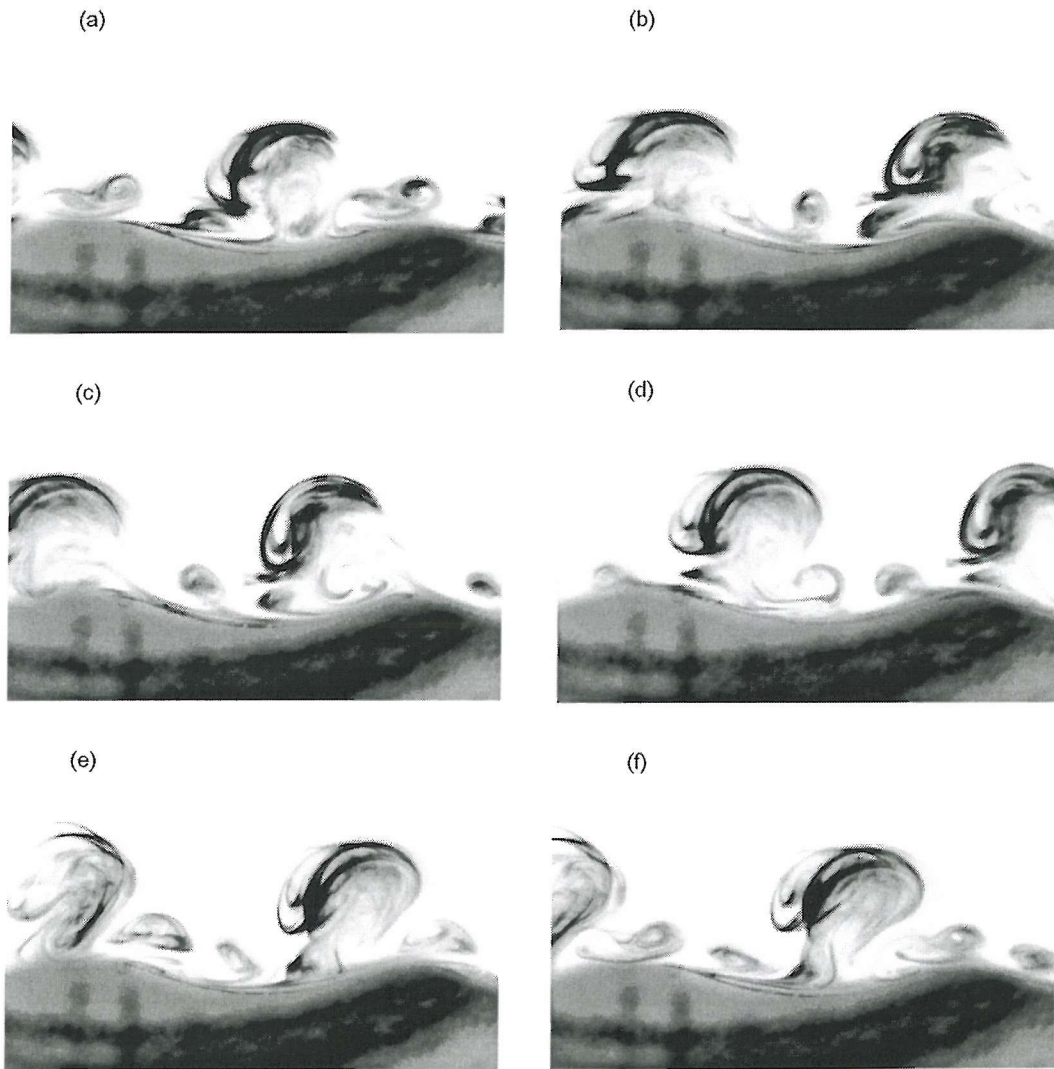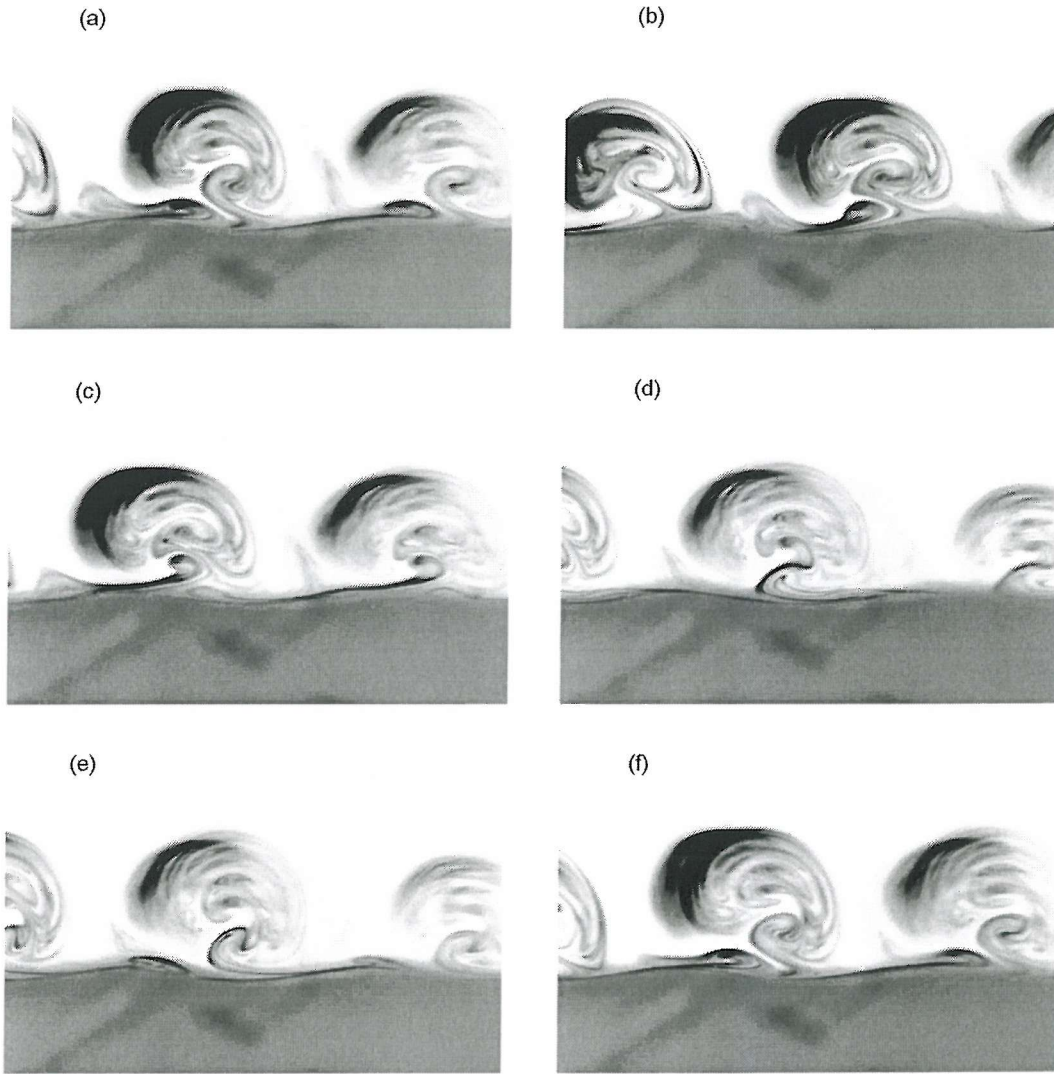
Figure 6.17: First flow separation regime; ripple slope $s_r = 0.05$; $r = 0.81$; $\beta = 1508$; (a) $\sigma t = 0$; (b) $\sigma t = 2\pi/5$; (c) $\sigma t = 4\pi/5$; (d) $\sigma t = 6\pi/5$; (e) $\sigma t = 8\pi/5$; (f) $\sigma t = 2\pi$; all wave phases are relative phases.

6.2.4 Vortex ejection regime

In the previous section, a regime for which the flow first separates has been presented. The regime studied in the present section is characterized by the flow separation and a vortex ejection from the ripple crest during each half-wave period. As seen in section 2.5.4, this regime has been widely studied before, but mainly by means of numerical modelling. In the present experiments, it has been observed for a range of values of r from 0.2 up to 1.2, with a mean value of 0.54. This mean value is lower than the calculated mean value for the previously shown regime, but it can be explained by the fact that the ripple slope seems to play a major role in this regime along with the orbital amplitude. No clear ejection has been witnessed with the weakest slope $s_r = 0.05$, but vortex ejection occurred for all the other slopes. This regime is obtained for T_a/r in the range $1.8 < T_a/r < 3.5$, as showed in figure 6.18.
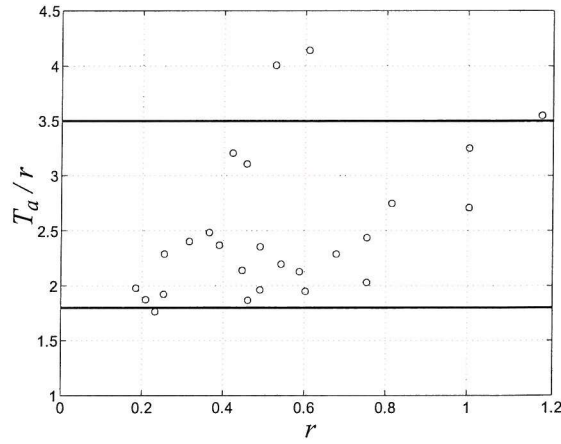
Figure 6.18: T_a/r with respect to r for which vortex ejection is observed. The horizontal line is for visual help and is arbitrary.

The ripple slope plays here a significant role as the steeper the slope is, the more likely vortex ejection is to happen. As shown in figure 6.19, the steeper the ripples, the smaller the orbital amplitude to ripple wavelength ratio has to be for the vortex ejection to occur. From this figure, speculation can be made on the fact that the smaller the

ripple slope is, the less obvious the vortex ejection threshold is. It can be assumed that vortex ejection could have been obtained for the smallest slope $s_r = 0.05$ but the flow oscillation amplitude needed would have been too difficult to generate with the wave-maker and visualizations would probably not have been possible.
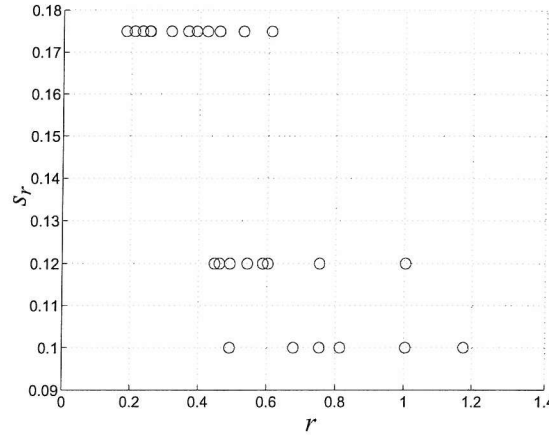
Figure 6.19: Vortex ejection for the different ripple slopes s_r.

Figure 6.20 is a sequence showing two vortex ejections, one during the first part of the wave cycle and another during the second part of the cycle. The flow separates at the ripple crest creating a vortex structure. Then the structure tends to increase in size and strength, even through the beginning of the deceleration phase. When the flow reverses, the vortex structure is convected away from the ripple crest by the local velocity. At the same time a new vortex is generated on the other side of the crest, to be ejected in the opposite direction. Once a vortex is ejected, it moves upward, joining a cloud of dye formed with the vortices ejected during the previous wave cycles. Figures 6.21 and 6.22 provide a closer view of the two vortex ejections. In figure 6.21 (c), in addition to the main vortex rotating anti-clockwise a second smaller vortex rotating clockwise is present. This vortex pair mechanism has been pointed out before by Blondeaux and Vittori (1991), as a result of their numerical model. This secondary vortex forming below the main vortex when ejected over the crest is here clearly shown.

Figure 6.20: Vortex ejection regime; ripple slope $s_r = 0.175$; $r = 0.46$; $\beta = 13$; (a) $\sigma t = 0$; (b) $\sigma t = \pi/5$; (c) $\sigma t = 2\pi/5$; (d) $\sigma t = 3\pi/5$; (e) $\sigma t = 4\pi/5$; (f) $\sigma t = \pi$; (g) $\sigma t = 6\pi/5$; (h) $\sigma t = 7\pi/5$; (i) $\sigma t = 8\pi/5$; (j) $\sigma t = 9\pi/5$; all wave phases are relative phases.

124

It seems that the angle with which the vortex is ejected can be different depending on the instantaneous flow direction. In figure 6.21, the flow direction is left to right, in the same direction as the wave propagation and the steady drift. The vortex is ejected from the crest but does not go upward and nearly follows a horizontal trajectory instead. In figure 6.22, where the flow and the wave propagation are in opposite directions, the vortex ejected in the second half of the wave cycle moves upward following the plan of the ripple slope. The steady drift may make the vortex travel more horizontally when the instantaneous velocity is in the same direction as the steady velocity, and by opposition when the vortex is ejected against the steady flow direction, the steady drift might force the vortex to move upward. The ripples used are fixed in shape, so if the flow motion was purely oscillatory, the vortex ejection should be similar in the two directions.
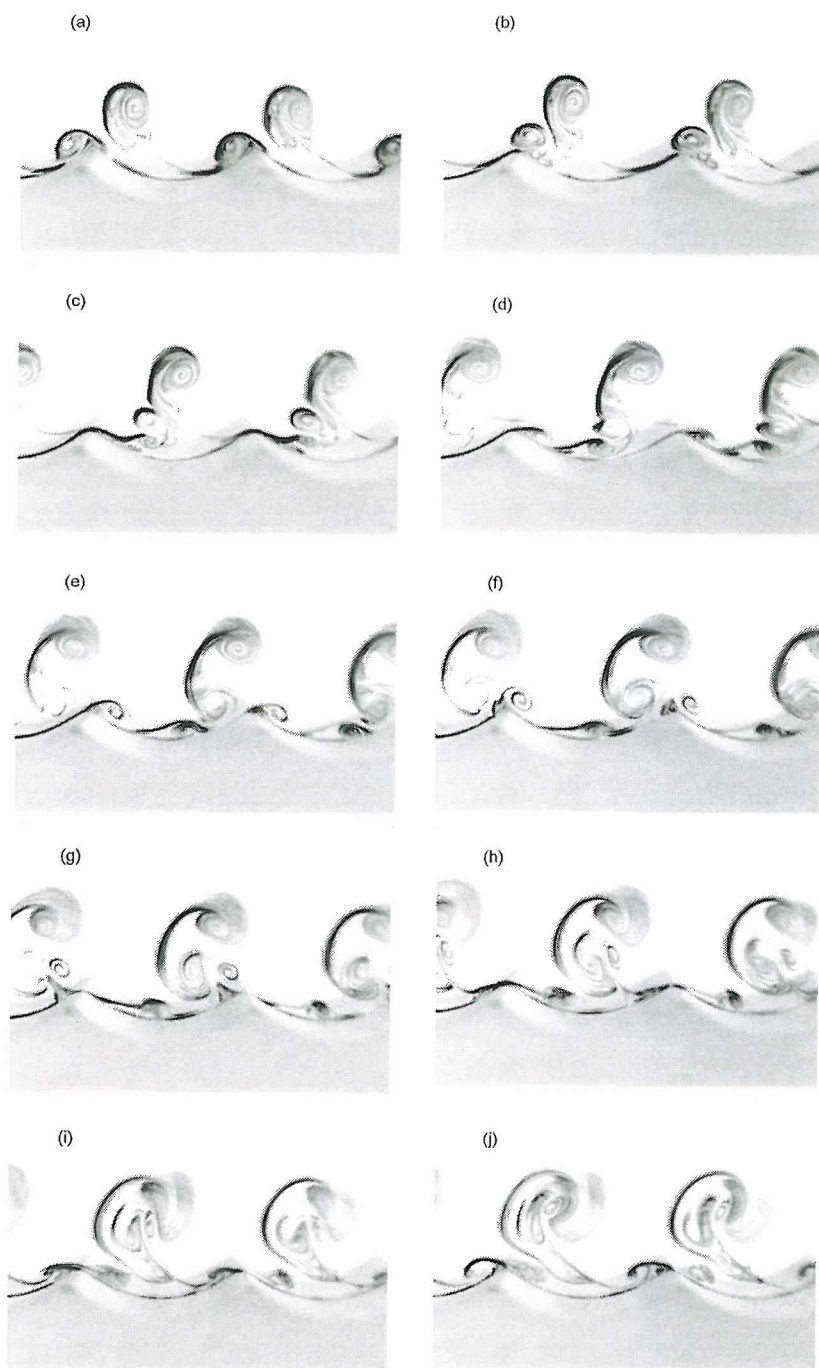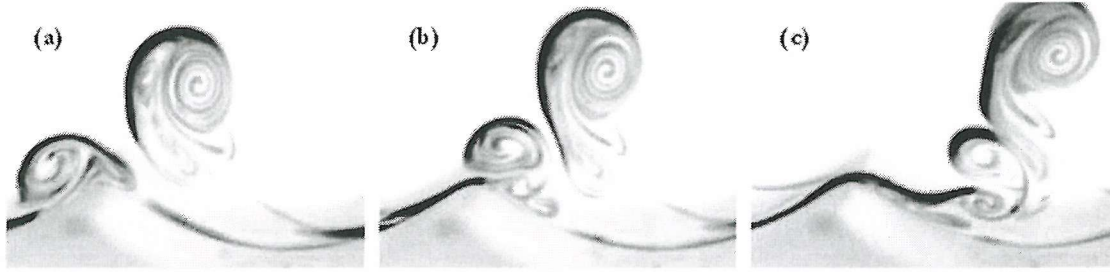

Figure 6.21: Vortex ejection regime; ripple slope $s_r = 0.175$; $r = 0.46$; $\beta = 13$; (a) $\sigma t = 0$; (b) $\sigma t = \pi/5$; (c) $\sigma t = 2\pi/5$; wave phases are similar to figure 6.20.

Figure 6.23 shows a sequence featuring vortex ejection for a ripple slope $s_r = 0.12$ and $r = 0.45$. Despite a similar value of r, the vortex size is smaller than for the case showed in figure 6.20. This difference can come from both a shorter wave period and a weaker ripple slope. This might be explained by the fact that the longer the wave period is, the more time the vortex has to build up before being ejected. The slope also plays a role in the vorticity building, as discussed in the previous sections. Figure 6.24 brings a closer view to the vortex ejection for the wave phases (a) and (b) of figure 6.23.

Figure 6.22: Vortex ejection regime; ripple slope $s_r = 0.175$; $r = 0.46$; $\beta = 13$; (a) $\sigma t = 4\pi/5$; (b) $\sigma t = \pi$; (c) $\sigma t = 6\pi/5$; wave phases are similar to figure 6.20.

The secondary vortex structure below the main vortex noticed in sequence 6.21 can also be seen. This particular mechanism is again noticed when the instantaneous flow is in the same direction as the steady drift. Another visualization of vortex ejection is showed in figure 6.25. As shown in frame (g), this case also presents a secondary vortex along with the main ejected vortex when the flow is in the same direction as the wave propagation. A close-up of part of figure 6.25(g) shown in figure 6.26 reveals more clearly the presence of the vortex pair.

Figure 6.27 shows another vortex ejection sequence for the first part of a wave cycle. The slope being weak, $s_r = 0.1$, the flow oscillation needs to be strong, $r = 0.81$; as a result the patterns obtained for the second part of the wave cycle are not shown, the dye being too diluted, no clear shape could be identified.

126

Figure 6.23: Vortex ejection regime; ripple slope $s_r = 0.12$; $r = 0.45$; $\beta = 110.8$; (a) $\sigma t = 0$; (b) $\sigma t = 2\pi/7$; (c) $\sigma t = 4\pi/7$; (d) $\sigma t = 6\pi/7$; (e) $\sigma t = 8\pi/7$; (f) $\sigma t = 10\pi/7$; (g) $\sigma t = 12\pi/7$; (h) $\sigma t = 2\pi$; all wave phases are relative phases.
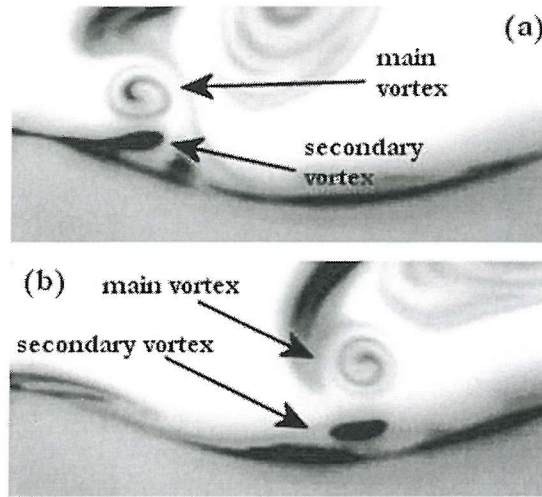
Figure 6.24: Vortex pair ejection; ripple slope $s_r = 0.12$; $r = 0.45$; $\beta = 110.8$; (a) $\sigma t = 0$; (b) $\sigma t = 2\pi/7$; all wave phases are similar to phases in figure 6.23.

(a)

(b)

(c)

(d)

(e)

(f)

(g)

(h)

Figure 6.25: Vortex ejection regime; ripple slope $s_r = 0.175$; $r = 0.41$; $\beta = 16.4$; (a) $\sigma t = 0$; (b) $\sigma t = 2\pi/7$; (c) $\sigma t = 4\pi/7$; (d) $\sigma t = 6\pi/7$; (e) $\sigma t = 8\pi/7$; (f) $\sigma t = 10\pi/7$; (g) $\sigma t = 12\pi/7$; (h) $\sigma t = 2\pi$; all wave phases are relative phases.

Figure 6.26: Vortex pair ejection; ripple slope $s_r = 0.175$; $r = 0.41$; $\beta = 16.4$; zooming of figure 6.25 picture (g).
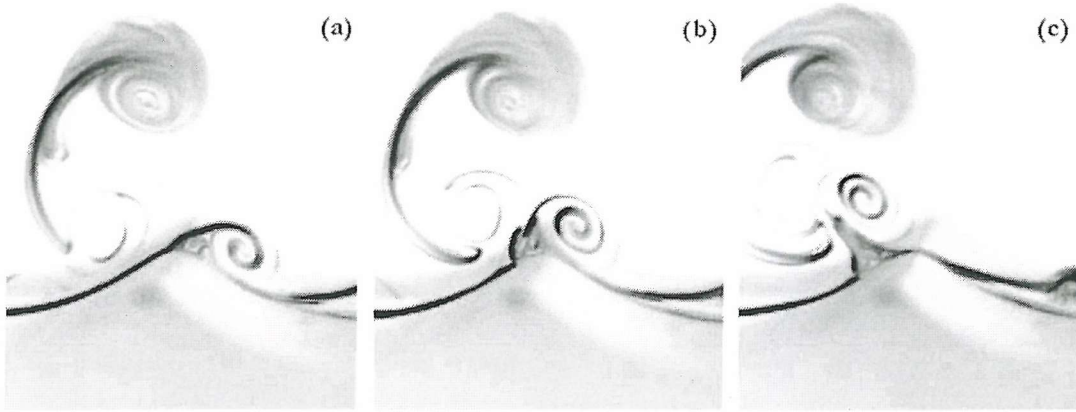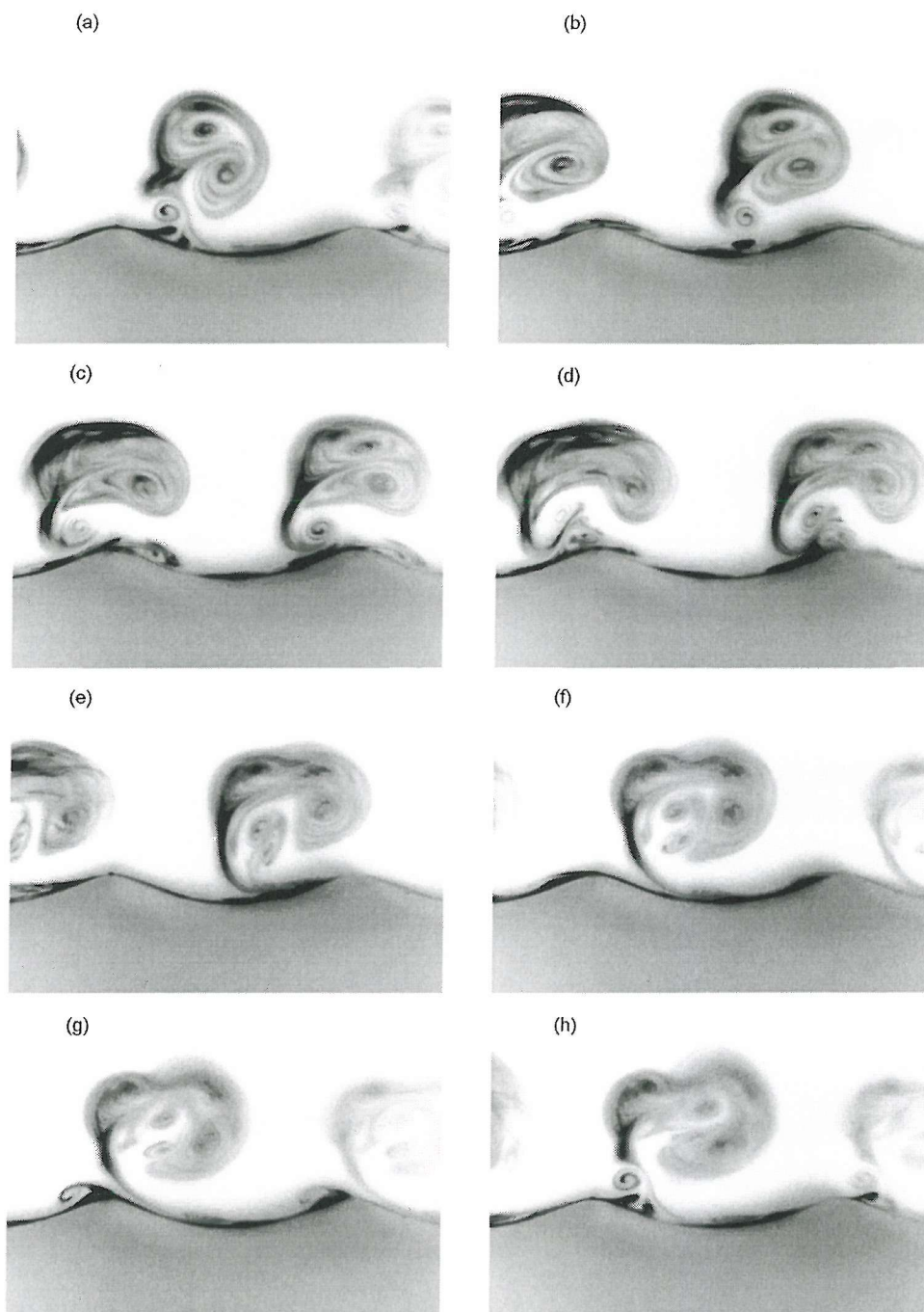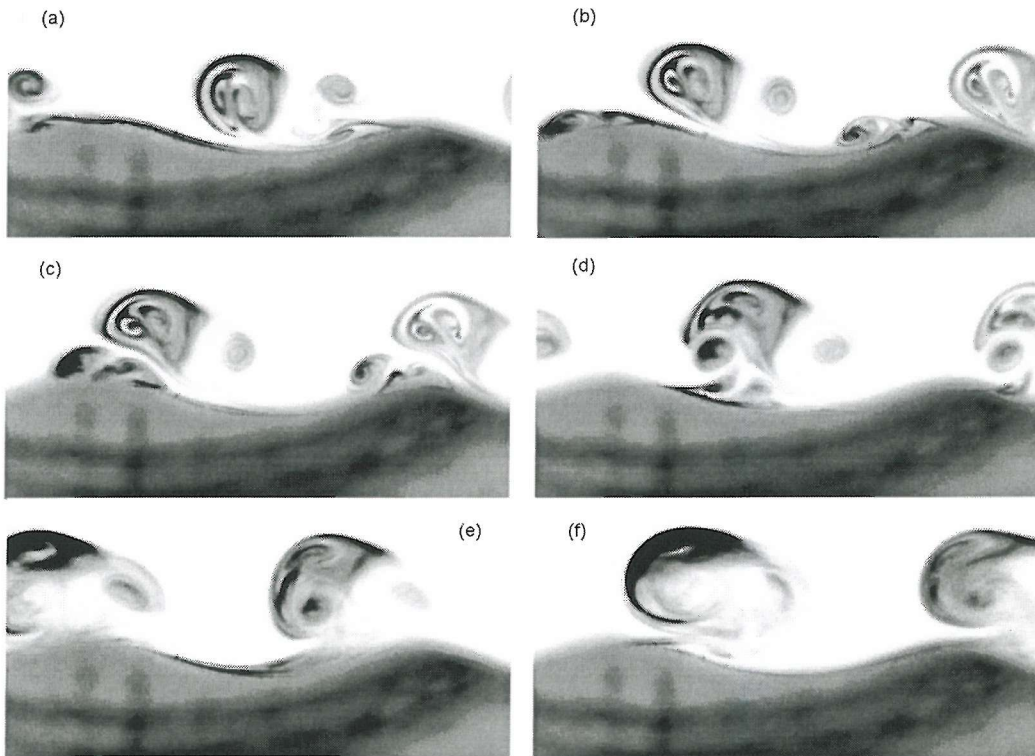

Figure 6.27: Vortex ejection regime; ripple slope $s_r = 0.1$; $r = 0.81$; $\beta = 164$; (a) $\sigma t = 0$; (b) $\sigma t = \pi/6$; (c) $\sigma t = \pi/3$; (d) $\sigma t = \pi/2$; (e) $\sigma t = 2\pi/3$; (f) $\sigma t = 5\pi/6$; all wave phases are relative phases.
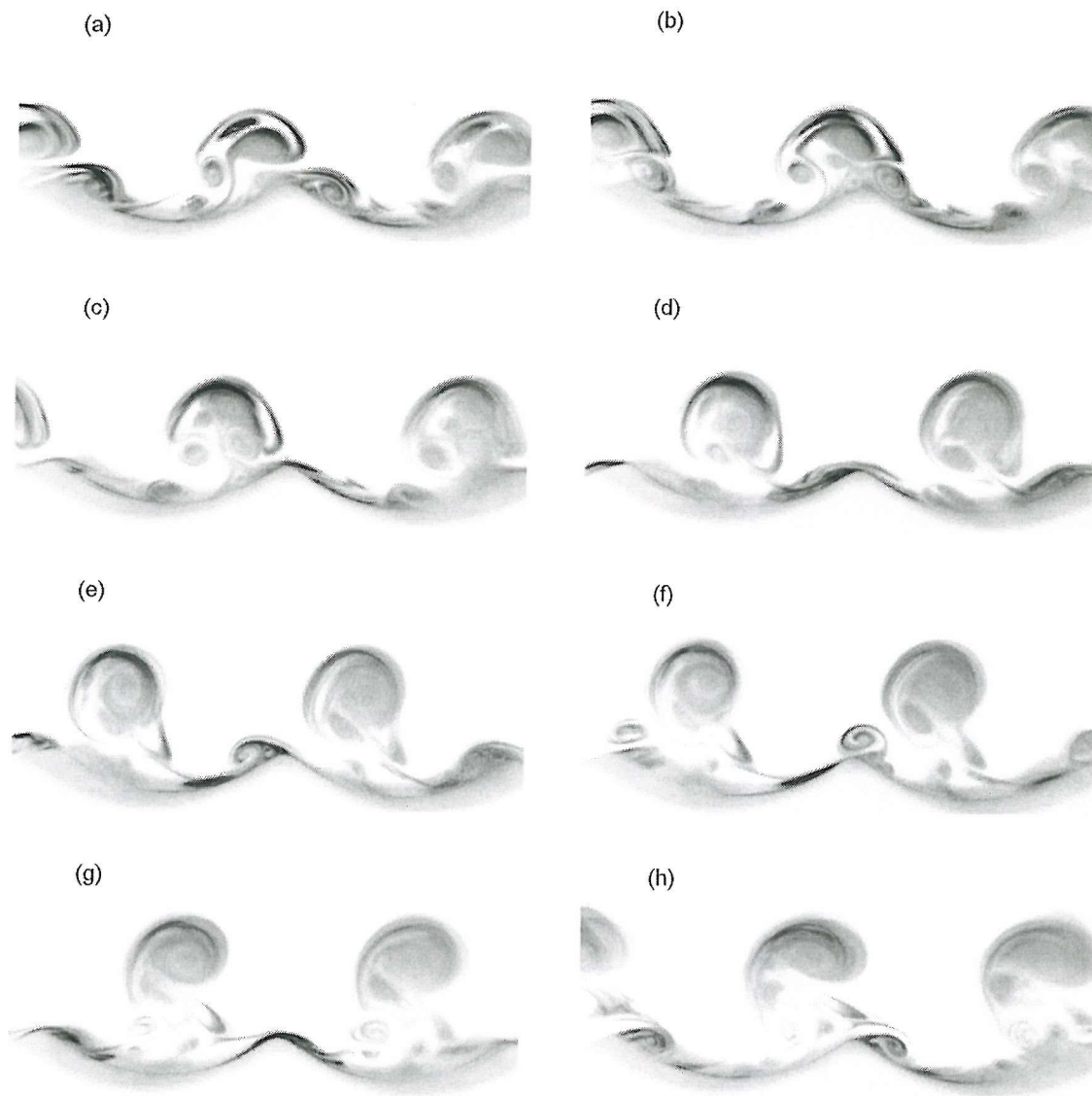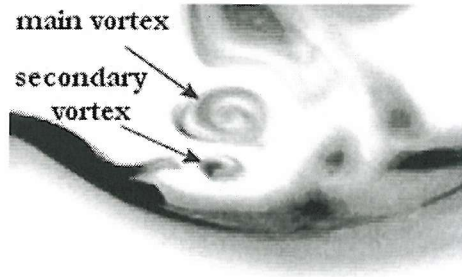
6.2.5 Discussion on the regimes

Regimes summary

Four flow regimes have been shown in the previous sections, all based on the visualizations of the flow patterns from the side of the wave flume. However the choice of separating one flow type to another might remain rather subjective, the present classification attempted to distinguish each different flow mechanism observed, possibly relevant to ripple formation and evolution. As a result, some of the flow aspects may be similar from one regime to another. For these four regimes, the main mechanisms and effects are:

- the regime with "roll" or cell structures is a stable regime where the ripples will probably build very slowly, facing no major change in shape. A steady streaming process is shown in the form of recirculation cells and no flow separation is present. The sediment transport can be assumed as being weak. This regime may correspond to the conditions for which rolling-grain ripples develop.

- the regime with "roll" plus jet structures will probably involve some significant sediment transport as the jets will drag some particles upward and release them later. The main effect is probably a slow building of the ripples, until they reach the maximum steepness for a given flow condition and a given grain size, and then oscillate around an equilibrium state. The steady streaming cells are still present but disturbed by the jet structures. The jet instability always appears first at the lee-side of the ripple slope, during the flow reversal.

- the flow separation regime is the transitional regime where flow separation first occurs. It features vortex structures nearly ejected from the crest being eventually dragged upward by the jets. It probably involves more sediment transport than in the previous regime, as the small vortices may be more effective at trapping sediment than the jets. But as the vortices are not really ejected but carried away

131

by the jets, the trapped sediment once dragged upward is probably released in a similar way to the previous regime.

- the regime with vortex ejection is certainly the regime involving the maximum sediment transport. It is obtained when the flow oscillation is not small compared to the ripple wavelength. It contributes to the building of the ripples, giving them this particular shape with sharp crests and flat trough, legitimately called vortex ripples. For several cases, when the flow is in the same direction as the wave propagation, the ejected vortex has a coupled vortex below its structure, counter rotating and smaller than the main vortex. It also turns out that when the flow is in the same direction as the wave propagation, the vortex is ejected along a horizontal path, but in the case of an opposite flow direction, the ejected vortex moves more upward, following the ripple slope plan.

What happens when the flow oscillation gets even stronger and significant turbulence occurs cannot be discussed here, as the experiments in such a case were limited by the technique of visualization. It can only be assumed that as the flow velocity increases, the size and strength of the vortices will also increase as well as their lifespan, so that they will probably interact with each other covering the entire ripple length leading to the presence of turbulence everywhere and probably at all times. For further analysis on this regime, see references cited in section 2.5.4.

A final remark that applies to all the regimes can be made: the curvature of the boundary seems to influence the shape and size of the structures, cells or vortices. The steeper the slope and therefore the more curved the boundary[6], the rounder the structures will be. On the other hand, for a weak ripple slope or weak curvature of the boundary, the structure will be more flat and usually smaller (figure 6.11).

---

[6]See formulas (5.1) and (5.2) in section 5.1.

Taylor number

It is recalled that the Taylor number is used to measure the importance of the centrifugal effects with respect to the viscous ones. The range for the ratio T_a/r for with each regime has been observed can be seen in figure 6.28. The regimes are difficult to categorize as all the parameters seem to play an important role. However, the ratio T_a/r seems to be a relevant parameter for this classification, as shown in figure 6.29.
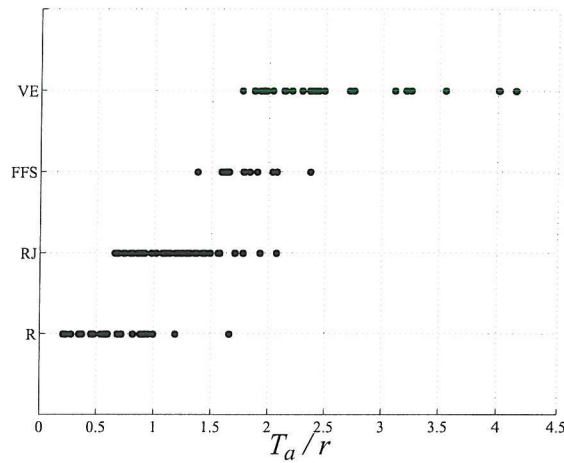
Figure 6.28: Two-dimensional regimes range for the Ratio T_a/r. R: roll patterns regime; RJ: roll + jet patterns regime; FFS: first flow separation regime; VE: vortex ejection regime.

Visualization limits

When the flow oscillation was large, observation had to be done quickly after reaching the expected flow conditions. Therefore, for these flows it was not possible to be certain of the stability of the flow mechanism, or in other words, whether or not it was repeating itself for a large number of wave periods. For the most stable conditions (first and second regimes), the dye patterns were covering the entire rippled section for as long as the waves were generated, as shown in figure 6.30.
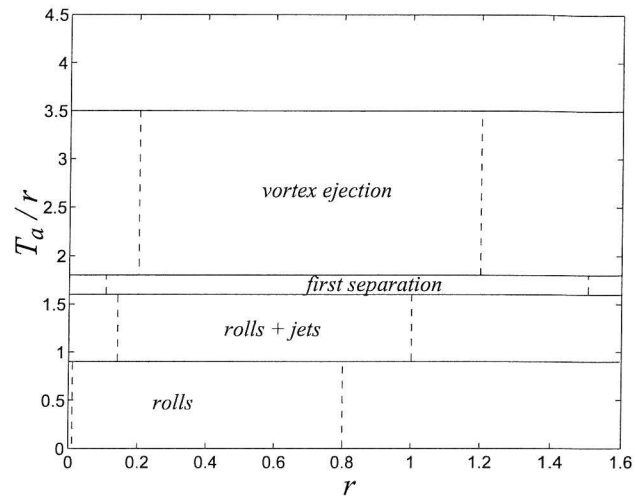
Figure 6.29: Two-dimensional regimes summary. The area above the upper limit of the vortex ejection area could not be studied due to the presence of turbulence limiting the experimental visualizations. The dashed lines shows the range in r for which each regime was obtained. The horizontal lines are for visual help and are arbitrary.

Figure 6.30: Cells plus jets regime; $s_r = 0.175$; $r = 0.14$; $T_a = 0.17$.

6.3 Three-dimensional instabilities

The flow classification detailed in section 6.2 is derived from two-dimensional visualizations obtained by filming from the side of the wave flume. By repeating the same experiments and filming from the top of the flume, above the rippled section, it was possible to have a three-dimensional view of the patterns, combining pictures taken from the side of the tank and from above. During the experiments, the dye patterns presented clear two-dimensional and three-dimensional structures depending on the flow and the ripple characteristics. By combining the different regime characteristics detailed in the previous section 6.2 with the three-dimensional aspects of the flow, detailed in the following sections, a more complete description of the flow above ripples can be obtained.

6.3.1 Two-dimensional flow patterns

Figure 6.31 shows a typical pattern of the two-dimensional flow usually observed. It corresponds to the most stable case discussed in section 6.2.1, where only "roll" structures are present above each ripple crest. The dye is regularly spread crosswise but the dye concentration is greater above the ripple crests due to the cell structures. Figure 6.32 corresponds to a weakly unstable case where jets of dye add to the "roll" structures showed in section 6.2.2. The streaks correspond to the small jets but viewed from above. The jet process is then purely two-dimensional. This kind of pattern is always obtained as long as the flow stays two-dimensional, the streaks being more or less visible depending on the strength of the jets. About 95% of the experimental cases where cells or cells plus jets structures were obtained showed two-dimensional structures from above. The structures stay two-dimensional for $T_a/r < 1.6$, as shown in figure 6.33. It corresponds to the upper limit of the regime featuring cells plus jet patterns described in section 6.2. It can then be concluded that the regimes featuring cells and cells plus jets are two-dimensional.

135
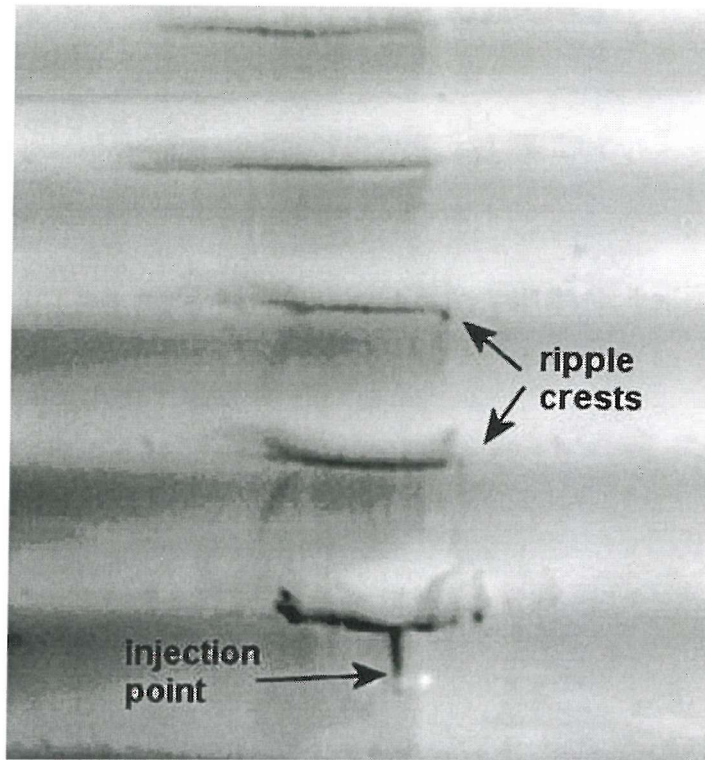
Figure 6.31: Two-dimensional dye patterns viewed from above the rippled section for a roll structure case; ripple slope $s_r = 0.05$; $r = 0.27$; $\beta = 2109$.
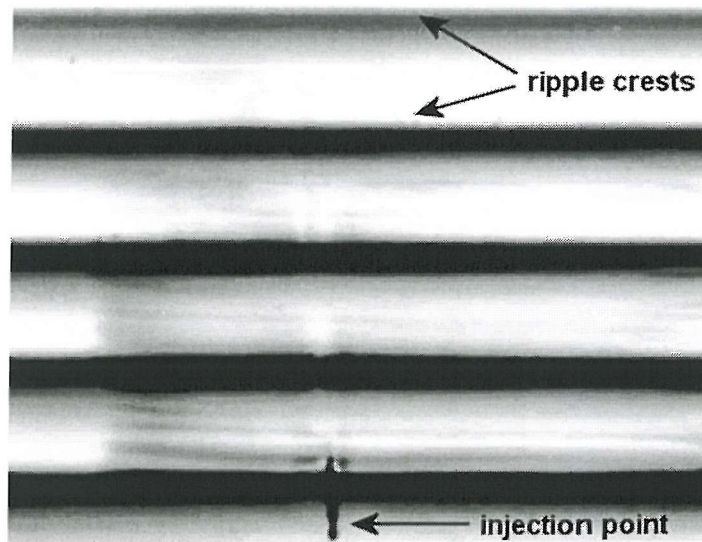
Figure 6.32: Two-dimensional dye patterns viewed from above the rippled section for a roll plus jet structure case; ripple slope $s_r = 0.12$; $r = 0.3$; $\beta = 79.2$.
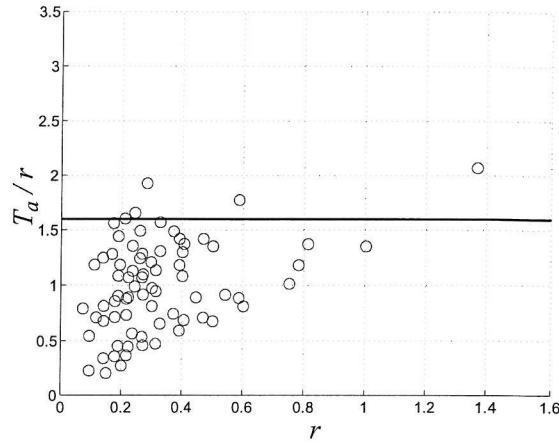
Figure 6.33: T_a/r range for two-dimensional flows. The horizontal line is for visual help and is arbitrary.

6.3.2   Two types of three-dimensional flow patterns

From a two-dimensional flow pattern the flow can break into three-dimensional structures. For a fixed ripple slope, increasing the wave amplitude (therefore the wave orbital amplitude) up to a certain point will always lead to three-dimensional instabilities. The wave period can also influence the type of instability obtained. The three-dimensional patterns can be divided in two types: a "ring" type and a brick-pattern type. Viewed from above, the brick-pattern type appears as a structure of regularly spaced bridges of dye, perpendicularly aligned to the ripple crest. The bridges starting from adjacent ripple crests are shifted by approximately half of the instability wavelength. The "rings" are equally spaced bridges of dye perpendicular to the ripple crest and regularly displaced from a ripple crest to the next.

Ring patterns

This pattern was the most common one observed during the experiments when three-dimensional instabilities were triggered. Among the three-dimensional pattern cases, ring patterns represented 70% of the experimental cases. About 67% of the cases

137

presenting ring patterns were categorized in the regime where the flow first separates and in the vortex ejection regime (sections 6.2.3 and 6.2.4). A typical ring pattern is shown in figure 6.34. As showed in figure 6.35, these structures were mainly observed
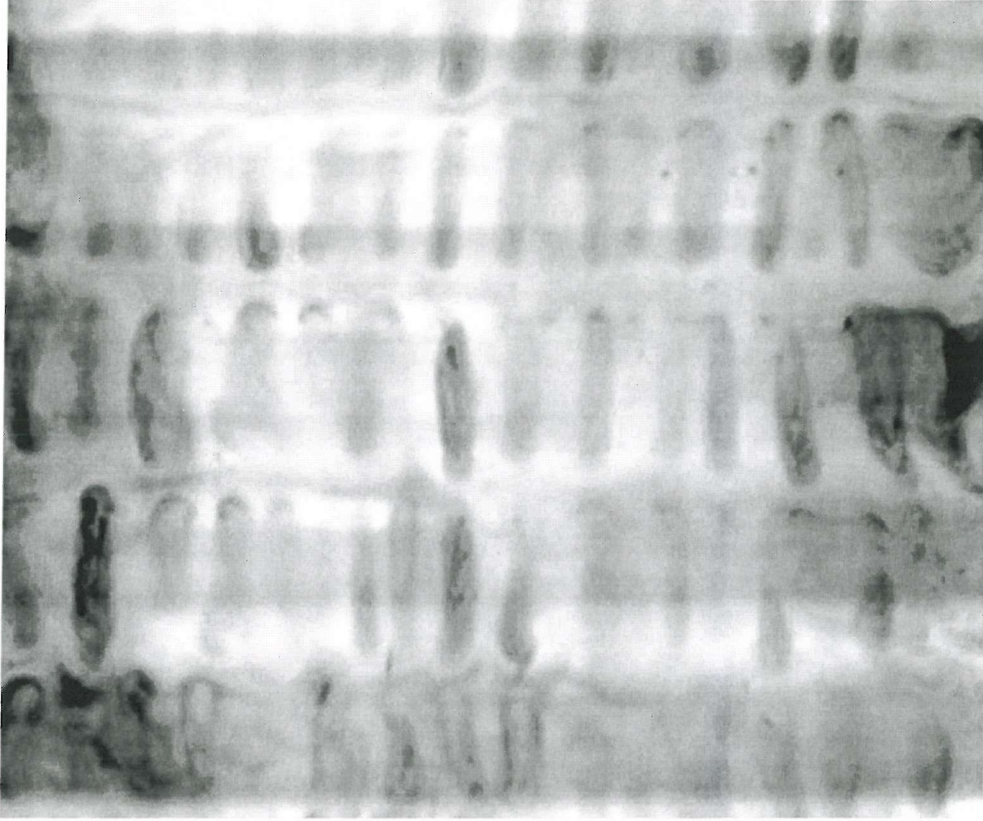
Figure 6.34: Three-dimensional ring pattern; ripple slope $s_r = 0.175$; $r = 0.15$; $\beta = 32.7$.

for $1.6 < T_a/r < 3.5$. This range is similar to the one found for the regime where flow first separates and for the vortex ejection regime if their range are put together. It then turns out from the experiments that the vortex ejection regime is three-dimensional.

An early stage of the rings formation is shown in figure 6.36, where the picture was taken immediately after the flow had reached the given characteristics. The flow
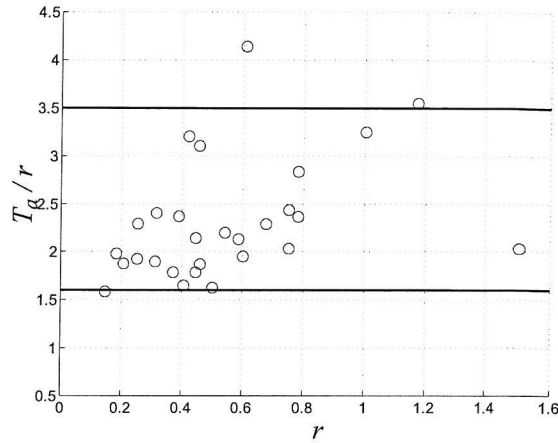
Figure 6.35: T_a/r with respect to r for which "rings" are observed. The horizontal line is for visual help and is arbitrary.

is then probably not completely established to the given orbital amplitude[7], but the purpose of this picture is to show the transition pattern between a two-dimensional flow (figure 6.32) and a ring pattern flow (figure 6.34). In this case, once the flow was established with its given characteristics, a ring pattern similar to figure 6.34 was obtained. The longitudinal streaks of dye are subject to an apparent oscillation in the crosswise direction. The amplitude of oscillation will grow, leading to the formation of separated "rings". Figure 6.37 is another example of the early stage of ring formation, with some ring structures already quite visible.

For a strong $r = 0.8$, the rings tend to get disorganized and the dye vanishes quickly. It can be supposed that bursts of turbulence cause the dye to dilute very quickly, leading to this unstable and blur pattern, as shown in figure 6.38.

The rings are usually visible for a few wave periods. If the flow oscillation is not too important, the rings will stay visible for about 5 to 10 wave periods but if the oscillation amplitude is large, the dye will be quickly diluted leaving a cloud with no apparent typical shape in less than 3 wave periods. It is then difficult to tell if this

---

[7]See section 5.3 for the wave-maker set-up.

139
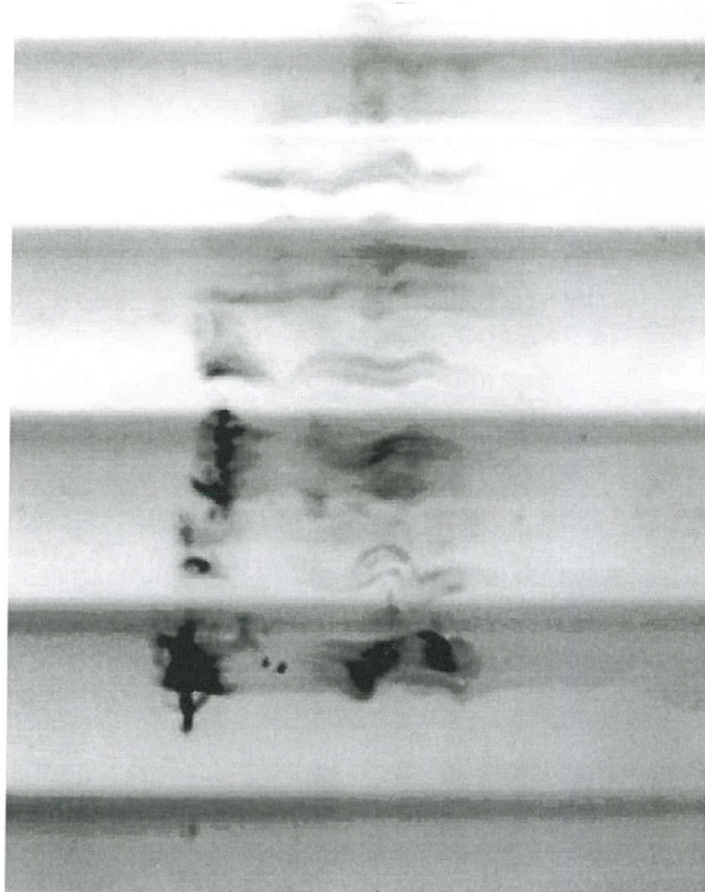
Figure 6.36: Early stage of the formation of ring pattern; ripple slope $s_r = 0.175$; $r = 0.25$; $\beta = 16.4$.

structure is stable in time.

The ratio of "ring" instability wavelength λ_i to ripple wavelength l_r was measured using all the ring cases observed. The quantity $\lambda_i/(rl_r) = \lambda_i/a_0$ is plotted against the Taylor number in figure 6.39. It appears that a simple relation such as

$$\frac{\lambda_i}{a_0} \approx \frac{1}{T_a} \tag{6.5}$$

can describe the experimental data behaviour, at least for the range of wave conditions
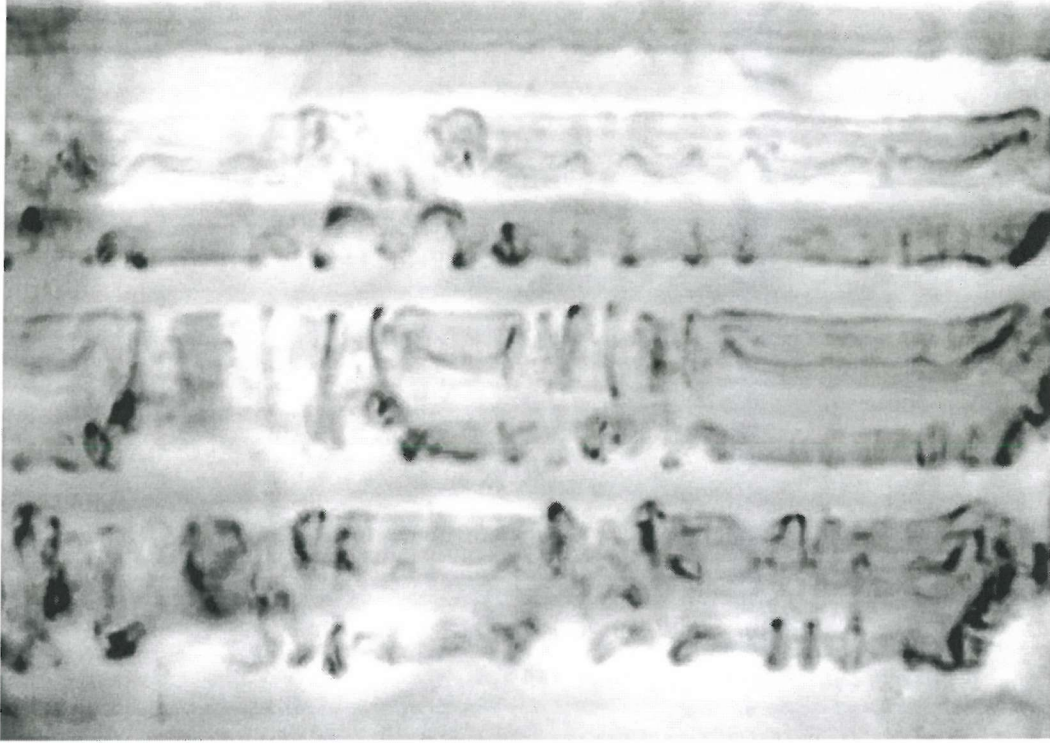
Figure 6.37: Early stage of the formation of ring pattern; ripple slope $s_r = 0.175$; $r = 0.18$; $\beta = 32.7$.

tested. Relation (6.5) is equivalent to:

$$\frac{\lambda_i}{\delta} \approx \frac{\sqrt{2}}{r s_r} \tag{6.6}$$
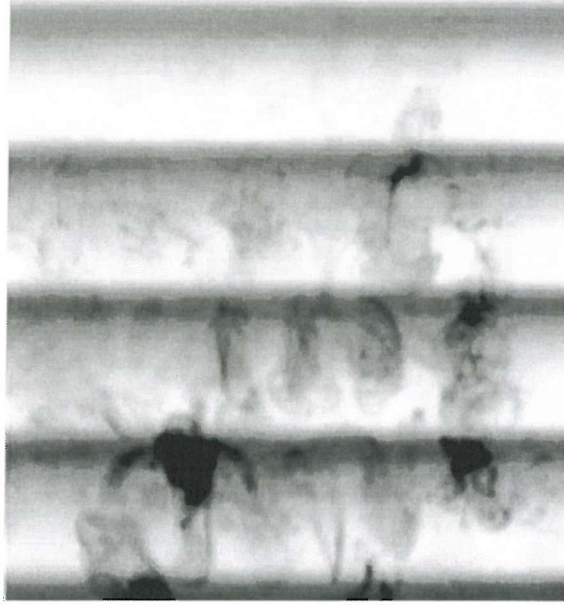
Figure 6.38: Ring pattern vanishing in semi-turbulent regime; ripple slope $s_r = 0.12$;
$r = 0.78$; $\beta = 63.4$.
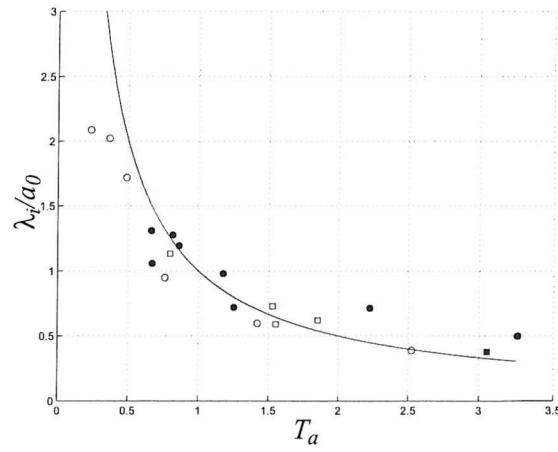
Figure 6.39: Ratio of "ring" instability wavelength λ_i to wave orbital amplitude a_0.
Experimental data: $\circ$ $s_r = 0.175$; $\bullet$ $s_r = 0.12$; $\square$ $s_r = 0.1$; $\blacksquare$ $s_r = 0.05$. The fitting
curve is $f(T_a) = 1/T_a$.

Brick pattern

A very particular type of three-dimensional instabilities has been observed. It represented 15% of the three-dimensional cases obtained experimentally. This regime has been particularly difficult to obtain during the experiments and did not stay stable very long. It differs from the ring regime because the bridges of dye are shifted from one crest to the next by approximately half the instability wavelength. Figure 6.40 shows the Taylor number range for which the brick pattern was obtained during the experiments. It seems that the brick-pattern is likely to happen for $1.5 < T_a/r < 1.85$. The upper limit slightly overlaps the lower limit of the ring pattern range. The lower limit is close to the lower limit found for the regime where flow first separates. Compared to the Taylor number ranges found for the regimes detailed in section 6.2, it seems that brick pattern is most likely to happen for the regime where flow first separates.
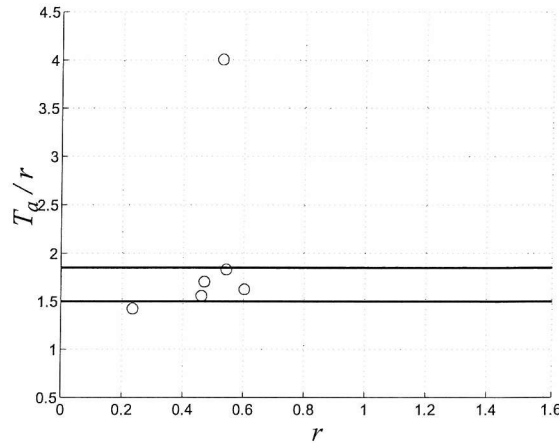
Figure 6.40: T_a/r range for which brick pattern is observed. The horizontal lines are for visual help and are arbitrary.

Figure 6.41 shows the shifted bridges from crest to crest. Figure 6.42 is another example, obtained for exactly the same flow and ripple characteristics but during another test. The dye is not spread very far crosswise, giving only two bridges after the

143

dye release point. As a result, only one bridge is present across the next ripple and two bridges across the ripple after. Figure 6.43 shows another brick pattern widely spread across the ripples. This pattern has been obtained for all the available ripple slopes except for the weakest slope $s_r = 0.05$. Table 6.1 is a summary of the flow and ripple features for which the brick pattern was observed during the experiments. The mean value for r is 0.47 and no brick pattern was obtained for $\beta > 164.1$. The range for the ratio of the brick-pattern bridge wavelength λ_b to ripple wavelength l_r can be seen in table 6.1. Mainly due to the lack of experimental cases, no obvious relation has been found between λ_b and the other parameters.

Ripple slope	T (s)	β	r	Taylor number	λ_b/l_r
0.175	3.13	10.45	0.23	0.33	0.90
0.175	2	16.4	0.52	2.11	1.325
0.12	2.5	63.4	0.47	0.8	0.8
0.1	3.13	104.9	0.6	0.98	1.03
0.1	2	164.1	0.46	0.71	0.75
0.1	2	164.1	0.54	0.99	0.66

Table 6.1: Ripple and flow characteristics for which brick pattern was obtained.

Figure 6.41: Brick pattern; ripple slope $s_r = 0.175$; $r = 0.23$; $\beta = 10.45$.

Figure 6.42: Brick pattern; ripple slope $s_r = 0.175$; $r = 0.23$; $\beta = 10.45$.
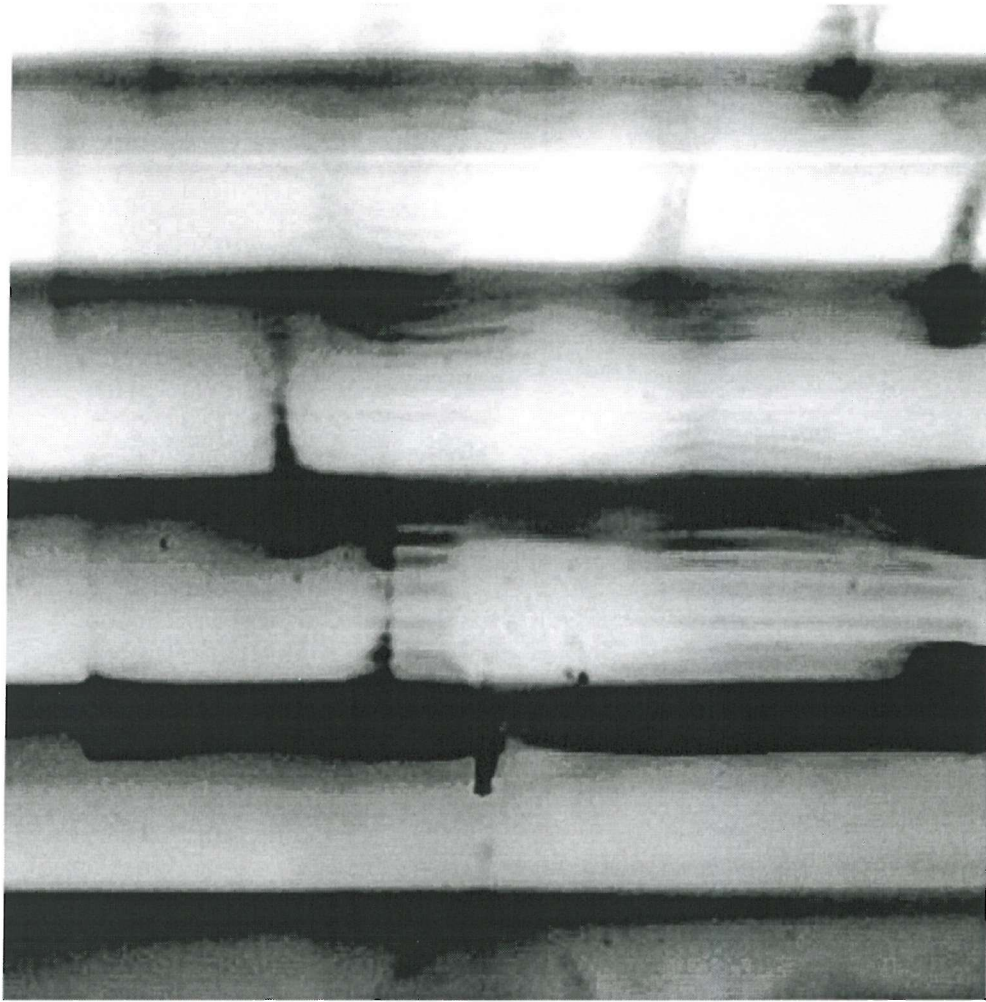
Figure 6.43: Brick pattern; ripple slope $s_r = 0.175$; $r = 0.52$; $\beta = 16.4$.

6.3.3 Comparisons with other authors' work

Scandura et al.(2000)

Hara and Mei (1990a) and Scandura et al. (2000) studied the oscillatory flow and the growth of vortices above ripples by means of numerical simulations. Their results are compared to the present experimental results in figure 6.44. Stable, unstable and marginal two-dimensional flows are plotted for a fixed ripple slope $s_r = 0.12$. Scandura et al. denote as unstable each flow solved by their model that presented transverse perturbations. According to them the marginal, stable and unstable definitions should however be treated with caution. The perturbation growth or decay was measured by looking at time evolution of energy at a specific wavelength. It turned out that in some cases it was difficult to discriminate stable from unstable flows. In figure 6.44 the horizontal axis is the Reynolds number while the vertical axis is $1/l$, with l as the dimensionless ripple wavelength $l = l_r \sigma / u_0$. Following Hara and Mei (1990b), stable and unstable regions are identified on the plane $(Re, 1/l)$. The present experimental data are shown as unstable when there was any sign of three-dimensional structures. These data points are located in the same area as the unstable flow obtained by Scandura et al. But the observations of stable flows were generally at Reynolds numbers smaller than for the cases obtained by Scandura et al. (2000). The experimental conditions cannot offer such a wide variety of cases as a numerical model does, therefore some areas in the graph could not be covered by the experimental data. Scandura et al. also noticed that for the case of a strong oscillatory flow over steep ripples, the action of a vortex structure created by the boundary layer separation and the vorticity roll-up would tend to create a jet directed upward lifting up particles. This jet is located in the centre of their computational box. It is different from the jets visualized in figure 6.32 section 6.3.1 as it is not happening across the whole width of the domain, but this process might involve a similar mechanism. They also noted that when r is of order 1 the flow separation has a destabilizing effect, making the flow become more
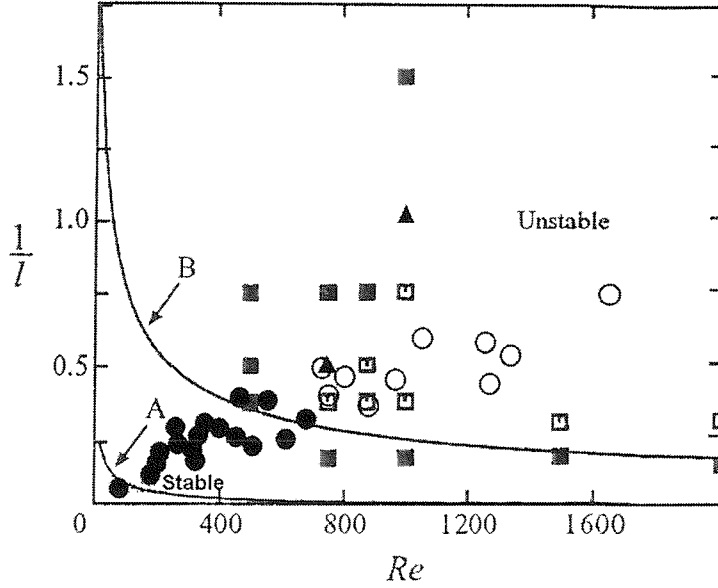
Figure 6.44: Scandura et al.(2000) results: stable ■, unstable □ and marginal ▲ 2D flows. Curve A has been derived from Hara and Mei (1990) for large values of l, curve B is a heuristic adaptation of curve A. Experimental results: stable ●, unstable ○ and marginal ⊙ 2D flows. l is the dimensionless ripple wavelength: $l = l_r \sigma / u_0$.

three-dimensional. The present experiments give good agreement with this remark as when the flow separation was observed, the flow was three-dimensional for most of the cases.

Hara and Mei (1990b)

In their numerical analysis Hara and Mei (1990b) found that for a gentle ripple slope $s_r \ll 1$ and for $r = 0.64$, an accumulation pattern indicating the formation of bridges between the transverse crests might lead to the brick-patterned ripples. According to Hara and Mei, centrifugal instabilities as well as vortex shedding must be effective in the initiation of the brick pattern. In the present experiment, the weakest slope is $s_r = 0.05$, and no brick pattern was observed using these ripples, but vortex shedding

149

was also very difficult to obtain. The absence of any brick pattern for the whole range of flow conditions might then be explained by the difficulty to obtain vortex shedding, and therefore three-dimensional flows, above such a weak ripple slope. However, Hara and Mei also concluded that the centrifugal instability threshold was for a Taylor number of order one (section 2.6.3). In the present experiments, if the mean value of T_a for which brick-pattern was observed is calculated, a value of 0.98 is found, which is in good agreement with Hara and Mei's results.

Sleath and Ellis (1978).

In Sleath and Ellis (1978), sand ripples were formed on a tray of sediment oscillating in a tank of still water. Brick patterns were obtained and the flow and ripple characteristics were recorded. Table 6.2 compares the results from Sleath and Ellis and the present experimental flow and ripple characteristics for which the brick pattern was obtained. The comparison is a qualitative one, since the experiments conducted by Sleath and Ellis are very different from the present ones. However, in the present experiments when the dye shows an obvious brick pattern structure, it can be assumed that the flow and ripple conditions would lead to brick pattern ripples if the bed was movable. There is good agreement on the range for which the brick pattern was obtained, even

Sleath and Ellis (1978)	Present experiments
$0.15 < s_r < 0.27$	$0.1 < s_r < 0.175$
$0.55 < r < 0.88$	$0.24 < r < 0.6$
$0.015 < \delta/l_r < 0.049$	$0.016 < \delta/l_r < 0.026$

Table 6.2: Comparison between Sleath and Ellis (1978) and the present experiments on the ripple and flow characteristics for which brick pattern was obtained.

though it seems that Sleath and Ellis also obtained brick patterns for stronger r and stronger ripple slopes. It shows that these particular dye patterns are connected to the

building process of brick pattern ripples for a sand bed. The three-dimensional vortices can be assumed to be the main cause in the formation of brick pattern ripples.

6.4 Discussion

From the experimental analysis of the flow above ripples by means of dye injection, the following results can be stated:

- For $T_a/r < 0.9$ the flow is mostly two-dimensional, presenting steady streaming recirculation cells on each crest.

- In two-dimensional flows a jet process can be present occurring at the lee-side of the ripple, for $0.9 < T_a/r < 1.6$. This process needs to be studied further.

- For $T_a/r > 1.6$, the flow is likely to separate and feature a vortex ejection at each half wave cycle. This flow is also likely to feature three-dimensional instabilities.

- The three-dimensional "ring" structure was the most common three-dimensional structure observed during the experiments for varied flows. It features flow separation, vortex formation and possible ejection.

- The three-dimensional brick pattern was not frequently observed during these experiments and was not very stable in time. It also features flow separation, but the vortex ejection process is not obvious.

- The ratio of "ring" instability wavelength to wave orbital amplitude λ_i/a_0 has been experimentally found behaving as the recipical of the Taylor number.

- The ratio of the brick-pattern bridge wavelength to ripple wavelength λ_b/l_r is in the range 0.6 to 1.3, while the ratio of "ring" instability wavelength to ripple wavelength λ_i/l_r is in the range 0.24 to 0.64.

- The brick pattern ripples are caused by three-dimensional vortices featuring a structure similar to the brick pattern.

- The vortex and the cell shapes are influenced by the curvature of the boundary; usually the steeper the slope, the larger the structures. But also for longer wave periods, the structures will be larger, having more time to grow.

A diagram giving a complete summary of the flow characteristics observed for the tested experimental conditions is shown in figure 6.45. Table 6.3 is a summary of all the relevant information on the flow characteristics recorded during the experiments.

T_a/r	side observations	flow dimension
up to 0.9	cells	2D flow
0.9 to 1.6	cells + jets	2D flow
1.6 to 1.8	flow separation	3D flow (BP likely)
1.8 to 3.5	flow separation + vortex ejection	3D flow (rings)

Table 6.3: Summary of the experimental visualizations; BP: Brick pattern; T_a: Taylor number; r: orbital amplitude to ripple wavelength ratio.
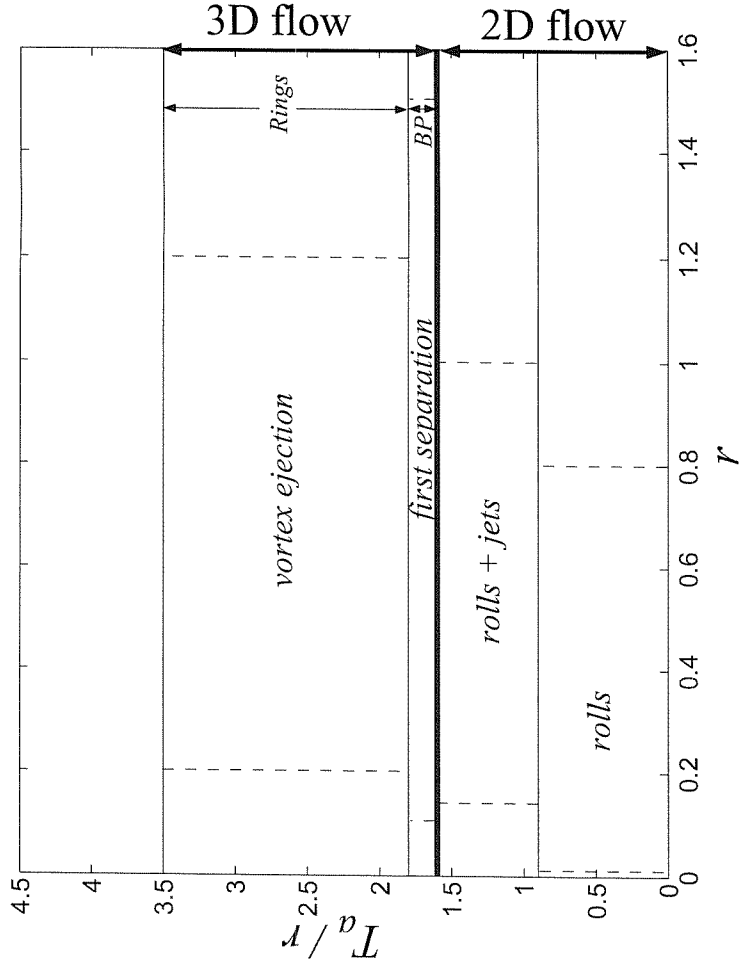
Figure 6.45: Flow characteristics summary. The thicker line shows the separation between 2D and 3D flows. BP: area where 3D brick patterns were observed. Rings: area where 3D ring structures were observed. The area above the upper limit of the vortex ejection area could not be studied due to the presence of turbulence limiting the experimental visualizations. The dashed lines show the range in r for which each regime was obtained. Areas outside the dashed lines domain could not be studied due to the appearance of turbulence limiting the visualizations. The horizontal thin lines are for visual help and are arbitrary.

Chapter 7

Conclusion

A review of previous work on flow over ripples revealed that many areas of study are still incomplete and further experimental and numerical investigations need to be done. This thesis describes work aimed at improving understanding of this flow.

Experiments have been conducted in a wave flume fitted with a fixed rippled bed. The wave-induced flow above the ripples was visualized by means of dye injection for a wide range of flow and ripple conditions. Remarkable flow patterns were observed such as recirculation cells, jets and vortices. A new classification of the flow structures has been obtained, in terms of appropriate parameters relevant to the flow and ripple conditions, providing valuable information on the flow characteristics. These parameters are the ripple slope, the wave orbital amplitude to ripple wavelength ratio and the Taylor number. Figure 6.45 (section 6.4) shows the classification obtained, identifying the type of flow pattern observed and the onset of three-dimensional motion.

The flow visualizations above solid ripples showed the extraordinary variety of flow regimes and structures that could take place close to the bed in various flow and ripple conditions. It can be supposed that for other flow conditions (larger flow oscillations, larger wave periods) that have not been represented in this study, some other regimes could be obtained. The present study mainly considered the cases for which the flow oscillation at the bed was of the same order as the ripple wavelength, as it is acknowl-

edged to happen frequently in shallow coastal areas.

The development of a two-dimensional computer model solving the flow in the vicinity of a flat or rippled bed also helped in understanding the key features of the flow process and provided some opportunity to study further some particular aspects of this flow such as the mean Eulerian velocity, the mass transport velocity and the vortex ejection process. The predictions of the model were in good agreement with other numerical and experimental sources when the main characteristics of the flow dynamics were studied. By comparing the model to the theory available for the case of wave-induced flows above a flat bed, discrepancies have been found on the consistency of the theoretical solutions.

Future work

Using the results provided in this thesis, further investigations could be done on different subjects.

The flow velocity above the ripples in a wave flume could be recorded by Particle Image Velocimetry (PIV) or Laser Doppler Anemometry (LDA), using flow conditions and ripple characteristics similar to the present experiments. These velocity data would help in understanding the dye patterns observed and could also provide a valuable input for the present model. Furthermore, obtaining the experimental velocity fields for the regime where circulations cells were observed might make this aspect of the flow clearer, particularly for wave flume experiments where the flow features a mean drift velocity. Their presence for the case of an oscillatory water tunnel is proven, as numerous theoretical analyses agreed. It would then be interesting to understand if the cells visualized in the present experiments are really part of the same mechanism; if it is the case, it would then be worth studying the process leading to the change in their structure.

The jet process revealed by the experiments needs to be studied further to understand the cause of this instability and its effect on the suspended sediment transport.

This study could also make use of PIV or LDA measurements.

Applying the same wave conditions to a movable bed with already formed ripples, especially when three-dimensional structures have been observed, would be the next step to improve knowledge on the ripple evolution from a two-dimensional to a three-dimensional pattern. Starting the experiments with two-dimensional formed ripples and applying flow conditions believed to lead to three-dimensional ripples would be possible using the results provided in the present thesis.

The development of a fully three-dimensional model solving the wave-induced flow over ripples remains a priority. The vortex ejection process, revealed by the visualizations to feature three-dimensional instabilities and believed to be a major factor in the sediment transport mechanism, would then be described more accurately.

Finally, the numerical model has been modified and enhanced, with the aim of calculating the trajectory of marked particles to allow direct comparison with the flow visualizations (appendix B). But this new model is still in development and few validated results could be shown in the present thesis. The methodology can be found in appendix B, as well as a comparison of predicted and observed particle trajectories.

Appendix A

Experiments on ripple enhancement

Some experiments have been conducted to illustrate one aspect of the ripple building process using the information given on sea bed ripple characteristics in section 2.7. The ripples used in the wave flume are fixed. However, by randomly releasing some sediment on the wavy bed, it is reasonable to assume that a part of the building process of the ripples described in section 2.7.1 could be observed. The ripples with the smallest slope available is used so that the flow conditions for which ripples should be building are easy to reach. The sediment used is bakelite of relative density 1.45 and diameter $d_{50} = 0.515mm$, where d_{50} is the particle diameter for which 50% of the particles will have a smaller diameter. If formula (2.41) is used with the corresponding values for the mobility number Ψ and for the range of possible wave periods and wave amplitudes in the wave flume, it is found that the actual ripple height is smaller than predicted for the majority of possible orbital amplitudes obtained in the present experiments[1], as shown in figure A.1. Therefore, by randomly distributing particles along the bed in water at rest and then by running waves of large enough amplitudes, an accumulation pattern on the ripple crests should happen as predicted by theory. Formulas (2.38) and (2.39) are used to calculate the orbital amplitudes corresponding to a fixed ripple wavelength, for the experimental range of wave periods. It can be assumed that for

---

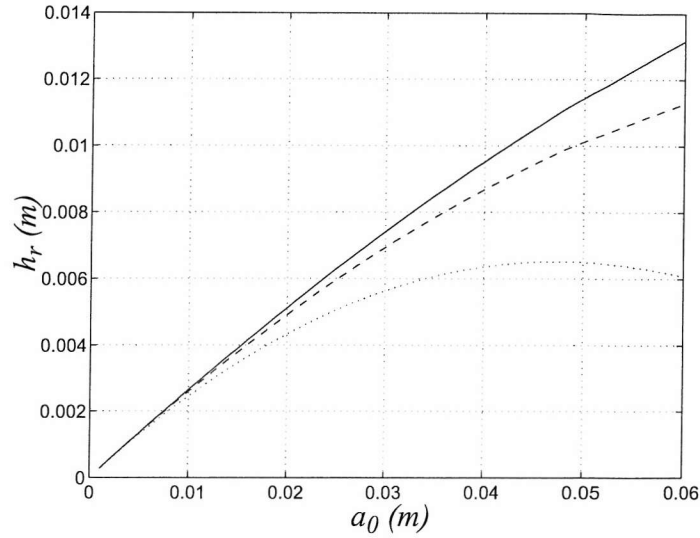[1]For the present experiments, the wave orbital amplitude range is 3.8 $mm < a_0 < 60$ mm.

Figure A.1: Ripple height predicted by formula (2.41) for a fixed ripple wavelength of 0.04 m. (-) T=3.13 s; (- -) T=2s; (..) T=1s. The ripple height is fixed and equal to 0.002 m.

orbital amplitudes larger than the limit set by formulas (2.38) and (2.39), for a fixed wave period, the sediment should tend to accumulate on the crests, enhancing the ripple height. The bakelite movement is observed and plotted in figure A.2, for different Reynolds numbers and wave periods. For large enough orbital amplitude values, or in other words for Reynolds numbers over the curves derived from formulas (2.38) and (2.39), an accumulation of the sediment on the ripple crests is observed, giving good agreement with the predictions. It appears that agreement is especially good for the longest wave periods tested. Figure A.3 is a perspective view of the ripples, showing a random distribution of bakelite on the rippled surface. After several waves of a fixed period and an orbital amplitude large enough to induce movement (figure A.2), the bakelite is transported and accumulates around the ripple crests, as shown in figure A.4. The lines of sediment will then oscillate around the crests, explaining why the sediment is slightly shifted on the lee-side of the crests in figure A.4, as the picture has
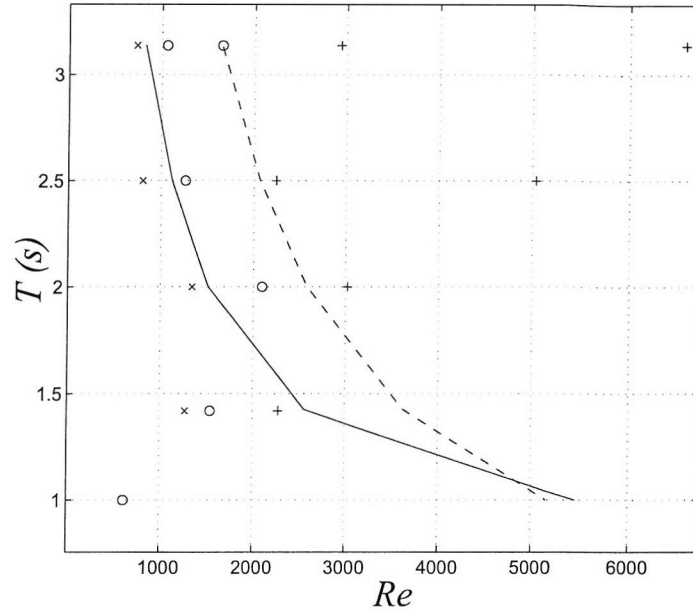
Figure A.2: Formula 2.38 (- -); Formula 2.39 (-) expressed in terms of Reynolds number for the experimental range of wave period and for a fixed ripple wavelength of 0.04 m. Observation of the bakelite movements: × no movement; o the lightest particles are moving; + all the particles are moving.

been taken just before flow reversal. This test partly demonstrates that for a sufficient enough wave orbital amplitude, the present ripples would tend to build up. These results are only qualitative and have to be taken with caution, as the experimental set-up remains different from reality. The bottom being fixed no real erosion in the ripple troughs can be shown, but it has been observed that the bakelite particles randomly distributed are dragged to the crests.
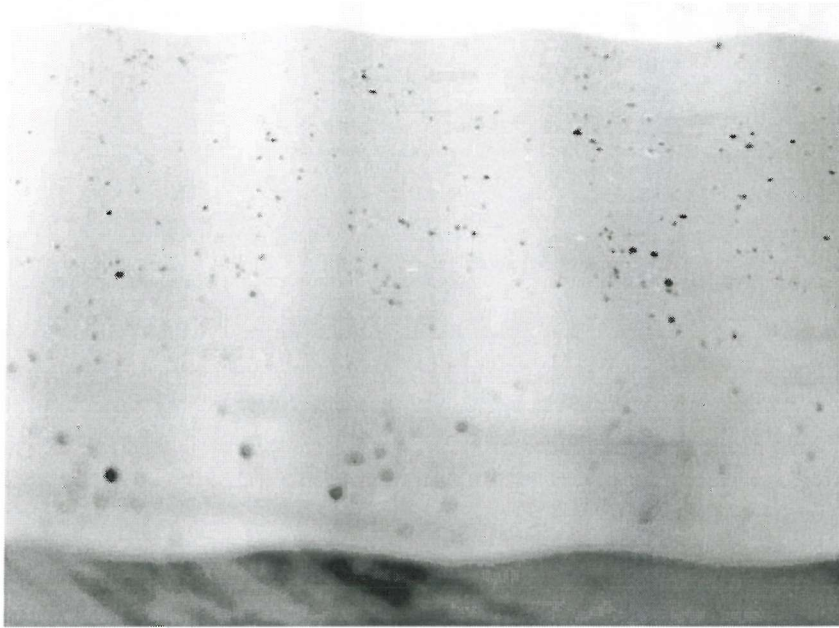
Figure A.3: Picture of the ripples with a random distribution of bakelite. Ripple wavelength: 0.04 m; ripple height: 0.002 m.
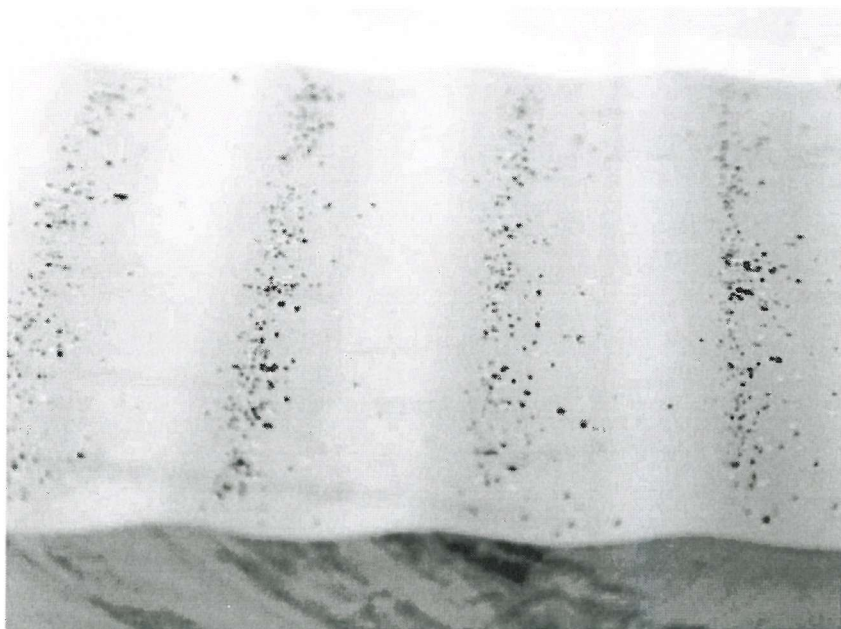
Figure A.4: Picture of the ripples after several waves. The bakelite particles are aligned and oscillate around the crests; $T = 3.13s$; $r = 0.8$; $Re = 3019$.

Appendix B

Trajectory model

An attempt to extend the use of the computer model presented in chapters 3 and 4 has been made to enable direct comparisons to be done with the experimental visualizations. The velocity model output is used to calculate the trajectories of marked particles released steadily from the ripple trough very close to the bed, in a similar way to the experimental set-up.

B.1 General algorithm

The trajectory model uses the velocity files output by the previous model run first for given conditions (ripple wavelength, ripple height, wave orbital amplitude and wave period).

- At each time step, a few particles are introduced above the trough. The time-step Δt is the same as the time step used in the first model.

- the positions of the particles previously introduced are then updated and their former position is deleted.

- the particle position update uses a fourth order Runge-Kutta integration.

B.2 Particle position update

B.2.1 Runge-Kutta method

If u^p and v^p are the horizontal and vertical velocities at the previous time-step, u^n and v^n are the new velocities calculated at the present time-step, x^p and y^p are the particle position coordinates at the previous time-step while x^n and y^n are the new position coordinates at the present time-step, the Runge-Kutta calculation is as follows.

$k1_x$ and $k1_y$ are calculated:

$$k1_x = \frac{dt}{2} u^p_{i-1,j} \quad ; \quad k1_y = \frac{dt}{2} v^p_{i-1,j} \tag{B.1}$$

The first temporary coordinates are found:

$$x^n_{i,j} = x^p_{i-1,j} + \frac{k1_x}{2} \quad ; \quad y^n_{i,j} = y^p_{i-1,j} + \frac{k1_y}{2} \tag{B.2}$$

$k2_x$ and $k2_y$ are calculated:

$$k2_x = \frac{dt}{2} u^n_{i,j} \quad ; \quad k2_y = \frac{dt}{2} v^n_{i,j} \tag{B.3}$$

The second temporary coordinates are found:

$$x^n_{i,j} = x^p_{i-1,j} + \frac{k2_x}{2} \quad ; \quad y^n_{i,j} = y^p_{i-1,j} + \frac{k2_y}{2} \tag{B.4}$$

$k3_x$ and $k3_y$ are calculated:

$$k3_x = \frac{dt}{2} u^n_{i,j} \quad ; \quad k3_y = \frac{dt}{2} v^n_{i,j} \tag{B.5}$$

The third temporary coordinates are found:

$$x^n_{i,j} = x^p_{i-1,j} + k3_x \quad ; \quad y^n_{i,j} = y^p_{i-1,j} + k3_y \tag{B.6}$$

$k4_x$ and $k4_y$ are calculated:

$$k4_x = \frac{dt}{2} u^n_{i,j} \quad ; \quad k4_y = \frac{dt}{2} v^n_{i,j} \tag{B.7}$$

The final estimation for the new coordinates can then calculated:

$$x_{i,j}^n = x_{i-1,j}^p + \frac{1}{6}(k1_x + 2k2_x + 2k3_x + k4_x) \tag{B.8}$$

$$y_{i,j}^n = y_{i-1,j}^p + \frac{1}{6}(k1_y + 2k2_y + 2k3_y + k4_y) \tag{B.9}$$

This kind of calculation faces a major problem: at any time step, the velocities needed do not systematically correspond to a grid point. Indeed, as any new particle position (x^n, y^n) found with (B.2), (B.4) or (B.6) does not correspond to a grid point, its corresponding velocities (u^n, v^n) needed for the calculations in (B.3), (B.5) or (B.7) do not exist. In order to have the velocities anywhere in the computed domain and not to be restricted to the grid points, a method divided in two steps is used. First, at a given time, for a given elevation (given j, see grid in figure 3.1), a Fourier analysis is done so that the velocity can be found anywhere along the same line of constant η, across the entire width of the domain. Second, as the velocity needed is also likely to be at a location in between two elevations, a Lagrange interpolation is done on the Fourier coefficients obtained previously, between two neighbouring and defined elevations. Then the interpolated Fourier coefficients can be used to calculated the velocities at the exact location needed.

B.2.2 Fourier transformation

For a given wave phase, the horizontal and vertical velocities are only available at the grid points. By doing a Fourier analysis of the velocity files at a given level j, u and v can be expressed as:

$$u_j = A_{0,j} + \sum_{n=1}^{nb} A_{n,j} \cos(n\theta) + B_{n,j} \sin(n\theta) \tag{B.10}$$

$$v_j = A'_{0,j} + \sum_{n=1}^{nb} A'_{n,j} \cos(n\theta) + B'_{n,j} \sin(n\theta) \tag{B.11}$$

where $\theta = \sigma t - kx$. Once the coefficients are calculated, the velocities can be found at any θ, that is at any time t and at any location along the same elevation.

B.2.3 Lagrange interpolation

A Lagrange interpolation is done for each Fourier coefficient, at intermediate levels, using five points. Any $A_{n,y}$ or $B_{n,y}$ is interpolated, for $j < y < j+1$. The formula used is:

$$f(y) \approx \frac{(p^2-1)p(p-2)}{24}f_{-2} - \frac{(p-1)(p^2-4)p}{6}f_{-1} + \frac{(p^2-1)(p^2-4)}{4}f_0$$
$$-\frac{(p+1)p(p^2-4)}{6}f_1 + \frac{(p^2-1)p(p+2)}{24}f_2 \qquad (B.12)$$

With:

- f_j standing for $A_{n,j}$ or $B_{n,j}$.
- $f(y) = f(j_0\Delta y + p\Delta y)$ is $A_{n,y}$ or $B_{n,y}$.
- $p = (y - j_0\Delta y)/\Delta y$.
- index $j = 0$ is the j level corresponding to the entire part of $y/\Delta y$. Other index values are for levels above and underneath it. $j = 1$ is the first level above the level $j = 0$ and $j = -1$ is the first level underneath it.

B.2.4 Periodicity

The particles are injected for a duration of several wave periods (typically 20 to 30), in order to get an established pattern. Indeed, the experiments in the wave tank showed that at least 10 to 20 wave periods were needed to get a complete dye pattern. The velocity files from the first model, saved for each wave phase, are used at the same relative wave phase for each wave period, assuming a repeatability of the oscillatory flow pattern. According to Marin (1992), Earnshaw and Greated (1998) and Malarkey and Davies (2002), such an approximation can induce errors in the calculation as the periodicity of particles movement can be in some cases longer than a wave period. Calculating the velocity files for several wave periods and using them directly in the particle trajectory calculation is possible but it needs too much computer time with the present model.

164

B.3 Results

No satisfactory result has been obtained so far. The particles trajectories produce the same type of pattern regardless of the wave conditions and do not offer the variety of structures visualized in the experiments. A very large number of wave periods might be needed in order to get different patterns. It would then need a lot of computer time to get complex patterns closer to the experimental flow visualizations. The model needs further optimization in order to reduce the computer time. The particle update loop with its interpolation calculations might also not be accurate enough to describe such a process. Using the same velocity files at each wave period could also be the main condition limiting the possibility to obtain any pattern observed in the experiments. A major problem can also come from the fact that the building process of the flow structures is a slow process involving weak time-mean velocities. Despite a good agreement of the model with the experiments for instantaneous velocities, the weak time-mean velocities might not be represented accurately enough by the model.

Figure B.1 shows a case of acceptable agreement between the experimental visualization and the trajectory computer model, for the case of a two-dimensional mushroom shape pattern. This kind of result is unfortunately the only type of shape produced by the model. This result has then to be treated with caution. This computed pattern can also be taken as the negative image of a pair of cells. It is recalled that the model does not include any steady component in the wave-induced velocity definition. Therefore, similarly to the results shown in section 4.3.4, the structure computed could be a kind of circulation cells pair. It is however not clear why for a large wave orbital to ripple wavelength ratio and steep ripple slope, either the same type of pattern is obtained instead of a vortex ejection pattern, or the model stops as particles would escape from the defined domain.

Further work needs to be done on this trajectory model. Improvement and optimization of this model are beyond the scope of the present thesis but should be carried out in the future.
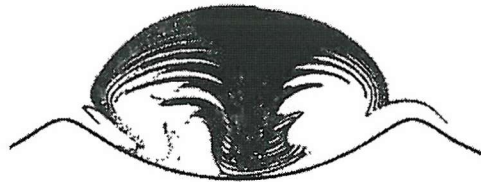
Experiments
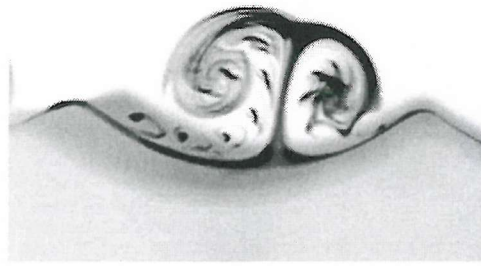
Model

Figure B.1: *Comparison trajectory model result - Experimental visualization; ripple slope $s_r = 0.175$; $r = 0.11$; $\beta = 32.7$ (wave period $T = 1$ s).*

166

List of references

Andersen, K. H. (2001). A particle model of rolling grain under waves, *Physics of fluids* **13**(1): 58–64.

Andersen, K. H. and Faraci, C. (2003). The wave plus current flow over vortex ripples at an arbitrary angle, *Coastal Eng.* **47**: 431–441.

Andersen, K. H., Chabanol, M. and VanHecke, M. (2001). Dynamical models for sand ripples beneath surface waves, *Physical Rev. E* **63**(6): 066308/1–8.

Bagnold, R. A. (1946). Motion of waves in shallow water, interaction between waves and sand bottoms, *Proc. Roy. Soc. Ser. A* **187**: 1–15.

Bakker, W. T. and Doorn, T. V. (1978). Near bottom velocities in waves with a current, *Proc. 16th Int. Conf. on Coastal Eng.* **2**(chap82): 13941413.

Beech, N. W. (1978). Laser doppler measurements in the oscillatory boundary layer beneath water waves, *DISA information* **23**: 6–10.

Blondeaux, P. and Vittori, G. (1991). Vorticity dynamics in an oscillatory flow over a rippled bed, *J. Fluid Mech.* **226**: 257–289.

Chowdhury, S. A., Sato, M. and Ueno, A. (1997). Numerical model of the turbulent wave boundary layer induced by finite amplitude water waves, *App. Ocean Res.* **19**: 201–209.

Collins, J. I. (1963). Inception of turbulence at the bed under periodic gravity waves, *J. Geophysical Res.* **68**: 6007–6014.

Cotton, M. A. and Stansby, P. K. (2000). Bed frictional characteristics in a turbulent flow driven by nonlinear waves, *Coastal Eng.* **40**: 91–117.

Davies, A. G. and Villaret, C. (1997). Oscillatory flow over rippled beds: boundary layer structure and wave-induced eulerian drift, *Adv. Fluid Mech.* **10**: 215–254.

Davies, A. G., Soulsby, R. L. and King, H. L. (1988). A numerical model of the combined wave and current bottom boundary layer, *J. Geophysical Res.* **93**(C1): 491508.

Dore, B. D. (1982). On the second approximation to mass-transport in the bottom boundary layer, *Coastal Eng.* **6**(2): 93–120.

Dyke, P. P. G. and Barstow, S. F. (1981). Wave induced mass transport: theory and experiments, *J. Hydraulic Res.* **19**(2): 89–106.

Earnshaw, H. and Greated, C. (1998). Dynamics of ripple bed vortices, *Exp. in Fluids* **25**: 265–275.

Fredsøe, J. and Deigaard, R. (1992). *Mechanics of coastal sediment transport*, Vol. 3 of *Advanced Series on Ocean Engineering*, World Scientific.

Fredsøe, J., Andersen, K. H. and Mutlu-Sumer, B. (1999). Wave plus current over a ripple-covered bed, *Coastal Eng.* **38**: 177–221.

Görtler, H. (1941). Instabilität laminarer grenzschichten an konkaven wänden gegenüber gewissen dreidimenionalen störungen, *Z. Angew. Math. Mech.* **21**(4): 250–252.

Grant, W. D. and Madsen, O. S. (1979). Combined wave and current interaction with a rough bottom, *J. Geophysical Res.* **84**(C4): 17971808.

168

Grant, W. D. and Madsen, O. S. (1986). The continental shelf boundary layer, *Annu. Rev. Fluid Mech.* **18**: 265–305.

Hall, P. (1984). On the stability of unsteady boundary layer on cylinder oscillating transversely in a viscous fluid, *J. Fluid Mech.* **146**: 347–367.

Hansen, J. L., VanHecke, M., Haaning, A., Ellegaard, C., Andersen, K. H., Bohr, T. and Sams, T. (2001a). Instabilities in sand ripples, *Nature* **40**: 324.

Hansen, J. L., VanHecke, M., Haaning, A., Ellegaard, C., Andersen, K. H., Bohr, T. and Sams, T. (2001b). Stability balloon for two-dimensional vortex ripple patterns, *Physical Rev. Letters* **87**(20): 204301–4.

Hara, T. and Mei, C. C. (1990a). Oscillating flows over periodic ripples, *J. Fluid Mech.* **211**: 183–209.

Hara, T. and Mei, C. C. (1990b). Centrifugal instability of an oscillatory flow over periodic ripples, *J. Fluid Mech.* **217**: 1–32.

Honji, H. (1981). Streaked flow around an oscillating circular cylinder, *J. Fluid Mech.* **107**: 509–520.

Honji, H., Kaneko, A. and Matsunaga, N. (1980). Flows above oscillatory ripples, *Sedimentology* **27**: 225–229.

Isaacson, M. D. S. Q. (1976). Mass transport in the bottom boundary layer of cnoidal waves, *J. Fluid Mech.* **74**(3): 401–413.

Jonsson, I. G. (1966). Wave boundary layers and friction factors, *Proc.* 10th *Int. Conf. Coastal Eng.* pp. 127–148.

Kajiura, K. (1968). A model of the bottom boundary layer in water waves, *Bulletin Earthquake Res. Institute* **40**: 75–123.

Kamphuis, J. W. (1975). Friction factor under oscillatory waves, *J. of Waterway, Harbours, Coastal Engineering Division, ASCE* **101**: 135–144.

Kaneko, A. and Honji, H. (1979). Double structures of steady streaming in the oscillatory viscous flow over a wavy wall, *J. Fluid Mech.* **93**(4): 727–736.

Lee, S. K. and Cheung, K. F. (1999). Laminar and turbulent bottom boundary layer induced by nonlinear water waves, *J. Hydraulic Eng.* **125**(6): 631–644.

Leeder, M. (1999). *Sedimentology and Sedimentary Basins: From Turbulence to Tectonics*, Blackwell Science (UK).

LeMéhauté, B. (1968). Mass transport in cnoidal waves, *J. Geophysical Res.* **73**(18): 5973–5979.

Liu, A. and Davies, S. H. (1977). Viscous attenuation of mean drift in water waves, *J. Fluid Mech.* **81**(1): 63–84.

Longuet-Higgins, M. S. (1953). Mass transport in water waves, *Phil. Trans. Roy. Soc. Lond. A* **245**: 535–581.

Malarkey, J. and Davies, A. G. (2002). Discrete vortex modelling of oscillatory flow over ripples, *App. Ocean Res.* **24**(3): 127–145.

Marin, F. (1992). *Experimental study of the flow generated by water waves above a rippled bed*, PhD thesis, Université du Havre.

Marin, F. and Belorgey, M. (1993). Flow regime and eddy structures into a boundary layer generated by the swell above a rippled bed, *Sediment transport mechanisms in coastal environments and rivers, Euromech 310, World scientific*, pp. 231–245.

Marin, F. and Sleath, J. F. A. (1993). Mass transport over rippled beds, *Sediment transport mechanisms in coastal environments and rivers, Euromech 310, World scientific*, pp. 246–254.

Matsunaga, N., Kaneko, A. and Honji, H. (1981). A numerical study of steady streamings in oscillatory flow over a wavy wall, *J. Hydraulic Res.* **19**(1): 29–42.

Mouazé, D. (2001). *Etude expérimentale de la couche limite générée par la houle autour d'un cylindre*, PhD thesis, Université de Caen.

Mouazé, D., Ourmières, Y. and Chaplin, J. (2002). Steady and unsteady flow in wave-induced boundary layers, *Proc. 17th Int. Workshop on Water Waves and Floating Bodies, Cambridge, UK*, pp. 139–142.

Nielsen, P. (1981). Dynamics and geometry of wave generated ripples, *J. Geophysical Res.* **86**(C7): 6467–6472.

Nielsen, P. (1992). *Coastal bottom boundary layers and sediment transport*, Vol. 4 of *Advanced Series on Ocean Engineering*, World Scientific.

O'Donoghue, T. and Clubb, G. (2001). Sand rippples generated by regular oscillatory flow, *Coastal Eng.* **44**: 101–115.

Phillips, O. M. (1980). *The dynamics of the upper ocean*, 2nd edn, Cambridge University Press.

Ranasoma, K. I. M. and Sleath, J. F. A. (1994). Combined oscillatory and steady flow over ripples, *J. Waterway, Port, Coastal and Ocean Eng.* **120**(4): 331–346.

Ridler, E. L. and Sleath, J. F. A. (2000). Effect of bed roughness on time-mean drift induced by waves, *J. Waterway, Port, Coastal and Ocean Eng.* **126**(1): 23–29.

Riley, N. (1978). Circular oscillation of a cylinder in a viscous fluid, *Journal of App. Math. and Phys. (ZAMP)* **29**: 439–449.

Roache, P. (1972). *Computational Fluid Dynamics*, Hermosa.

Russell, R. C. H. and Osorio, J. D. C. (1957). An experimental investigation of drift profiles in a closed channel, *Proc. 6th Conf. on Coastal Eng.* **1**: 171–193.

Saric, W. S. (1994). Görtler vortices, *Annual Rev. Fluid Mech.* **26**: 379–409.

Sarpkaya, T. and Isaacson, M. (1981). *Mechanics of wave forces on offshore structures*, Van Nostrand Reinhold (NY).

Scandura, P., Vittori, G. and Blondeaux, P. (2000). Three-dimensional oscillatory flow over steep ripples, *J. Fluid Mech.* **412**: 355–378.

Schlichting, H. (1979). *Boundary layer theory*, 2nd edn, Mc Graw-Hill series in Mechanical Enggineering.

Sleath, J. (1976). On rolling-grain ripples, *J. Hydraulic Res.* **14**(1): 69–81.

Sleath, J. F. A. (1972). A second approximation to mass transport by water waves, *J. Marine Res.* **30**(3): 295–304.

Sleath, J. F. A. (1973). Mass transport in water waves of very small amplitude, *J. Hydraulic Res.* **11**(4): 369–383.

Sleath, J. F. A. (1984a). *Sea bed mechanics*, Ocean Engineering, a Wiley series.

Sleath, J. F. A. (1984b). Measurements of mass transport over a rough bed, *Proc. of the 19th Int. Conf. on Coastal Eng., Am. Soc. of Civil Engineers*, pp. 1149–1160.

Sleath, J. F. A. (1987). Turbulent oscillatory flow over rough beds, *J. Fluid Mech.* **182**: 369–409.

Sleath, J. F. A. and Ellis, A. C. (1978). Ripple geometry in oscillatory flow, *University of Cambridge, Dept. of Eng. Rep. A/Hydraul./TR2.*

Swan, C. and Sleath, J. F. A. (1990). A second approximation to the time-mean lagrangian drift beneath a series of progressive gravity waves, *Ocean Eng.* **17**(1/2): 65–79.

Tanaka, H., Mutlu-Sumer, B. and Lodahl, C. (1998). Theoretical and experimental investigation on laminar boundary layers under cnoidal wave motion, *Coastal Eng. J.* **40**(1): 81–98.

Taylor, G. (1923). Stability of a viscous liquid contained between two rotating cylinders, *Phil. Trans. Roy. Soc. Lond. A* **223**: 289–293.

Vittori, G. and Blondeaux, P. (1996). Mass transport under sea waves propagating over a rippled bed, *J. Fluid Mech.* **314**: 247–265.

Wiberg, P. L. and Harris, C. K. (1994). Ripple geometry in wave-dominated environments, *J. Geophysical Res.* **99**(C1): 775–789.

Yalin, M. S. (1971). *Theory of hydraulic models*, MacMillan Press, London.